DOI:10.15774/PPKE.ITK.2021.008

Pázmány Péter Catholic University

Faculty of Information Technology and Bionics

Roska Tamás Doctoral School of Sciences and Technology

Dénes Pálfi

Application of High Efficiency Enzymatic Compensated Two-Photon Photodissociation Material

Ph.D Dissertation

Thesis Advisor: Balázs J. Rózsa MD., Ph.D

Budapest, 2020

DOI:10.15774/PPKE.ITK.2021.008

Continuous effort - not strength or intelligence - is the key to unlocking our potential.

Winston Churchill

DOI:10.15774/PPKE.ITK.2021.008

TABLE OF CONTENT

DOI:10.15774/PPKE.ITK.2021.008

DOI:10.15774/PPKE.ITK.2021.008

ACKNOWLEDGEMENT

First of all, I would like to thank my supervisor, Dr. Balázs Rózsa. It was a truly moment when I met him first and later joined his really special laboratory. It was really interesting to see how research and develop field could bind together and open new horizons. Luckily, our laboratory is very multidisciplinary and during the past years I always could ask a little help for my work. I do hope I can return to them!

I would like to thank Pázmány Péter Catholic University for the great atmosphere and every little, but important bureaucratic and scientific help, because sometimes these little kind gestures could help the most!

I'm so thankful for the endless help for my colleague and my friend, Balázs Chiovini. I never forget the super long and exhausting experiments in the Pázmány lab. I do believe these experiments would never have been successful without his profession and his strength of will. I have learnt a lot from him.

I also would like to thank my colleagues, Gergely Katona, Gergely Szalay, Tamás Tompa, Linda Sulcz-Judák, Attila Kaszás, Gábor Juhász, Zoltán Szadai, Miklós Madarász and Myrtill Majoros. Moreover, I thank the unlimited help from the chemist team, especially from prof. Imre Csizmadia, Zoltán Mucsi, Csilla Haveland Lukácsné and Orsolya Frigyesi.

Finally, I have a special thanks to my family. They believed in me, when I needed it the most.

DOI:10.15774/PPKE.ITK.2021.008

LIST OF FIGURES

DOI:10.15774/PPKE.ITK.2021.008

DOI:10.15774/PPKE.ITK.2021.008

LIST OF TABLES

LIST OF SCHEMES

DOI:10.15774/PPKE.ITK.2021.008

ABBREVIATIONS

1P	–	*One-photon*
2P	–	*Two-photon*
2PLSM	–	*Two photon laser scanning microscopy*
ACSF	–	*Artificial cerebrospinal fluid*
AMPA	–	*α-amino-3-hydroxy-5-methyl-4-isoxazolepropionic acid receptor*
AP	–	*Action potential*
AP5	–	*(2R)-amino-5-phosphonovaleric acid*
bAP	–	*Backpropagation action potential*
CNQX	–	*6-cyano-7-nitroquinoxaline-2,3-dion*
DNI-Glu	–	*Dinitro indulin glutamate*
EOM	–	*Electro-optic modulator*
EPSP	–	*Excitatory post synaptic potential*
FS-PV INs	–	*Fast Spiking parvalbumin-expressing interneurons*
GABA	–	*Gamma-aminobutyric acid*
IC	–	*intercrossing change*
IPSC	–	*inhibitory post synaptic current*
LUT	–	*Look up table*
MNI-Glu	–	*Mononitro-indolinyl-glutamate*
$NADP^+$	–	*Nicotinamide adenine dinucleotide phosphate*
NMDA	–	*N-methyl-D-aspartate receptor*
ODS	–	*Octadecyl-silica*
OPA	–	*o-phthalaldehyde*
PDA	–	*Photodiode array*
PMT	–	*Photo multiplier tube*
QY	–	*Quantum yield*
SPW-R	–	*Sharp wave ripples*

DOI:10.15774/PPKE.ITK.2021.008

TFA	–	*Trifluoro acetate*
TPQE	–	*Two-photon quantum efficacy*
TPσ	–	*Two-photon absorption cross-section*
TTX	–	*Tetrodotoxin*
VGCC	–	*Voltage gated calcium channel*

DOI:10.15774/PPKE.ITK.2021.008

SUMMARY

Two-photon (2P) uncaging of caged-neurotransmitter molecules is a method of choice to mimic and study the subtleties of neuronal communication either in the intact brain or in slice preparations. However, the currently available caged materials (*i.e.* MNI-Glutamate) are just at the limit of their usability and have several drawbacks. The local and focal nature of their use may for example be jeopardized by a high spontaneous hydrolysis rate of the commercially available compounds with increased photochemical release rate. Here we synthesized more effective caged compounds (*e.g.* DNI-Glu•TFA), then we showed the mechanisms of hydrolysis and 2P activation, by using quantum chemical modeling. Furthermore, we developed a new enzymatic elimination method removing the liberated neurotransmitters inadvertently escaping from their original compound during experiment. This method is usable both in one-photon (1P) and in 2P experiments, and allows for the application of materials with an increased rate of photochemical release. The efficiency of this new cage-compound together with the developed enzymatic elimination method is demonstrated to be useful in neurophysiological experiments.

Sharp wave-ripple activity in the hippocampus is associated with the reactivation of neuronal ensembles within specific circuits during memory formation. Fast-spiking, parvalbumin-expressing interneurons (FS-PV INs) are thought to provide fast integration to these circuits by suppressing regenerative activity in their dendrites. Using 2P imaging and glutamate uncaging we challenged this classical view by demonstrating that the dendrites of FS-PV INs can generate propagating Ca^{2+} spikes during sharp wave-ripples. These spikes are originated from dendritic hot spots and mediated by L–type VGCC channels. Notably, Ca^{2+} spikes were associated with membrane potential oscillations, which we call ‘interneuronal rippleoscillations’. These interneuronal ripple oscillations had the same frequency as the field potential oscillations associated with sharp wave-ripples and controlled the phase of action potentials of FS-PV INs. Our results showed that the DNI-Glu•TFA can be used for uncaging modeling even for the most delicate structures such as tuft dendritic region in a long measurement time-scale.

In this present study I performed the DNI-Glu•TFA characterization, the experimental design, and the major part of the uncaging modeling.

DOI:10.15774/PPKE.ITK.2021.008

SCIENTIFIC QUESTIONS

In 21st century neuroscience, the greatest aim of the science community is to overcome the problem of data volume. The estimated number of neuronal connections are higher than we thought before, and they are not limited to neuronal ensembles or single cell level, but in dendritic level. The smallest unit for neuronal calculations is a dendritic segment. Therefore, if we ought to understand the mechanism better we have to try to image in sub micrometer range in a living tissue during ongoing brain activity. The modern imaging technique such as two-photon microscopy allows us not just to collect information from the brain with high spatial and temporal resolution but to control and to change the neuronal environment with the help of two-photon uncaging. This technique can mimic physiological release of neurotransmitters. One of the possible caged compound candidate, is the widely used MNI-Glu. However, it has certain disadvantages, like smaller two-photon quantum efficacy (TPQE) and other side effects. In the case of low TPQE, higher laser intensity would be necessary to reach threshold levels for dendritic integration processes, which is very undesirable due to the higher phototoxicity. The one-photon uncaging cannot be the solution too, because of its low spatial resolution and tissue penetration depth. Therefore, we started to design a novel uncaging compound, using quantum chemical modeling, to increase the TPQE which allows more efficient measurements on living tissue.
Along these perspectives, I addressed the following scientific questions:

Q1: Using theoretical modeling, is it possible to apply higher TPQE compound without any undesirable side effects?

Q2: Can it be used for extended, sensitive and complex biological experiments such as neuronal network modulation and dendritic integration during brain oscillations?

DOI:10.15774/PPKE.ITK.2021.008

I.VALIDATION OF DNI-GLU•TFA

1. BACKGROUND

In the latest decade neuroscience went through an enormous change with respect to the aspects of technology applied. The two-photon (2P) microscopy has revolutionized the whole neuroscience field of live imaging. In the past, confocal microscopy was applied for functional live imaging, but nowadays due to its obvious disadvantages, its application is mostly limited for anatomical studies. Nowadays, 2P imaging have replaced the confocal technique in functional, real time imaging field, and thanks to its high efficacy, the researchers could redefine their scientific questions. They could examine the phenomenon directly in living organisms, deep in the tissue and analyze the outcome in parallel with the electrophysiology for instance. Not only the electrophysiology but a series of techniques can be also combined with nonlinear microscopy (chemical and viral dying, focal and optogenetic stimulation, behavior tools for *in vivo* studies, etc.). Nonlinear, 2P microscopy became the leading tool in functional neuroscience.

These thoughts are also true for two photon uncaging. After the millennium some research groups have published different kinds of uncaging compounds, which were capable of two-photon absorption, but with quite low two-photon absorption cross section (TPσ) and efficacy. The common character of these compounds is the relative low cross-section and their low-moderate the hydrolytic stability. According to a general conclusion, the larger the cross-section the more decreased the hydrolytic stability of the compound. In the first section of the results, I show a novel series of compounds which were aimed to gap this efficacy/stability dichotomy, by means of a complex quantum chemical modeling. I validated the results of these calculations by detailed neurobiological characterization. I also developed a novel enzymatic method to provide an increased stability for the caged-molecule. In the second part of the result, I demonstrate an example about the usability of the new caged-compound via a neuroscientific question, namely how can we generate calcium spikes in neuronal dendritic segments. This novel two-photon uncaging tool can help to understand better the dendritic processes during ongoing brain activities.

DOI:10.15774/PPKE.ITK.2021.008

1.1. BASICS OF TWO-PHOTON MICROSCOPY

Two photon excitation phenomenon was described for the first time by Maria Goeppert-Mayer (1906–1972) in her doctoral thesis [1]. This quantum effect says one short-wavelength (~400 nm, high energy) photon can be replaced with two long-wavelength (~800 nm, low energy) photons during the excitation of a fluorescent molecule (**Figure 1**), based on the Heisenberg uncertainty principle.

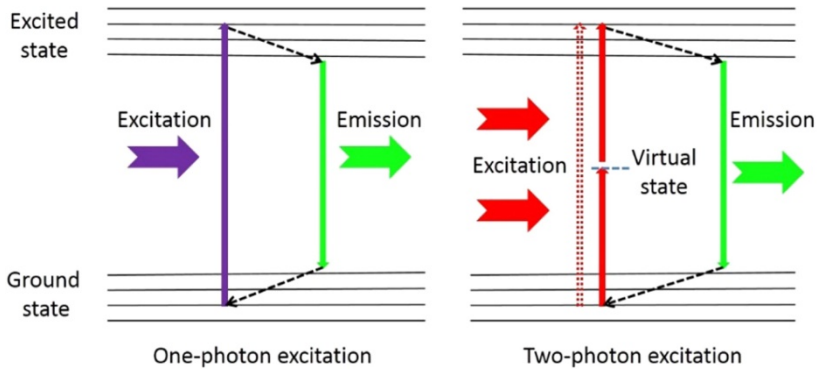

Figure 1 *Jablonski Energy Diagram* of one-photon vs two-photon excitation– the two simultaneous lower energy photons can combine (right) and result in the same effect as one higher energy photon (left) [2].

Despite the early discovery, the scientific community had to wait nearly 60 years for the first demonstration of 2P imaging in a neuroscience experiment (because of the lack of suitable laser source) which was published in Science by Denk and his colleagues in 1990 [3]. They reported the successful application of 2P excitation for an *in vitro* sample. The number of publications using 2P techniques has exponentially increased in the past few years [4]. In general, 2P microscopy is a form of laser-scanning microscopy that uses localized 'nonlinear' excitation to excite fluorescence only within a thin raster-scanned plane and nowhere else. Two-photon molecular excitation was made possible by the very high local instantaneous intensity provided by the tight focusing in a laser scanning microscopy combined with the temporal concentration of a femtosecond pulsed laser. Mode-locked laser produces a stream of colliding-pulses. The duration of a pulse is 100 fs at a repetition rate of 80 MHz (**Figure 2**) and the probability becomes appreciable for the molecule to absorb two longer wavelength photons (~800 nm) simultaneously. With this quantum method we are able to mimic the effect of a 1P excitation but within a tiny and limited excitation volume causing less phototoxicity and resulting in deeper penetration (up to 1 mm) in the tissue [5, 6].

DOI:10.15774/PPKE.ITK.2021.008

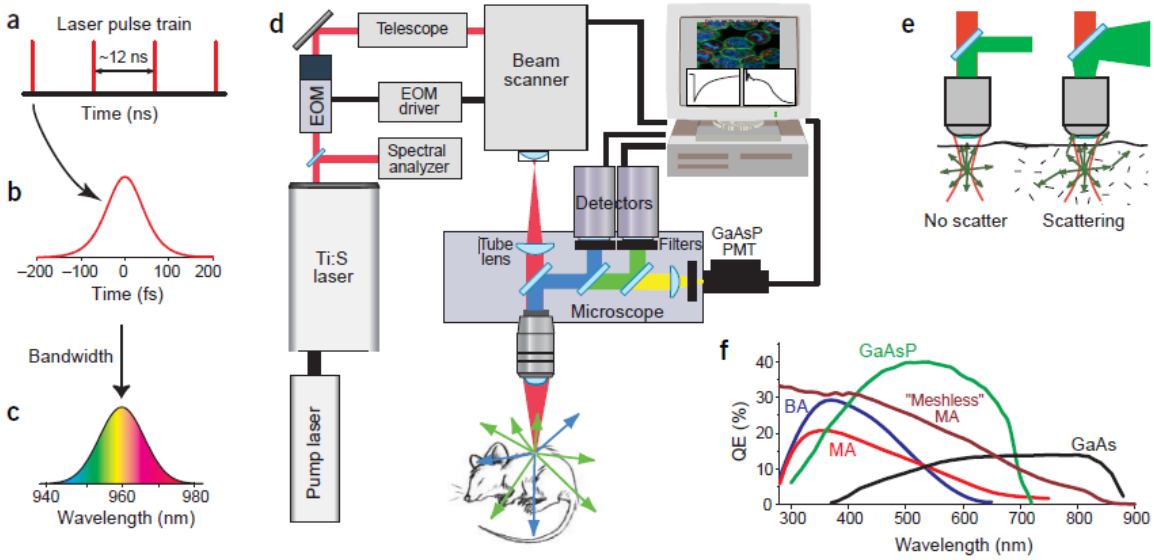

Figure 2 *Components of a multiphoton microscope* (a) Laser pulse train form the Ti:S mode locked laser. (b,c) The FWHM duration and spectral FWHM (~10nm) of a single laser pulse. (d) Schematic representation of a 2P system. (e) Emissioned photon scattering in deep tissue. (f) Comparison of different PMTs quantum efficacy.

1.2. PHOTODISSOCIATION IN NEUROSCIENCE

Two-photon photochemical uncaging has revolutionized numerous areas of cell- and neurobiology, because it allows rapid photochemical release of neurotransmitters in small volumes [7, 8]. This rapid and highly localized release of neuroactive molecules has produced relevant results in the studies of receptor distribution [9-11], channel kinetics [12, 13] or even network circuitry [14-18]. This is capable of mimics and therefore allows studying synaptic transmission mechanisms in the intact brain [11] from nitric oxide through protective groups [19] to various inhibitor substances [20] or excitatory neurotransmitters such as glutamate [18, 19]. The latter can be used to study synaptic integration [21, 22] and postsynaptic mechanisms [23, 24]. So far, the most commonly used caged glutamate compound is 2(*S*)-2-amino-5-(4-methoxy-7-nitro-2,3-dihydro-indol-1-yl)-5-oxo-pentanoic acid (MNI-Glu, **1**) [7, 25, 26], however, other neurotransmitters, like GABA [18, 25, 27] and Gly [28] are also reported. Ideal caging groups should be noncytotoxic, soluble, and should have biologically enduring bonds **(Figure 3**) with the neurotransmitters they protect.

DOI:10.15774/PPKE.ITK.2021.008

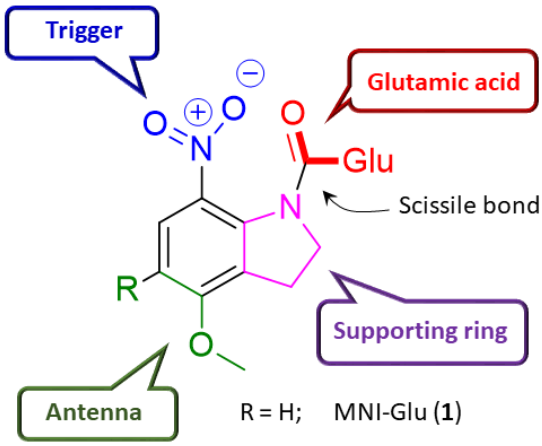

Figure 3 *Structural features of nitro-indolinyl cage scaffold, such as MNI-Glu (***1***, MonoNitro-Indolinyl-Glutamate).*

The cage scaffold effectively blocks the activity of the bonded biomolecule, when it undergoes efficient removal after excitation on the antenna moiety through the scissile bond. MNI-Glu fulfills the main requirements for an ideal cage compound including efficient uncaging processes with relatively high chemical yield, fast two-photon induced release (quantum yield 8.5%) [27], low spontaneous hydrolysis rate and low biochemical side effects [29]. Consequently, it is possible to effectively release glutamate from MNI-Glu by 2P laser scanning just on a few locations over neural elements.

The emergence of the importance of measuring temporally complex fast activation patterns, for example synchronized brain activity, such as sharp waves [30] or gamma oscillations [31] in fact raises new requirements which the above compound may not fit properly. Novel 3D scanning technologies provide the required spatially and temporally complex fast activation patterns [22, 32-35], but then the rate of photochemical release and the occurring phototoxicity induced by the required high laser intensity are becoming the limiting factors. In these cases, the fast-photochemical release requires a highly efficient two-photon absorption cross-section (2Pσ) and also a high quantum yield (QY) for the photochemical reaction of an ideal caged compound. The relationship between the chemical structure and QY or 2Pσ has not been investigated yet. It seems that the required high QY in the majority of the available compounds comes with a more unstable chemical structure making them more susceptible to spontaneous and undesired hydrolysis. Indeed, different rates of hydrolysis are shown for most of the caged compounds at physiological pH and temperature [36], which may result in dendritic swelling, intensive precipitation of the compound, robust changes in electrophysiological properties, or even cytotoxicity [36]. In some cases of caged materials, spontaneous hydrolysis is not so evident, at the same time, the continuous release and the resulting accumulation of the uncaged neurotransmitters may induce "side effects" on the receptors during the usually long physiological experiments.

DOI:10.15774/PPKE.ITK.2021.008

For example, when the ambient glutamate concentration reaches the micromolar range in the tissue, it activates half of the NMDA receptors (glutamate receptor, EC50 ~ 2 μM) [37-39], which causes AMPA receptor desensitization [40] and may also activate metabotropic glutamate receptors [41]. The most widely used caged glutamate, the MNI-Glu releases glutamate spontaneously at a rate, which may double the physiological ambient glutamate concentration (~25 nM) [37] during elongated measurements. This side effect could prevent the long and complex pharmacological experiments.

1.3. COMPARISON OF ONE AND TWO-PHOTON UNCAGING

Most of the caged compounds developed in the last decade are only sensitive to 1P laser irradiation. The two-photon cross-sections are typically too low to release the neurotransmitter effectively. The typical wavelength for one-photon excitation is around 355-380 nm and 420-440 nm [42], however these higher energy photons are scattering more significantly in the tissue and release the neurotransmitter not just in the focal point but along the whole optical pathway. The average two-photon uncaging volume is around 1 μm^3, which is a hundred times larger in the case of 1P uncaging. The phototoxicity and other side effects are also volume and concentration dependent. One of the other major differences between one- and two-photon excitation is the spatial resolution, which is a crucial factor to get a proper feedback about the dynamics of the signal propagation or the distribution of ion channels along the dendrite. During 2P uncaging the spatial resolution is ~2 μm in Z direction [43], in contrast with the 1P uncaging, where this factor is at least 12 μm (**Figure 4**).

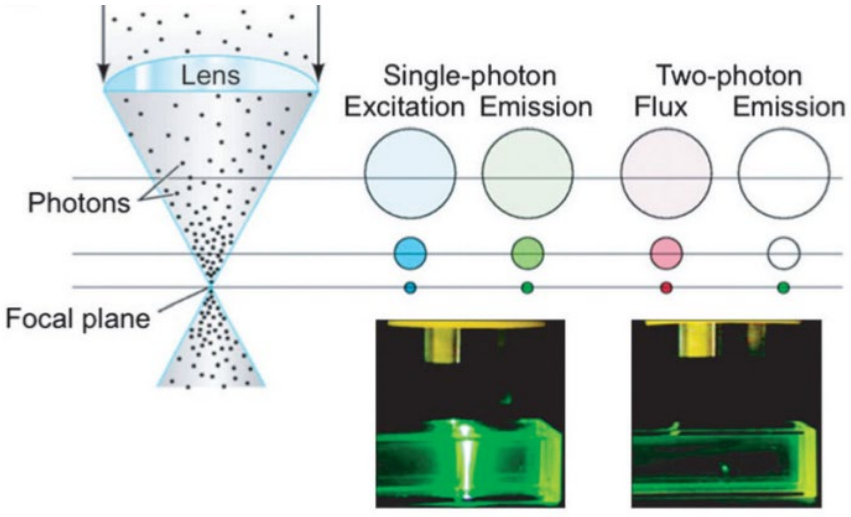

Figure 4 *Comparison of one- and two-photon uncaging*. Left, schematic diagram of a lens focusing light. *Middle*, One-photon excitation occurs throughout the light absorption path and total excitation is equal in each z-section. *Right*, 2P emission is confined to

DOI:10.15774/PPKE.ITK.2021.008

the focal plane due to the nonlinear nature of the creation of the excited singlet state [44].

2. MATERIALS AND METHODS

Amino acid derivatives were obtained from Bachem. All other chemicals were purchased from Sigma-Aldrich. Reagents were the highest purity available. ^{1}H, ^{13}C, NMR spectra were recorded in d^{6}-DMSO using TMS as an internal reference with a Bruker Avance III spectrometer operating at 400 MHz and 125 MHz. High-resolution MS spectra were measured using a Shimadzu MS spectrometer. In some cases, preparative HPLC was applied on a Armen type instruments, on a Gemini 250×50.00 mm; 10 μm, C18, 110A column in 0.2% TFA in water (eluent A) and acetonitrile (eluent B) liquid phase, using the gradient method.

2.1. SLICE PREPARATION AND ELECTROPHYSIOLOGY

Experiments were performed in accordance with the Hungarian Act of Animal Care and Experimentation (1998; XXVIII, section 243/1998.). The Animal Care and Experimentation Committee of the Institute of Experimental Medicine of the Hungarian Academy of Sciences, and the Animal Health and Food Control Station approved the experimental design. Acute hippocampal slices were prepared from P15-20 rats and mice using isoflurane anesthesia followed by swift decapitation. Horizontal (300 μm) brain slices were cut with a vibratome (Leica VT1000) and stored at room temperature in artificial cerebrospinal fluid (ACSF) (in mM: 126 NaCl, 2.5 KCl, 2 $CaCl_2$, 2 $MgCl_2$, 1.25 NaH_2PO_4, 26 $NaHCO_3$ and 10 glucose) as previously described.

Hippocampal neurons in CA1 stratum radiatum near the border of the stratum lacunosum-moleculare were visualized using 900 nm infrared oblique illumination. Whole-cell recordings were made at 32°C (MultiClamp 700B, Digidata 1440; Molecular Devices, Sunnyvale, CA, USA) with glass electrodes (current-clamp: 6–9 MΩ; voltage clamp: 3-5 MΩ) filled with (in mM): 125 K-gluconate, 20 KCl, 10 HEPES, 10 di-tris-salt phosphocreatine, 0.3 Na-GTP, 4 Mg-ATP, 10 NaCl, 0.1 Fluo-4, 0.1 ALEXA 594, and 0.008 biocytin. Cells with a resting membrane potential more negative than –50 mV were accepted. The recorded cells were classified as hippocampal interneurons and pyramidal cells according to their electrophysiological properties.

GABA IPSCs were induced by focal synaptic stimulation in the presence of AP5 (60 μM) and CNQX (10 μM). Glass electrodes (6-9 MΩ) filled with ACSF were placed at a distance of 10-15 μm from the soma (stimulation: 0.1 ms, 10-50 V, 10 ms pulse interval, 1 stimulus; BioStim, Supertech). All evoked IPSCs were verified for synaptic delay.

Data acquisition was performed using pClamp10 (Molecular Devices) and MES v5.3300 (Femtonics Ltd.) software.

2.2. MEASUREMENT OF FREE GLUTAMATE CONCENTRATION

DOI:10.15774/PPKE.ITK.2021.008

Spontaneous hydrolysis of DNI-Glu•TFA was detected by direct measurement of glutamate concentration. Standard solutions of the glutamic acid were prepared with distilled water at concentrations of ~ 1.9–2.5·10^{-3} M (weighed with analytical precision) and further diluted before use. Stock solution of *o*-phthalaldehyde (OPA) contained 0.20 g (weighed with analytical precision) in 10 ml methanol (referred to as methanolic OPA solution). DNI-Glu•TFA (~0.01–0.014 g) was weighed with analytical precision and dissolved in 10 – 50 ml distilled water or in 12 ml ACSF (final concentration 2.5 mM for DNI-Glu•TFA). Borate buffer was mixed in 50/50 (v/v) ratios from 0.4 M boric acid (dissolved in 0.4 M potassium chloride) – 0.4 M sodium hydroxide. OPA/MPA reagents were obtained by mixing, in the order of listing, 500 µl methanolic OPA with 4 ml buffer solution and 20 µl MPA. 12 µl NADP solution (0.2 M) was added to the ACSF solution of DNI-Glu•TFA with or without the glutamate dehydrogenase enzyme. Different amounts of enzyme were added (200, 520, 1040, 2000 and 5200 units/L) to the 12 mL ACSF solution saturated with 95 % O_2 and 5 % CO_2 gas. Derivatizations of blank, standard, and sample solutions were performed with reagent solutions stored in the refrigerator no longer than 9 days, at ~4 C°. 400 µl reagent solutions were mixed with 60 µl glutamic acid or DNI-Glu•TFA solutions and were let to decay for 5 min before injection. The analytical setup consisted of a Waters HPLC instrument (Waters, Milford, MA, USA), made of a Waters 996 PDA Detector and a Waters 474 Detector, a Waters 616 Controller quaternary pump with a thermostat table column area, and a Waters 717 Autosampler, operating with the Millennium Software (version 2010, 1992–95, validated by ISO 9002). The analytical columns were a BST Hypersil ODS, 15 cm × 4.0 mm, 5 µm; a Thermo Hypersil ODS 15 cm × 4.6 mm, 5 µm; and a Thermo Hypersil Gold 20 cm × 4.6 mm, 5 µm, all three used with guard columns (BST Hypersil ODS 20 mm × 4 mm, 5 µm or Thermo Hypersil ODS 10 mm × 4 mm, 5 µm).

Detections were performed simultaneously: PDA and Fl detectors were connected in the order of listing. PDA data were recorded between 190 and 400 nm (PDA) and evaluated at 285 nm for DNI and 337 nm for all the OPA–caged-glutamate derivatives. The fluorescence intensities of the OPA–glutamic acid derivative were evaluated at the optimum fluorescence wavelengths of isoindoles ($\lambda_{Ex}/\lambda_{Em}$=337/454 nm).

The eluent system consisted of two components: eluent A was: 0.05 M sodium acetate of pH 7.20 ± 0.05, while eluent B was prepared from 0.1 M sodium acetate–acetonitril–methanol (46/44/10), mixed in volume ratios and titrated with glacial acetic acid or 1.0 M sodium hydroxide to pH 7.20 ± 0.05. Elutions were performed in the gradient mode (40^0C): starting with 1% B for 1 min with 1.3 ml/min flow rate, reaching 100% B and 2.0 ml/min flow rate within 7 minutes, afterwards 3 minutes isocratic elution with 100% B, and, finally, returning to the initial concentration (1% B) in 1 minute and equilibrating for 4 minutes with this B content.

DOI:10.15774/PPKE.ITK.2021.008

OPA, MPA, glutamic acid, and glutamate dehydrogenase were obtained from Sigma (St. Louis, MO, USA). NADP was produced by Calbiochem (Germany, Darmstadt). HPLC-grade methanol and acetonitrile were purchased from Sigma-Aldrich (Seelze, Germany). Reagents were of the highest purity available.

2.3. TWO-PHOTON IMAGING

Two-photon imaging started 15–20 min after attaining the whole-cell configuration, on a two-photon laser-scanning system (Femto2D, Femtonics Ltd.) using femtosecond lasers (830-850 nm), (Mai Tai HP, SpectraPhysics). The Multiple Line Scanning Method was used to image long dendritic segments. At the end of each experiment, a series of images were taken across the depth of the volume encompassing the imaged neuron. Measurement control, real-time data acquisition and analysis were performed with a MATLAB-based program (MES, Femtonics Ltd.) and using a custom-written software.

2.4. TWO-PHOTON UNCAGING

After achieving whole-cell mode and filling pyramidal cells or interneurons with 100 μM Fluo-4, the bath solution was changed to ACSF containing 2.5 mM MNI-Glu•TFA (**1**), DNI-Glu•TFA (**2**), MNI-Ulg•TFA (**3**), or DNI-Ulg•TFA (**4**). Photolysis of caged glutamate was performed with 690-830 nm ultrafast, pulsed laser light (Mai Tai HP Deep See, SpectraPhysics or Cameleon Ultra II, Coherent). The intensity of the uncaging laser beam was controlled with an electro-optical modulator (EOM, Model 350-80 LA, Conoptics). Dispersion compensation was set to have maximal response at the depth of uncaging (50-80 μm from surface). The uncaging laser beam was coupled to the imaging optical pathway with a dichroic mirror (custom laser combiner, z750bcm; Chroma Technology Corp). Chromatic aberration was compensated for at the focal plane. Radial and axial alignment errors between the imaging and uncaging point spread functions were held with two motorized mirrors below 100 nm and 300 nm, respectively. Imaging was interleaved with two-photon glutamate uncaging periods when galvanometers jumped to 15-25 selected locations (within <60 μs jump time) and returned back to the imaging trajectory thereafter. Positions of uncaging sites were finely adjusted according to background images taken. Line scan data were also used to avoid overlap between uncaging locations and the dendrite. Photolysis of caged glutamates was performed in “clustered” patterns (0.8±0.1 μm distance between inputs) along the dendrite. Small drifts of the sample (approximately 0.1-0.2 μm/min) were compensated manually according to regularly taken background images and fluorescent pixel intensities in uncaging locations during photo-stimulation. The same uncaging pattern in the same dendritic location was used during comparison of different uncaging materials. Perfusion rate was set to 6 ml/min in order to increase the exchange rate of ACSF containing different uncaging materials. L-glutamic dehydrogenase (Sigma-Aldrich) was applied to the bath. β-

DOI:10.15774/PPKE.ITK.2021.008

nicotinamide adenine dinucleotide phosphate hydrate (200 µM, Sigma-Aldrich) was also applied to the bath, or alternatively, was injected with 1 µM/min with an initial concentration of 50-100 µM in order to compensate for consumption during the enzymatic reaction. Unless otherwise indicated, data are presented as mean±s.e.m. Statistical comparisons were performed using the Student's paired *t*-test.

2.5. STATISTICS

We measured the overall photochemical yields of DNI-Glu•TFA (**2**), DNI-Ulg•TFA (**4**), and MNI-Ulg•TFA (**3**) relative to the responses of MNI-Glu•TFA (**1**) by calculating the relative change in the second order of laser intensity (2P irradiation), which is required to generate overlap in the responses. We used unconstrained non-linear optimization to minimize the distance between the two point sets, where the changed variable was the scale factor applied to the 2P irradiation bringing the two point sets into overlap. The distance between the point sets was defined by the sum:

$$r = \sum_{i,j} \left(x_i - x_j\right) \cdot e^{-\left(y_i - y_j\right)^2 / S^2} \qquad \textbf{Eq. 1}$$

Where x_i and x_j are the laser intensity data corresponding to the two datasets, while y_i and y_j are the corresponding EPSP or Ca^{2+} transient amplitudes. S was set to 2 mV for EPSP, and 2 % for Ca^{2+} transient measurements (**Figure 11A**).

2.6. BASICS OF QUANTUM CHEMICAL MODELING

The fundamental equation of quantum mechanics was firstly described by *Erwin Schrödinger* in 1926. In principal, the applied computational methods in the quantum chemical modeling are solving the Schrödinger-equation for the examined molecule structure.

$$\hat{H}\Psi + \frac{h}{i2\pi}\frac{\delta\Psi}{\delta t} = 0$$

where $\hat{H}$ is the Hamilton operator, t is time and Ψ is the state vector of the quantum system. The Ψ state function is the function of the x, y, z coordinates and time (t) and during steady state the space- and time-dependent forms can be discussed independently [45].

Nowadays, instead of the sophisticated calculation of the classical wave functions (*ab initio*), the *density functional theory* (DFT) is the most popular tool for quantum chemical modeling, which based on the determination of the electron density [46,47]. Despite to the moderate computational demand, these tools can give quite accurate results even for larger molecules. However, these calculations are not strictly *ab-initio*, because they use a few embedded parameters, having experimental origins. These methods are based on the *Hohenberg-Kohn Theorems*, which says

DOI:10.15774/PPKE.ITK.2021.008

the external potential, and hence the total energy, is a unique functional of the electron density [48]. In this way, the ground state of electron density can be computed by the simple *Hartree-Fock* mathematical method, providing quick results. These methods seek to approximately solve the electronic Schrödinger equation. The total energy can be written as function of electron density:

$$E_{DFT}(\rho) = T(\rho) + J(\rho) + V_{ne}(\rho) + E_x(\rho) + E_c(\rho)$$

where $\boldsymbol{T(\rho)}$ is the kinetic potential, $\boldsymbol{J(\rho)}$: electron repulsion functional, $\boldsymbol{V_{ne}(\rho)}$ is external potential, $\boldsymbol{E_x(\rho)}$ is exchange functional, and $\boldsymbol{E_c(\rho)}$ is correlation functional.

In this equation, the unknown parts are only the exchange functional, and correlation functional, which are predefined parameters. To calculate them several mathematical methods are already exist. Most of the cases, the hybrid methods are most popular, where the exchange and correlation functionals are the linear combinations of DFT and HF exchange functionals. The B3LYP method is also a hybrid method [49], where the exchange part was replaced by a *Becke 3-parameter* functional, while the correlational part is using the *Lee–Yang–Parr* functional. The DFT methods use empirical parameters which are optimized by higher order calculations or experimental values, so these methods are not strictly *ab initio* methods. Despite of that during the last years the very popular DFT method numerous (more than 100) has been developed and it is rising.

The Born-Oppenheimer approximation says motion of every atomic nuclei and electrons in a molecule can be treated separately, since the atomic nuclei are much heavier than the electrons [49]. During geometrical optimalizations, the energy minimums of the hypersurface could be calculated with GDIIS and RFO methods, while for the calculation of transition states (TS) QST3 mathematical method is the most common tool. After the inspect, frequency calculation is very important to check whether it is a true minimum or transition state. IRC (*Intrinsic Reaction Coordinate*) method is also quite useful tool to confirm transition states. Most of the cases the reaction medium can be modelled with implicit or implicit-explicit (hybrid) solvent models [50,51]. The most popular implicit solvent model is the IEF-PCM (*Integral Equation Formalism Polarizable Continuum Model*) where the relative permittivity and the diameter of the solvent are the input parameters. Briefly this models the solvent as a polarizable continuum (dielectrics).

We used combinations of B3LYP theoretical method and 6-31G(d,p) basis sets for the quantum chemistry calculations. The numerical computations were carried out with the different versions of Gaussian program (G98, G03) [52,53] on the servers at University of Szeged.

DOI:10.15774/PPKE.ITK.2021.008

2.7. COMPUTATIONAL METHODS

All computations were carried out with the Gaussian09 program package [54] (G09), using convergence criteria of 3.0×10^{-4}, 4.5×10^{-4}, 1.2×10^{-3} and 1.8×10^{-3}, for the gradients of the root mean square (RMS) force, maximum force, RMS displacement, and maximum displacement vectors, respectively. Computations were carried out at B3LYP/6-31G(d,p) level of theory. The method and basis sets were chosen for their reliability in agreement with the studies established earlier. The vibrational frequencies were computed at the same levels of theory, as used for geometry optimization, in order to properly confirm that all structures reside at minima on their potential energy hypersurfaces (PESs). Thermodynamic functions U, H, G, and S were computed at 298.15 K.

Since trifluoroacetic acid (TFA) is mainly important for crystallizing the caged neurotransmitters under biologically relevant conditions (pH=7.4), the solvated caged neurotransmitters are mostly in their zwitterionic form. Therefore, geometric optimization of these ionic caged neurotransmitters was carried out in the absence of TFA in aqueous phase mimicked by the CPCM continuum model of implicit water as implemented in the Gaussian09 software package [54]. To obtain only the real local minima of the B3LYP/6-31G(d,p) potential energy surface, normal mode analysis was carried out at the same level of theory, then the B3LYP/6-31G(d,p) harmonic frequencies obtained were used to evaluate the thermochemical properties ($\Delta H°$, $\Delta S°$ and $\Delta G°$) of the species studied. The solvation Gibbs free energy of these species, $\Delta G_{solv}{}^{0}$, was also calculated.

Based on these B3LYP/6-31G(d,p) geometries, the degenerated two-photon absorption strength for an average molecular orientation was computed at the same B3LYP/6-31G(d,p) level of theory *via* quadratic response theory.

Geometric optimizations and frequency calculations were performed with the Gaussian09 software package, while the time-dependent calculations of static non-linear properties were obtained using the DALTON 2.0 quantum chemistry program[55]. The raw data were shown in Palfi et al. 2018 Supplementary material.

DOI:10.15774/PPKE.ITK.2021.008

2.8. DETAILED DESCRIPTION OF QUANTUM MOLECULAR COMPUTED RESULTS

Three branching points exist in the mechanistic scheme (**Figures 7, 14)**

Point I. The ratio of the processes from the ground state A(S_0) to the excited state B(S_1) and the spontaneous hydrolyzed J(S_0) compounds depends significantly on the experimental conditions, such as light intensity, temperature, and retention time of the compound in the experiment. In general, the typical ratio of the spontaneous hydrolysis for MNI-Glu is about 0.1%. Under the same experimental conditions, due to the 29-fold faster hydrolysis rate, about 3% of DNI-Glu•TFA hydrolyses spontaneously, and 97% is excited to the B(S_1) state.

Point II. The ratio of de-excitation processes from E(T_1) to H(S_0), and the triplet-state reaction of E(T_1) to F(T_1) was estimated by the relationship between the activation enthalpy [*H*(TS2)] of the process of E(T_1)→F(T_1) and the intercrossing enthalpy change [*H*(IC)] of the process E(T_1)→H(S_0). In this speculation, it is generally accepted that there is a linear relationship between the energy difference of the triplet and singlet surfaces and the intensity of intersystem crossing (ISC); the smaller the energy difference, the higher the transformation rate.

$$\Delta H(TS2) = H[TS2(\mathrm{T_1})] - H[E(T_1)], \qquad \textbf{Eq. 2}$$

$$\Delta H(IC) = H[E(T_1)] - H[H(S_0)], \qquad \textbf{Eq. 3}$$

The activation barrier of the straightforward triplet reaction for MNI-Glu is 8.3 kJ/mol higher than that of DNI-Glu•TFA, directing the transformation to the "unwanted" ISC process, mainly deactivating MNI-Glu by de-excitation. In the absence of general mathematical equations, it is difficult to estimate the ratio of the two processes. However, in the case of MNI-Glu, one can estimate that the transformation toward de-excitation should be about 10-fold faster than the "useful" triplet state reaction. For DNI-Glu•TFA, the same speculation shows an opposite picture, where the triplet state reaction is roughly 28 times faster, due to the lower *H*(TS2) enthalpy barrier (**Eq. 4**) as well as 2-times faster ISC. Overall, one can estimate, that the DNI-Glu•TFA transformation toward the position F(T_1) on the triplet surface is ten times more effective than MNI-Glu transformation, resulting in a 10-fold more effective process. A very different conclusion can be drawn for MNI-Ulg and DNI-Ulg, because the significantly higher barriers inhibit the formation of the photocleavaged products. Therefore, the ISC process dominates the mechanism. According to the QM calculations, only a very poor quantum yield can be assigned to the Ulg products.

DOI:10.15774/PPKE.ITK.2021.008

Point III. The ratio of the rate of back-isomerisation [H(S_0)→A(S_0)] and the spontaneous hydrolysis process [H(S_0)→J(S_0)] can be estimated by their activation enthalpy difference, described in **Eq. 4-7**. All these ratios were rounded to 0.1% toward the hydrolysis, therefore the overall main process is the back process to the initial state A(S_0). The same conclusion can be drawn for MNI-Ulg and DNI-Ulg (**Eq. 8-11)**.

$$\Delta H_{TS}(MNI\text{-}Glu) = H[TS6](MNI\text{-}Glu) - H[TS3](MNI\text{-}Glu) = 142.8 - 161.1 = \text{-}18.3\,\frac{kJ}{mol}, \quad \textbf{Eq. 4}$$

$$ratio(MNI\text{-}Glu) = e^{\frac{\Delta H_{\mathrm{TS}}(\mathrm{MNI\text{-}Glu})}{\mathrm{RT}}} = e^{\frac{-18.3\,\mathrm{kJ/mol}}{306\mathrm{K}\times 0.008314\,\mathrm{kJ/K*mol}}} = 0.000654 \approx 0.1\%, \quad \textbf{Eq. 5}$$

$$\Delta H_{TS}(DNI\text{-}Glu) = H[TS6](DNI\text{-}Glu) - H[TS3](DNI\text{-}Glu) = 138.9 - 158.6 = \text{-}19.7\,\frac{kJ}{mol}, \quad \textbf{Eq. 6}$$

$$ratio(DNI\text{-}Glu) = e^{\frac{\Delta H_{\mathrm{TS}}(\mathrm{DNI\text{-}Glu})}{\mathrm{RT}}} = e^{\frac{-19.7\,\mathrm{kJ/mol}}{306\mathrm{K}\times 0.008314\,\mathrm{kJ/K*mol}}} = 0.000371 \approx 0.1\%, \quad \textbf{Eq. 7}$$

$$\Delta H_{TS}(MNI\text{-}Ulg) = H[TS6](MNI\text{-}Ulg) - H[TS3](MNI\text{-}Ulg) = 167.3 - 185.5 = \text{-}18.2\,\frac{kJ}{mol}, \quad \textbf{Eq. 8}$$

$$ratio(MNI\text{-}Ulg) = e^{\frac{\Delta H_{\mathrm{TS}}(\mathrm{MNI\text{-}Ulg})}{\mathrm{RT}}} = e^{\frac{-18.2\,\mathrm{kJ/mol}}{306\mathrm{K}\times 0.008314\,\mathrm{kJ/K*mol}}} = 0.000658 \approx 0.1\%, \quad \textbf{Eq. 9}$$

$$\Delta H_{TS}(DNI\text{-}Ulg) = H[TS6](DNI\text{-}Ulg) - H[TS3](DNI\text{-}Ulg) = 157.9 - 178.2 = \text{-}20.3\,\frac{kJ}{mol}, \quad \textbf{Eq. 10}$$

$$ratio(DNI\text{-}Ulg) = e^{\frac{\Delta H_{\mathrm{TS}}(\mathrm{DNI\text{-}Ulg})}{\mathrm{RT}}} = e^{\frac{-20.3\,\mathrm{kJ/mol}}{306\mathrm{K}\times 0.008314\,\mathrm{kJ/K*mol}}} = 0.000152 \approx 0.1\%, \quad \textbf{Eq. 11}$$

DOI:10.15774/PPKE.ITK.2021.008

3. RESULTS

One of the main purposes of this work is to understand the relationship between the spontaneous hydrolysis, the two-photon photochemical cross-section, the 2P spectrum and the chemical structure. For this reason, we synthesized the known MNI-Glu (**1**) and its three novel chemical analogues and compared their chemical, biological characteristics to the prediction of the quantum chemical modeling. The experimental data, in good agreement with the theoretical results, showed that DNI-Glu (**2**) has indeed higher two-photon photochemical cross-section but its spontaneous hydrolysis is also higher compared to MNI-Glu (**1**). To overcome this drawback of DNI-Glu (**2**), we tried to eliminate or at least compensate for this high spontaneous hydrolysis compared to the level of MNI-Glu (**1**), so a new enzymatic, biocompatible method was also developed.

3.1. SYNTHESES OF MNI-GLU•TFA, MNI-ULG•TFA, DNI-GLU•TFA, AND DNI-ULG•TFA

The synthesis of MNI-Glu (**1**) was carried out according to a previously published method (**Scheme 1**).[27] Some modifications of the reaction conditions were made to optimize the original low yield. The synthesis of **2–4** were started on the same route (**Scheme 1**), starting from the methylation of the 4-hydroxy-indole, leading to **6**, then its reduction by $NaBH_3CN$. The 4-methoxy-indoline (**7**) was acylated by differently protected glutamic acids (Boc-Glu(OtBu)-OH - 8 and Boc-Glu-OtBu - **9**), resulting in the so called Glu- (**10**) and Ulg-derivatives (**11**), respectively. However, selection of mononitration and dinitration requires distinct procedures. The original, $AgNO_3$/AcCl reagent combination (Route A) was found to be the best choice for the selective mononitration at position 7 under dark condition. Here, the deprotection of **12** and **13** was carried out in a separate step by TFA, yielding MNI-Glu (**1**) and MNI-Ulg (**3**), respectively.

A selective and productive dinitration procedure, however, required more development (Route B–E), carried out only for the synthesis of DNI-Glu (**2**, **Scheme 1**). Further nitration of the protected mononitro compound **12**, by using $AgNO_3$/AcCl reagent, resulted in the desired product in low yield. This may be due to the moderate activity of the reagent (Route B). Stronger nitration condition, the $NaNO_3$ in TFA solvent, was elaborated on compound **1** (Route C), which resulted in significant amount of degraded side-product during the work-up. The same nitration condition was also tried on compound **10** (Route D), where the desired product was formed in one step, but in a moderate yield.

DOI:10.15774/PPKE.ITK.2021.008

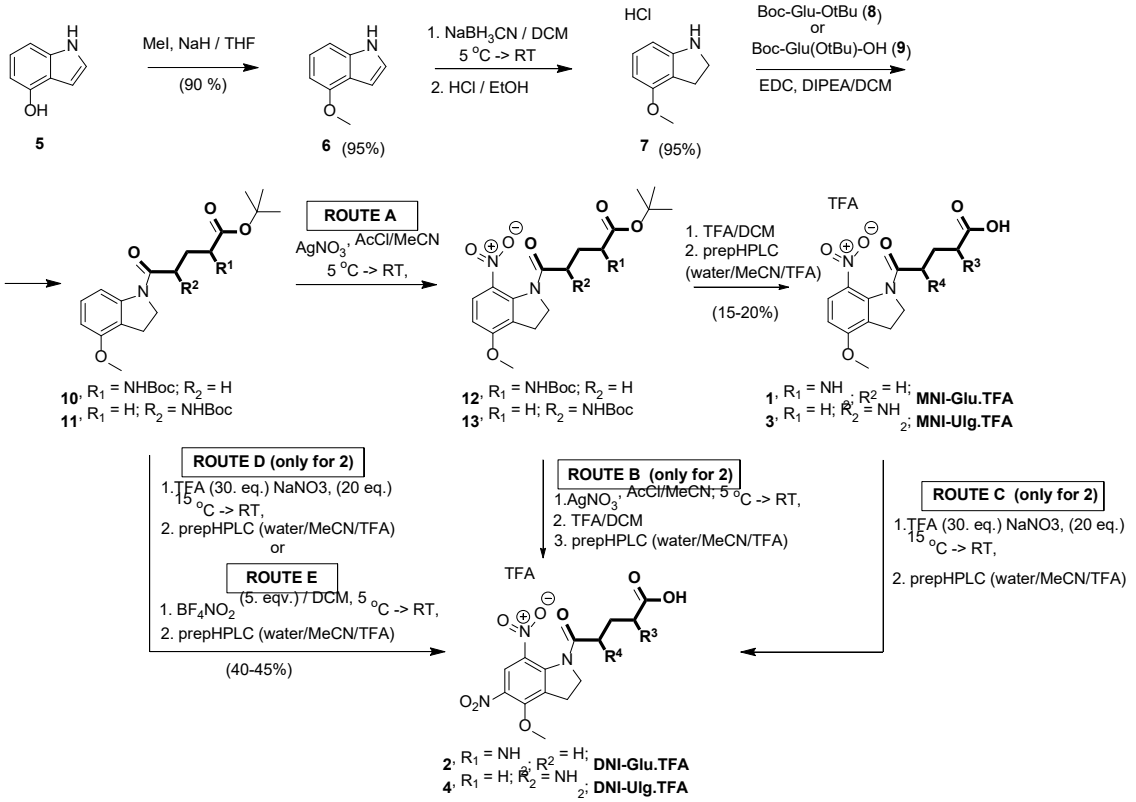

Scheme 1 The synthetic scheme of the trifluoroacetate salts of MNI-Glu (**1**), DNI-Glu (**2**), MNI-Ulg (**3**) and DNI-Ulg (**4**), including five **Routes A–E**.

Moreover, the large excess of TFA caused difficulties during work-up. Finally, the one-pot dinitration (Route E) of **10** later **11** by 3 equivalents of $NO_2 \cdot BF_4$ in dry DCM, at low temperature (0–5 ºC), was also carried out. Meanwhile the deprotection of **10** and **11** also happened. It should be pointed out, that the success of four different routes (B, C, D and E) were different. Out of the four methods, Route E turned out to be the most effective from synthetic point of view, exhibiting the highest yield (40–45%) and chemical purity (>99%) as well as appropriately low free glutamate content.

In all the cases, the last steps and the subsequent purification by preparative HPLC, as well as lyophilization were carried out in darkness to avoid unwanted photochemical degradation, which could lead to the appearance of free glutamate. The trifluoro acetate (TFA) counter ions were introduced in the purification step by means of the acidified aqueous eluent (0.2% TFA in water).

DOI:10.15774/PPKE.ITK.2021.008

3.2. ESTIMATION AND REDUCTION OF SPONTANEOUS HYDROLYSIS BY ENZYME

It is known, that MNI-Glu (**1**) tends to hydrolyze spontaneously under aqueous conditions, releasing the glutamate in an undesired process, causing difficulties in long-term measurements. It was reported earlier, that DNI-Glu (**2**) exhibits faster hydrolysis.[56] The ratio of the hydrolytic rates of DNI-Glu•TFA (**2**) vs. MNI-Glu•TFA (**1**) can be estimated from their carbonalycity values (CA%)[57] for their respective ground states, calculated as high as 42.3% and 38.1%, respectively (**Scheme 2.**). This 4.2% difference in carbonalycity (ΔCA% corresponds to about a 29-fold increase in the rate constant of spontaneous hydrolysis (see **Eq. 1-3**). In order to avoid the numerous negative effects of spontaneous hydrolysis, and therefore allow the use of caged compounds with high QY value (*e.g.* **2**), it was necessary to develop a selective method for the free glutamate elimination, which does not influence the concentration of the caged compound and has no side effects on the tissue. The use of enzymes, being selective for their substrates and effective in very low concentrations, seem to be an obvious choice. Two key processes are responsible for glutamate degradation: transamination and deamination. We chose glutamate dehydrogenase (**Scheme 2**), because its coenzyme, nicotinamide adenine dinucleotide phosphate ($NADP^+$) is not metabolized in the brain tissue[58]. To determine the required enzyme and coenzyme concentration, first we estimated the spontaneous hydrolysis rate of DNI-Glu•TFA (**2**), which was determined earlier. The detailed calculation is in the literature methods.[59] While the unit activity of glutamate dehydrogenase is defined for the reverse direction (for 2-oxoglutarate to glutamate conversion), consequently the rate of the forward reaction is estimated to be more than one order of magnitude slower. It is important to note that the rate of added glutamate elimination is approximately 6 orders of magnitude smaller than the rate of glutamate uptake in acute slices;[60] therefore, the enzymatic method does not interfere with the glutamate uptake system in small tissue volumes. At the same time, it effectively eliminates increased glutamate levels in the whole perfusion volume.

Two enzyme concentrations were tried, a lower 200–520 units l^{-1} and a higher 2000-5200 units l^{-1}. This enzymatic reaction effectively decreased glutamate concentration (pink and green in **Figure 5**) compared to the control experiment (blue in **Figure 5**). The higher enzyme concentration improved the efficiency of glutamate elimination (**Figure 5**). As expected, the enzymatic reaction was sufficiently selective, the enzyme did not decrease the concentration of the caged compound [without enzyme: 2.4 ± 0.019 mM, with enzyme: 2.39 ± 0.019 mM, p = 0.66, t-test; DNI-Glu•TFA (**2**) within 136 min.]. However, the efficiency of the method decreased with longer measurement times. Most of the laboratories, where uncaging experiments are performed, freeze and reuse solutions of caged materials, and therefore need efficient glutamate elimination in a longer time window. The effect of the enzyme was validated also in physiological measurements in the presence of DNI-Glu•TFA (**2**), since the amplitude of the uncaging-evoked responses did not change significantly during the experiments ($8.2\times10^{-4} \pm 4.1\times10^{-5}$ %/s, p = 0.84).

DOI:10.15774/PPKE.ITK.2021.008

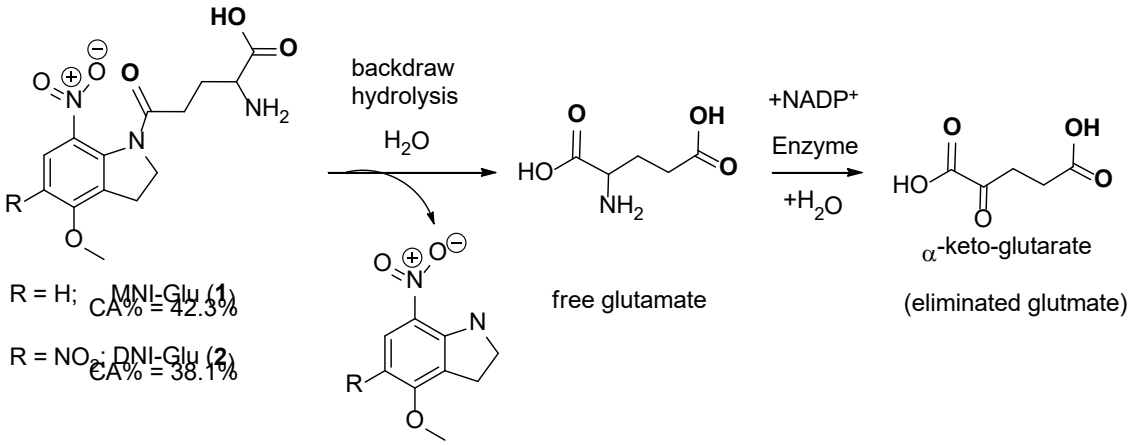

Scheme 2 *Enzymatic reduction.* The enzyme was glutamate dehydrogenase in the presence of $NADP^+$.

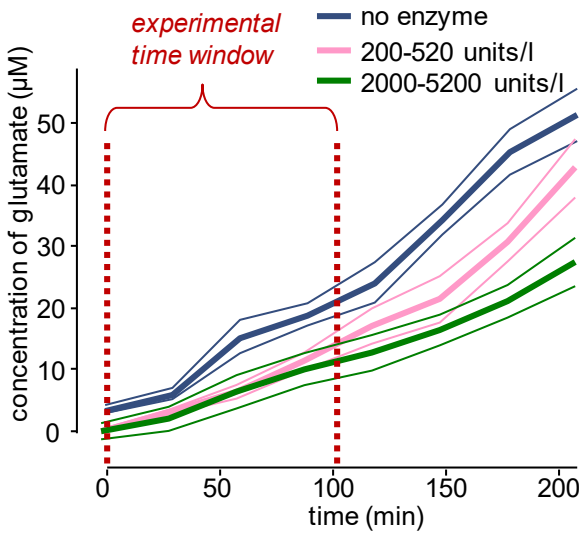

Figure 5 *Enzymatic compensation during long term measurements* Hydrolysis curves of DNI-Glu•TFA (**2**) in 2.5 mM measured under control condition (blue), and when 200-520 units l^{-1} (pink) or 2000-5200 units/l (green) enzyme and its coenzyme (200 μM $NADP^+$) were added. Thin lines show the error range. Measurements were performed in ACSF buffer at pH 7.4 at 309 K. The free glutamate was determined via OPA/MPA derivatization by HPLC, based on earlier experiences [61].

Next, we investigated whether electrophysiological measurements could be improved by the use of this novel enzymatic elimination method. It is known, that even a small increase in ambient glutamate level results in NMDA receptor activation and therefore it enhances neuronal excitability [62], increasing the rate of ongoing synaptic activity in whole-cell recorded neurons. Indeed, the frequency of spontaneous excitatory postsynaptic potentials (EPSPs) in CA1 pyramidal neurons increased, when DNI-Glu•TFA (**2**) was added to the bath perfusion (control: 1.64 ± 0.34 Hz; in the presence of DNI-Glu•TFA (**2**): 3.87 ± 0.67 Hz, n = 8, $p < 0.01$, *t*-test).

DOI:10.15774/PPKE.ITK.2021.008

Albeit the enzymatic method was not able to fully eliminate glutamate increase, as shown in **Figure 6**, it effectively decreased the unwanted EPSP frequency to the control value (1.71 ± 0.29 Hz; p > 0.3, n=8; **Figure 6**), indicating the physiological efficiency of the method. The increase in EPSP rate could not be the consequence of dendritic filtering or any alteration in our recording conditions, as the amplitude of EPSPs did not change throughout these experiments (control: 1.07 ± 0.16 mV; in DNI-Glu•TFA (**2**): 1.11 ± 0.28 mV, p = 0.9, *t*-test; when enzyme was added: 1.05 ± 0.21 mV, n = 3, p = 0.93, *t*-test). The use of the enzymatic elimination method allows a more precise comparison of the overall photochemical yield of MNI-Glu•TFA (**1**), DNI-Glu•TFA (**2**), since the modulatory effect of the elevated ambient glutamate concentration is eliminated.

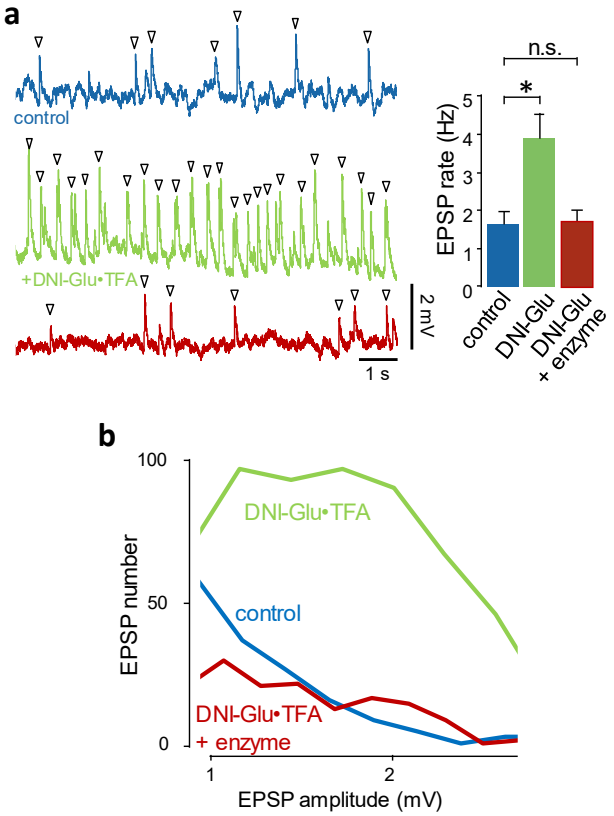

Figure 6 *Enzymatic method to compensate for the spontaneous hydrolysis of caged materials.* (**a**) Spontaneous somatic EPSPs recorded from a CA1 pyramidal cell under control conditions (blue), increased EPSPs in the presence of DNI-Glu•TFA (**2**, green), and normalized EPSPs, when the enzyme and its substrate ($NADP^+$) were also added to the perfusion solution containing **2** (red). (**b**) Frequency change of spontaneous EPSPs recorded in (n = 7) CA1 pyramidal neurons (mean±s.e.m.). EPSP frequency returned to its original value when the enzyme and its substrate was added (* and n.s. indicate p < 0.05 and non-significant difference, respectively). Corresponding amplitude histogram of spontaneous EPSPs.

DOI:10.15774/PPKE.ITK.2021.008

3.3. QUANTUM CHEMICAL MODELING OF THE PHOTOCHEMICAL UNCAGING PROCESS VERSUS GROUND STATE HYDROLYSIS MECHANISM

The reaction mechanism of the desired photochemical glutamate release and the unwanted hydrolysis of compound **1**–**4** were studied and compared on quantum chemical bases using GAUSSIAN 09 software [54] (**Figure 7**, **Table 1**). It is important to note that the mechanistic reaction profile proved to be identical for **1**–**4**, but the energy values varied in a significant range (4–10 kJ mol^{-1}) depending on the substituents. Starting from the initial state **A(S_0)**, the reaction mechanism could be divided into two main parts, the excited state cleavage (*Process 1*; **A→B→C→D→E→F →G**) and the undesirable ground state hydrolysis (*Process 2*; **A** → **H** then **H**+ H_2O → **I** as well as **A**+ H_2O → **I**).

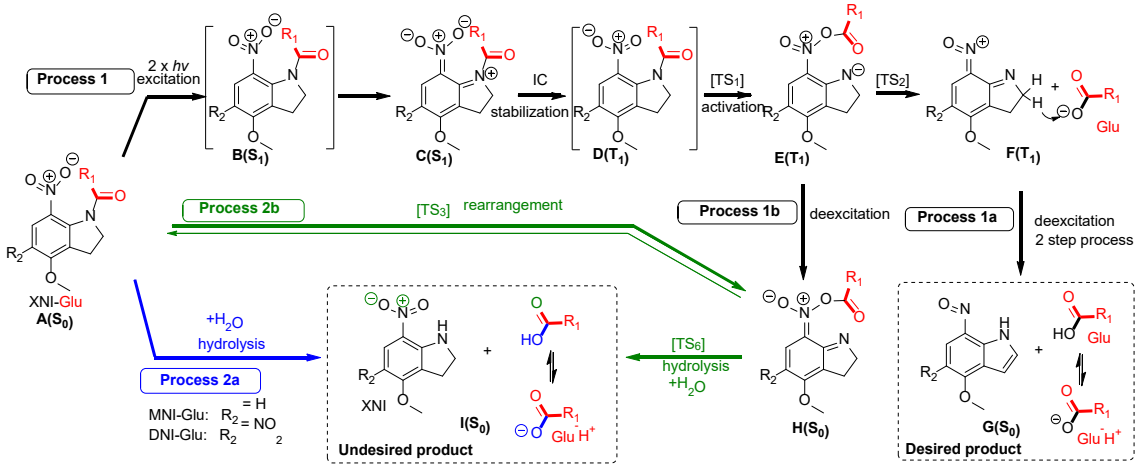

Figure 7 *Quantum chemical modeling of the photochemical reactions* (*process 1a* and *1b*, as black arrows), as well as the two possible mechanisms of ground state hydrolytic reactions (*process 2a* blue arrow; *process 2b* red arrow) for caged compounds **1**–**4**, at B3LYP/6-31G(d,p)//PCM(water) level of theory.

DOI:10.15774/PPKE.ITK.2021.008

Table 1. *Computed enthalpy values (in kJ mol^{-1}) of different states* (**A**–**I**) and **TS1**–**TS5** for compounds **1**–**4** relative to state **A** at B3LYP/6-31G(d,p)//PCM(water) level of theory.

	States[a]	(1)	(2)	(3)	(4)
Process 1	**A(S_0)**	0.0	0.0	0.0	0.0
	B(S_1)[b]	309.4	299.3	319.3	307.9
	C(S_1)	231.7	229.2	234.8	266.7
	D(T_1)	235.1	231.5	243.4	225.1
	TS1	282.4	270.5	338.1	310.1
	E(T_1)	167.0	183.5	138.8	143.0
	TS2	213.1	221.3	160.1	148.5
	F(T_1)	210.0	194.0	158.9	148.4
	G(S_0)	18.0	16.5	18.0	16.5
Process 2	**TS3**	142.8	138.9	167.7	177.7
	H(S_0)	128.2	125.3	93.7	95.7
	TS4	161.1	158.6	212.4	206.9
	TS5	196.0	186.8	> 200[c]	> 200[c]
	I(S_0)	–58.1	–67.3	–58.1	–67.3

[a]The states are shown in **Figure 7** and **9**. [b]Estimated from the excitation energies. [c]Estimated from the scanning of the reagent and reactant.

0

The main branch of *Process1* involves the excitation [**A(S_0)→B(S_1)**] followed by geometrical relaxation [**B(S_1)→C(S_1)**]. ~~H~~igh energy excited singlet state **C(S_1)** tends to transform to triplet state **D(T_1)** *via* intersystem crossing (ISC). In this triplet state an acyl transfer reaction can occur easily, where the acyl group migrates from the indoline N to the O of the NO_2, producing a very stable triplet state [**D(T_1)→E(T_1)**] via a low energy barrier: **TS1**. At this point, the mechanism may separate in to two ways (*Processes 1a* and *1b*). The desired product state, including the free glutamate [*Product 1;* **G(S_0)**], is reached by the way of the N–O bond cleavage of **E(T_1)** through **TS2**, leading to high energy state **F(T_1)** and finally a de-excitation to ground state [**G(S_0)**]. However, due to the relative stability of the triplet state **E(T_1)**, it can undergo a de-excitation process to a very reactive species **H(S_0)**.

Finally, from here on, it may go back to the starting state [**A(S_0)**] *via* **TS3** or to the undesired *Product 2* [**I(S_0)**] (**Figure 7**) *via* inadvertent hydrolysis, including **TS4**. As, in general, **TS3** exhibits lower enthalpy values, the **A(S_0)** can be the end of *Process 1a*, which may be considered as an unbeneficial "short circuit" of the process. *Process 2a* represents the direct, ground state hydrolysis of the reactant involving one water molecule [**A(S_0)→TS5→I(S_0)**], while *process 2b*,

DOI:10.15774/PPKE.ITK.2021.008

at first, involves an internal rearrangement [**A(S_0)→TS3→H(S_0)**] *via* the neighboring NO_2 group participation, before the aqueous hydrolysis leading to **I(S_0)**, through **TS4** occurs. According to the computed TS enthalpies, *process 2b* proved to be the energetically favorable, thus dominant process, due to the lower enthalpy values of **TS3** and **TS4**. The main difference between the MNI-Glu (**1**) and DNI-Glu (**2**) derivatives can be identified in the states of **E(T_1)→TS2→F(T_1)**. The relative enthalpies of **E(T_1)** for **2** are significantly higher than **1** by 183.5 – 167.0 = 16.5 kJ mol^{-1}, which means that the **E(T_1)** state of **2** cannot stabilize its structure, compared to **1**. As another effect, the de-excitation from the triplet state minimum [**E(T_1)**] to the ground state **H(S_0)** depends not only on the transition moment, but also on the lifetime of the **E(T_1)** minimum. Its lifetime depends on the height of the following transition state (**TS2**) **(Figure 8)**. If that transition state is higher than the population of the **E(T_1)** state is greater and the emission to the ground state would be more pronounced. This situation would reduce the efficiency of the glutamate release, which occurs in the minimum **F(T_1)** following **TS2**. This barrier height (**Table 1**) of **TS2** is 213.1 − 167.0 = 46.1 kJ mol^{-1} for **1** and 221.3 − 183.5 = 37.8 kJ mol^{-1} for **2**. This represents a 46.1 − 37.8 = 8.3 kJ mol^{-1} difference in the activation enthalpy for the N–O cleavage [**E(T_1)→F(T_1)**] than MNI-Glu (**1**, **Figure 9**). Due to the 8.3 kJ mol^{-1} difference in activation energies of dissociation (**TS2**), the relative rate constant exp (8.3/RT) amounts to approximately 20 times faster for **2**, as compared to **1**. Due to the increased rate of **2**, the population of the **E** state will be greater for **1**, therefore **1** has a longer lifetime at state **E(T1)**. Consequently, **1** has a greater chance to deexcite to **H(S0)**, and results in a significant increase in quantum yield (QY) for **2**.

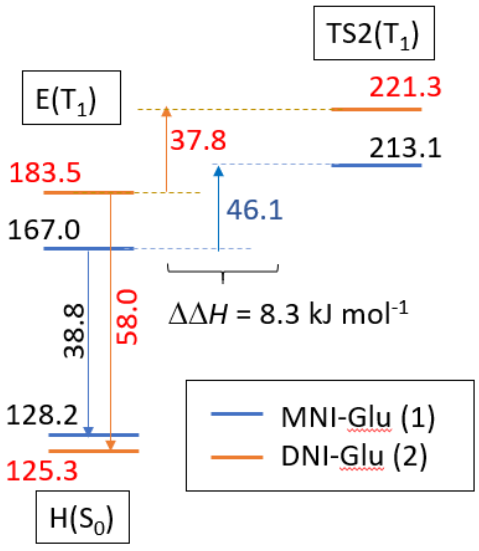

Figure 8. *Relative enthalpies of **H(S_0)**, **E(T_1)** and **TS2(T_1)** for MNI-Glu (1) and DNI-Glu (2)*, which estimates the quantum yield of the uncaging process.

The only drawback of DNI-Glu (**2**) versus MNI-Glu (**1**) indicated also by computations is the augmented ground state (non-photochemical) hydrolysis, which could expose aqueous tissues to

DOI:10.15774/PPKE.ITK.2021.008

an increased glutamate concentration. This ground state hydrolysis, however, is very hindered in the cases of DNI-Ulg (**4**) and MNI-Ulg (**3**), due to the strong H-bonding between the neighbouring C=O and α-NH_3^+ groups.

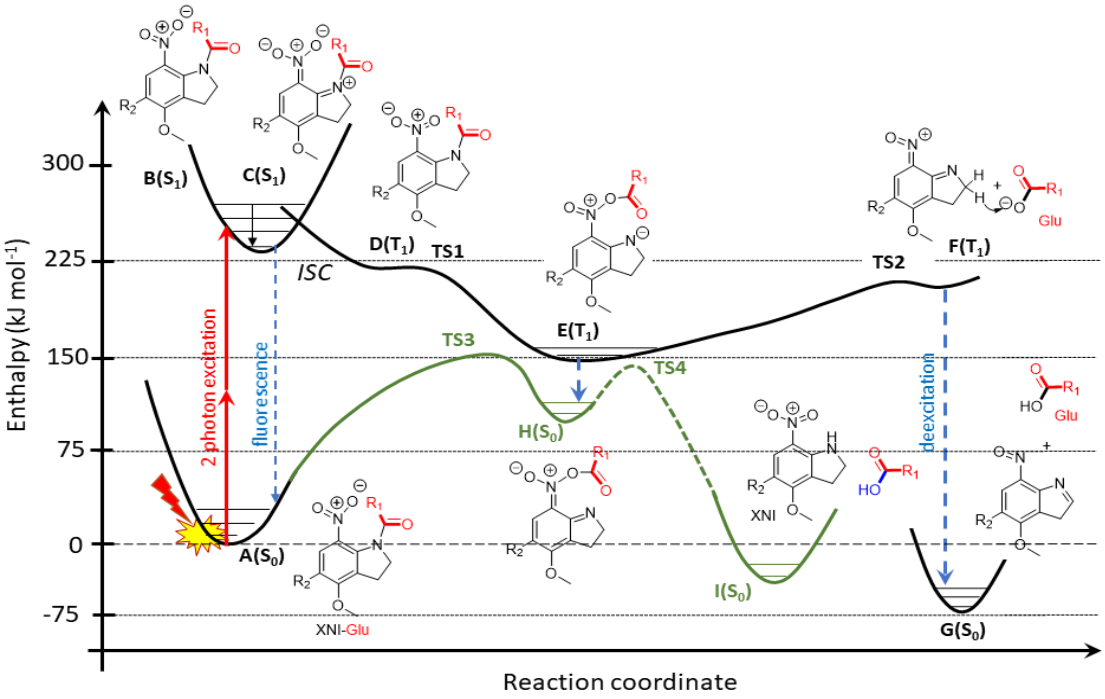

Figure 9. *Quantum chemical modeling of the potential enthalpy profile* of the photochemical (black) and ground state (green) mechanism for compounds **1**–**4** at B3LYP/6-31G(d,p)//PCM(water) level of theory. For detailed data see **Table 1**.

3.4. QUANTUM CHEMICAL MODELING OF THE TWO-PHOTON ABSORPTION (2PA)

The photochemical pathways of MNI-Ulg (**3**) and DNI-Ulg (**4**) are almost identical, but their energy values differ from their corresponding isomer pairs MNI-Glu (**1**) and DNI-Glu (**2**), respectively. Significant deviation can be observed in the **E(T1)** positions, which are much closer in enthalpy by an amount of 20–40 kJ mol^{-1} to the ground state structures **H(S_0)**, than those of **1** and **2**. This proximity of the triplet and singlet surfaces may suppose a very probable de-excitation from **E(T_1)** to **H(S_0)** in molecules **3** and **4** where the glutamate was bound in reverse mode as compared to **1** and **2**, decreasing the QY value significantly.

DOI:10.15774/PPKE.ITK.2021.008

Table 2. *The computed two-photon transition tensor components (S) for the S_0–S_1 transition of MNI-Glu (**1**) and DNI-Glu (**2**)* computed at B3LYP/6-31G(d,p) level of theory (*DFT method*) by using DALTON 2.0, assuming monochromatic light source with linear polarization.

Compounds	**MNI-Glu (1)**	**DNI-Glu (2)**
S_{xx}	13.5	28.6
S_{yy}	0.3	0.4
S_{zz}	0.1	0.1
S_{xy}	–0.4	–2.9
S_{xz}	–0.7	–0.4
S_{yz}	0.2	0.1

We computed the two-photon absorption (2PA) cross-section (σ) of the two, most potent uncaging compounds, MNI-Glu (**1**) and DNI-Glu (**2**), using DALTON 2.0 program in gas phase at B3LYP/6-31G(d,p) level of theory [55]. The 2P transition moment tensor components (S) were calculated and analyzed (**Table 2**). As it can be seen from these data, the S_{xx} is the highest tensor component for both compounds **1** and **2**, while the contribution of the other tensor components proved to be almost negligible. It appears that a charge transfer from OMe to NO_2 along the x direction (behaves as an antenna as illustrated in **Figure 3**) plays an important role in determining the net transition probability of these molecules. The 2PA cross section values (σ) were calculated from linear transition probability (D) and the excitation energy (E) (**Table 3**), based on a method published earlier [43,44,54,55]. The results show about 4.3 times larger σ value for DNI-Glu (**2**) than that of MNI-Glu (**1**). These results predict almost 5 times larger 2PA for the S_0–S_1 excitation, which influence positively the overall photochemical process.

DOI:10.15774/PPKE.ITK.2021.008

Table 3. *Two-photon transition energy (E in eV), probabilities (D_f, D_g and D in a.u.) and cross section values* (σ in a.u. as well as in GM) for the S_0–S_1 transition of MNI-Glu (**1**) and DNI-Glu (**2**) computed at B3LYP/6-31G(d,p) level of theory by using DALTON 2.0, assuming monochromatic light source (387 nm) with linear polarization.

Compounds	**MNI-Glu (1)**	**DNI-Glu (2)**	**Ratio**
E (eV)	3.20	3.12	–
D_f (a.u.)	65.0	282	**4.34**
D_g (a.u.)	61.4	278	**4.53**
D (a.u.)	376	1676	**4.46**
σ (a.u.)	6.94	29.4	**4.24**
σ (GM)	13.16	55.75	**4.24**

3.5. BIOLOGICAL COMPARISON OF FOUR GLUTAMATE CAGED COMPOUNDS

A. Neurobiological comparison experiment at constant laser intensity of caged compounds 1–4 (Method A)

For the comparison of the efficacy of the known MNI-Glu•TFA (**1**) as well as its modified compounds DNI-Glu•TFA (**2**), MNI-Ulg•TFA (**3**), and DNI-Ulg•TFA (**4**), were activated on the same temporally and spatially clustered patterns of inputs on hippocampal neurons. The uncaging effect was analyzed in terms of excitatory postsynaptic potential (uEPSP in mV) as well as the increased intracellular dendritic Ca^{2+} concentration measured by the change of fluorescent intensity ($\Delta F/F$) of the added Ca-ion sensitive dye (Fluo-4, **Figure 10A**). These compared their somatic membrane potential and dendritic Ca^{2+} responses evoked in the presence of **2**–**4** to the ones evoked in the presence of **1**, since the properties of the later compound is being well-documented in the literature[11, 54]. The pairwise comparison was performed on the same neuron and same dendritic location.

The same laser intensity, concentration and uncaging time were used during each experiment. All caged materials were bath-applied at a concentration of 2.5 mM. The same laser intensity, which induced only small excitatory postsynaptic potentials (uEPSPs) and small dendritic Ca^{2+} responses (1.43 ± 0.15 mV and 1.22 ± 0.11 $\Delta F/F$, respectively) in the presence of MNI-Glu•TFA (**1**) elicited approximately 10-fold higher responses in the presence of DNI-Glu•TFA (**2**; 15.22 ± 0.28 mV and 7.95 ± 0.25 $\Delta F/F$, respectively, 1st row of **Figure 10B**). The same experiments for DNI-Ulg•TFA (**3**; 2.85 ± 0.29 mV and 1.82 ± 0.12 $\Delta F/F$; 2nd row of **Figure 10B**) brought

DOI:10.15774/PPKE.ITK.2021.008

significantly less effective results. Interestingly, MNI-Ulg•TFA (**4**; 0.91 ± 0.18 mV and 0.29 ± 0.10 ΔF/F, 3rd row of **Figure 10B**) proved to be less effective than the reference compound **1**.

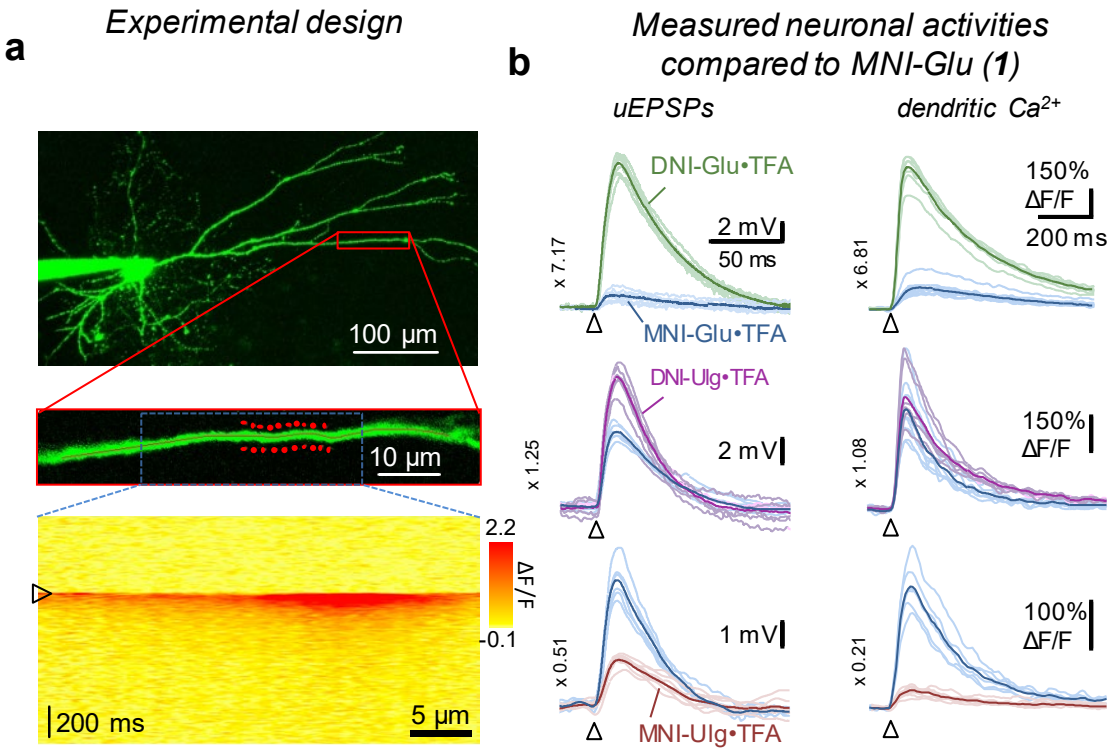

Figure 10. *Comparison of novel caged glutamate compounds **2**–**4** with the reference MNI-Glu•TFA (**1**) in neurophysiological uncaging measurements at constant laser energy (**Method A**).* (**A**) (Top) Maximal intensity z projection image of a CA1 interneuron filled with Fluo-4 and Alexa 594. (Middle) Red box shows the enlarged dendritic region of interest. Red points are locations selected for two-photon glutamate uncaging in the presence of DNI-Glu•TFA (**2**, 2.5 mM). (Bottom) Representative uncaging-evoked Ca^{2+} response (average of 5 traces) measured along the red curve in middle. Triangle shows time of uncaging. (**B**) (Left) Two-photon uncaging-evoked somatic excitatory postsynaptic potentials (uEPSPs) in the presence of cage compounds (**1**–**4**). (Right) Simultaneously measured Ca^{2+} transients DNI-Glu•TFA (**2**, green), DNI-Ulg•TFA (**3**, violet), MNI-Ulg•TFA (**4**, red) compared to the responses measured in the presence of MNI-Glu•TFA, (**1**, blue). Bold lines show averages. Triangles indicate uncaging time.

DOI:10.15774/PPKE.ITK.2021.008

B. Neurobiological comparison experiment at increasing laser intensity of caged compounds 1–4 (Method B)

The dendritic and somatic membrane compartments can nonlinearly amplify high-amplitude EPSPs, therefore the overall photochemical yield cannot be determined precisely at a single laser intensity. Thus, we performed a series of uncaging measurements precisely on the same site of the same neuron only for MNI-Glu (**1**) and the most effective DNI-Glu (**2**) (in the sequence of +**1** → wash-in → +**2** → wash-in → +**1**) at increasing laser intensities, as shown in **Figure 11**. The responses were plotted as a function of the second order of the laser intensity and measured the increased photochemical yield as a relative *x*-axis shift of the responses in the presence of DNI-Glu•TFA (**2**) and MNI-Glu•TFA (**1**) by calculating the distance (black arrows) between the two point sets using unconstrained nonlinear optimization (**Figure 11A**). The average distance between the two point sets revealed that the release of glutamate with the same rate from MNI-Glu•TFA (**1**) requires 7.17 ± 0.84-fold (ΔF/F) higher two-photon excitation as compared to DNI-Glu•TFA (**2**; $p < 0.00001$, n= 10).

Next (**Figure 11B**), we repeated these experiments by comparing the efficiency of the photochemical release of the reversely coupled compounds, MNI-Ulg•TFA (**3**) and DNI-Ulg•TFA (**4**) relative to the release of MNI-Glu•TFA (**1**). This agreed well with the uncaging experiment, obtained at constant laser energy. The uncaging responses were increased to 5.47 ± 0.49 ($p=0.001$, n=8) for DNI-Glu•TFA (**2**), and 1.25 ± 0.04 ($p = 0.003$, n = 3) for DNI-Ulg•TFA (**4**) and reduced to 0.51 ± 0.07 ($p < 0.001$, n = 4) in the presence of MNI-Ulg•TFA (**3**) as compared to the reference MNI-Glu•TFA (**1**)(**Figure 11B**, *inset*). Our data showed that the efficiency of photochemical release and the uncaging measurements correlated well for all of the four uncaging materials (R = 0.9877).

DOI:10.15774/PPKE.ITK.2021.008

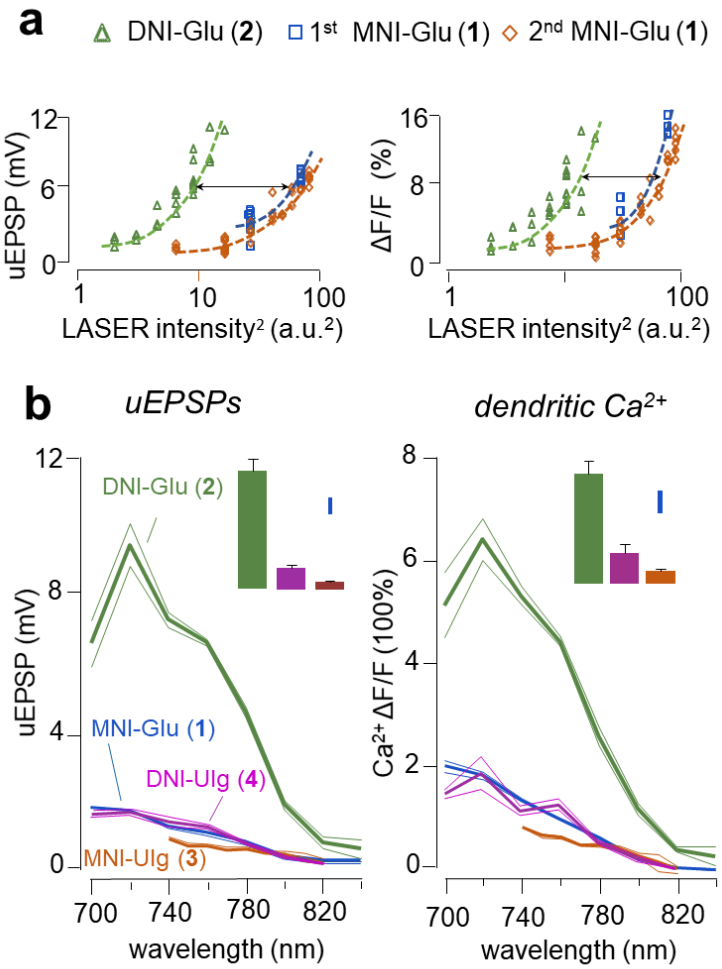

Figure 11. *Comparison of novel caged glutamate compounds in neurophysiological uncaging measurements with varied laser energies (**Method B**).* (**A**) Excitatory postsynaptic potential (uEPSP) amplitudes and dendritic Ca^{2+} transient plotted as a function of the second order of the uncaging laser intensity in the presence of MNI-Glu•TFA (**1**, blue squares), following wash-in of DNI-Glu•TFA (**2**, green triangle), and after recovery in MNI-Glu•TFA (**1**, orange diamond). (**B**) Amplitude of uEPSPs (*left*) and dendritic Ca^{2+} transients (*right*) evoked in the presence of MNI-Glu•TFA (**1**, blue, n=11 neurons;), DNI-Glu•TFA (**2**, green, n=8), DNI-Ulg•TFA (**3**, violet, n=3), MNI-Ulg•TFA (**4**, red, n = 6) as a function of wavelength (mean ± s.e.m). (*Inset*) The normalized amplitudes of uEPSPs and dendritic Ca^{2+} transients with their errors were measured at 740 nm and normalized to responses of MNI-Glu•TFA (**1**) (blue bars show one unit). In summary, the efficacy of the four compounds studied by different biological methodology (**1**–**4**) are compared in **Table 4**.

DOI:10.15774/PPKE.ITK.2021.008

Table 4. *Comparison of the relative efficacy values of MNI-Glu•TFA (**1**), DNI-Glu•TFA (**2**), DNI-Ulg•TFA (**3**) and MNI-Ulg•TFA (**4**)*, measured in *in vitro* neurobiological investigations. For details see **Figure 7** and **8**.

Compounds	**Method A** Rel. to (**1**)	**Method B** Rel to (**1**)
MNI-Glu•TFA (**1**)	1.00	1.00
DNI-Glu•TFA (**2**)	5.47 ± 0.49	7.17 ± 0.84
MNI-Ulg•TFA (**3**)	0.51 ± 0.04	not examined
DNI-Ulg•TFA (**4**)	1.25 ± 0.03	not examined

3.6. DETAILED EXAMINATION OF THE SIDE-EFFECT OF CAGED COMPOUNDS MNI-GLU•TFA (1) AND DNI-GLU•TFA (2) ON GABA-A RECEPTORS

A further important criterion of a good caged glutamate candidate is the reduced effect on GABA receptors. It was shown earlier that the experimental concentration of MNI-Glu (**1**), like other caged compounds, cause antagonist effect on the GABAergic transmission [64-66]. Generally, this results in a significant issue when neuronal circuits are studied due to the appearance of imbalanced epileptiform events [64]. In addition to that, MNI-Glu typically blocks the GABAergic responses, which prevent the study of inhibitory network activity. Consequently, we measured the effect of DNI-Glu•TFA (**2**) on inhibitory postsynaptic currents (IPSCs) elicited by focal electric stimulation while blocking glutamatergic synaptic transmission (10 µM CNQX and 60 µM AP5) (**Figure 12**). Whereas MNI-Glu•TFA (**1**) in 350 µM reduced the amplitude of IPSCs by 54.3 ± 4.0 % ($p = 0.03$, $n = 5$), DNI-Glu•TFA (**2**), at the same concentration, did not induce any significant reduction (6.1 ± 5.0 %, $p = 0.28$, $n = 11$). These data undoubtedly show that the application of DNI-Glu may avoid these side effects observed during the application of MNI-Glu.

DOI:10.15774/PPKE.ITK.2021.008

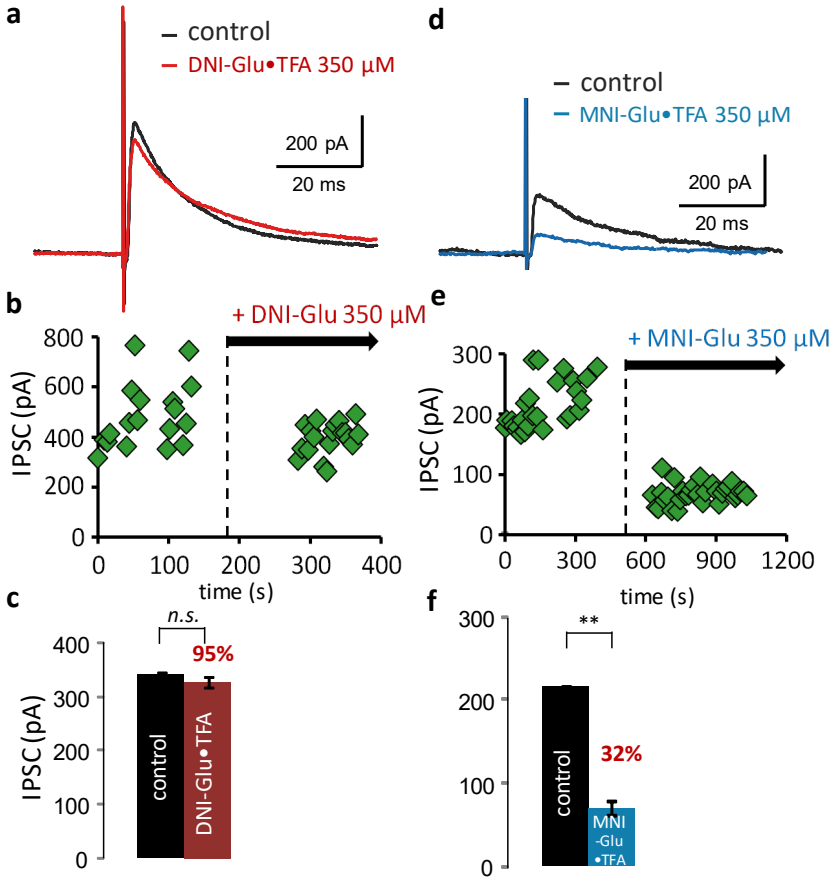

Figure 12. *Effect of DNI-Glu•TFA (2) and MNI-Glu•TFA (1) on IPSCs elicited by synaptic stimulation.* (**A**) Representative IPSCs under control conditions and in the presence of 350 µM DNI-Glu•TFA. Synaptic responses were induced by focal electric stimulation during the blockade of glutamatergic synaptic transmission (10 µM CNQX and 40 µM AP5) in order to isolate GABAergic currents. (**B**) Amplitude of IPSCs plotted against time. Gray arrow indicates time when DNI-Glu•TFA was added to the bath. (**C**) Average IPSC amplitudes under control conditions (black) and in the presence of DNI-Glu•TFA. Bars show mean ± s.e.m., n = 5, p = 0.27. (**D-F**) The same as **A-C** but for MNI-Glu•TFA. Note the stronger GABA effect of MNI-Glu•TFA. Note, the higher reduction in IPSC amplitude in the presence of MNI-Glu•TFA. Asterisks indicate significance ($p < 0.01$).

DOI:10.15774/PPKE.ITK.2021.008

3.7. INHIBITION EFFECT OF DNI-GLU•TFA (2) ON POTASSIUM CHANNELS

Potassium channels play a crucial role in dendritic integration and signaling, so it was important to exclude the potential effect of DNI-Glu•TFA (**2**) during the experiments. I examined the role of DNI-Glu•TFA (**2**) in K^+ currents in CA1 pyramidal cells. I performed somatic patch-clamp recordings in the presence of mibefradil (50 µM), nimodipine (20 µM), ω-Conotoxin MVIIC (0.5 µM), TTX (3 µM) to isolate potassium currents in CA1 pyramidal neurons (**Figure 13A**). In voltage clamp (VC) mode currents were elicited by somatic voltage injection [58]. After the control part DNI-Glu•TFA (**2**) (2.5 mM) was added to the bath to record the amplitude changes of potassium currents (**Figure 13B, C**). Ten minutes after DNI-Glu•TFA (**2**) was added to the bath the potassium current recordings were started. There is no significant change in K^+ current profile (DNI-Glu•TFA 0.99+0.02, p=0.94, n=4 cells). I concluded that K^+ currents in CA1 pyramidal neurons were found not to be sensitive to DNI-Glu•TFA (**2**).

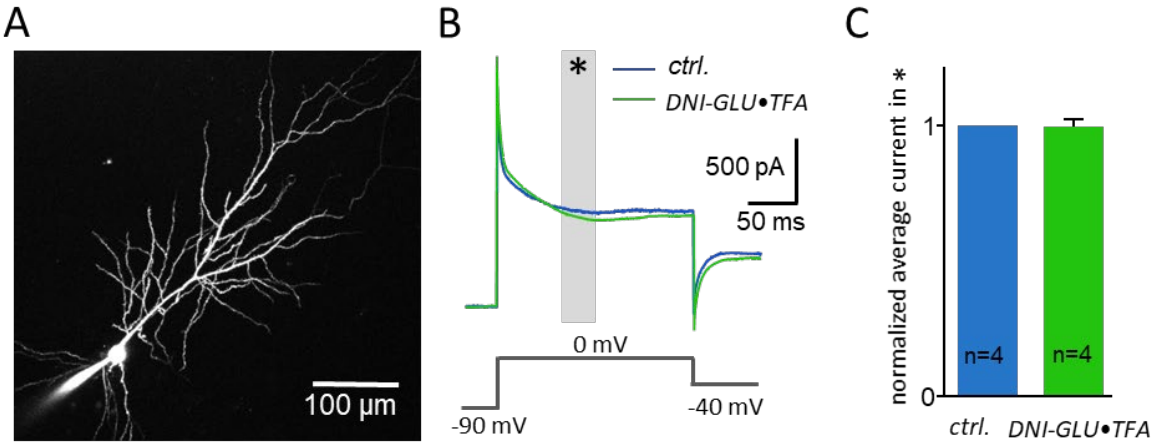

Figure 13. *Pharmacological profile of uncaging evoked K^+ currents* (**A**) Maximal intensity z projection image of an CA1 pyramidal cell filled with the morphological dye, Alexa 594. (**B**, *Top*) Example electrophysiological current traces in control conditions (mibefradil 50 µM, nimodipine 20 µM, ω-Conotoxin MVIIC 0.5 µM, TTX 3 µM, blue) and in presence of DNI-Glu•TFA (2.5 mM, green). Gray bar shows the ROI where the analysis was made. (*Bottom*) Electrophysiological protocol for the experiment. (**C**) Amplitude of electrophysiological responses in control conditions (blue) and in presence of DNI-Glu•TFA (green). The responses were normalized for the comparison (n=4 cells).

DOI:10.15774/PPKE.ITK.2021.008

4. CONCLUSION OF THE QUANTUM CHEMICAL AND BIOLOGICAL RESULTS

According to computational results, we can transform our enthalpy values to kinetical information and explain the differences between MNI-Glu (**1**) and DNI-Glu (**2**) observed during the neurobiological uncaging experiments (**Figure 14**). The difference between **1** and **2** can be traced back to three branching points (labeled by the Arabic numerals I, II, and III). Initially at point I, a small percentage of the compounds (0.1% for MNI-Glu and 3% for DNI-Glu, respectively) hydrolyses spontaneously. The remnants (99% and 97%, respectively) undergo excitation. At point II about nine times as much DNI-Glu (**2**) (90%) undergoes dissociation compared to MNI-Glu (**1**) (9.9%). This data, 11% agrees well with the experimentally determined QY (8.5%) [22]. In the final stage, at point III, only 0.1% of the compound is hydrolysed. Consequently, DNI-Glu (**2**) is the most effective of the four compounds, in excellent agreement with experiments.

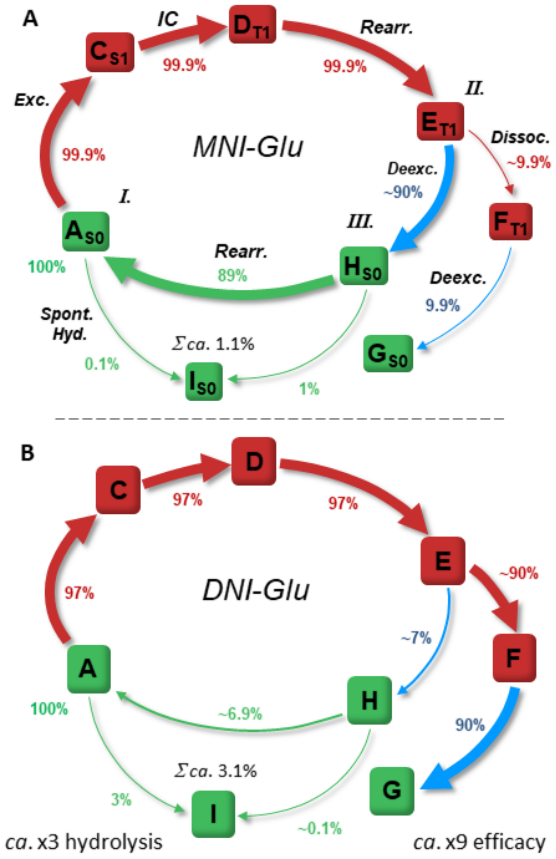

Figure 14 *Symbolic representation of the mechanism underlying photochemical release and spontaneous hydrolysis of MNI-Glu (1), DNI-Glu (2).* (a-b) The thickness of these lines correspond to the efficiency of the individual steps. Numerical estimates of efficiency (in %) of each step are indicated. Branching points are marked by *I*, *II*, and *III*. Red, green, and blue arrows indicate excitation, rearrangement and de-excitation parts of the schemes respectively.

DOI:10.15774/PPKE.ITK.2021.008

5. DISCUSSION PART I

The following questions arose during the research process. How can different segments of dendrites be activated or inhibited? How can the activity patterns of neurons be modified? Previously, scientist used invasive focal or local electric stimulations of the axons in order to modify indirectly cellular or populational activities [68-70]. However, this technique carries serious drawbacks, namely that we never know exactly the precise location of the activation site. Moreover because of the mixed axonal bundles we need to exclude the noninterested chemical or physiological components by applied pharmacons [71]. For instance, when we want to excite glutamatergic axons we have to block GABA-axons by different antagonists [70, 71]. Nowadays, photoactivation is one of the most important techniques to model dendritic processes. We can apply inactive caged neurotransmitters into the brain tissue and activate them in a well determined spatial-temporal pattern. Uncaging allows us to release neurotransmitters precisely next to the synaptic active site, thus we can activate ligand dependent receptors along the region of interest [8, 11]. Moreover, with uncaging we can activate predefined synaptic patterns in subdentritic level [22].

With the appearance of two-photon techniques, new horizons were opened for photoactivation too. Two-photon uncaging has numerous advantages compared to one-photon uncaging [72]. The excitation volume in 2P uncaging is limited only to the focal point and does not excite the entire lightpath in the tissue, which greatly reduces ~~the~~ phototoxicity. Moreover, with 2P neurotransmitter release can be achieved in deeper layers through the increased penetration depth, therefore 2P technique gives an opportunity to use uncaging *in vitro*, *ex vivo* or even *in vivo* [73]. So far only one caged material, MNI-Glu was used in relevant neurobiological studies. At this point, it is important to bear in mind that MNI-Glu is excitable by 2P [25, 27]. However, MNI-Glu has significant and well-documented disadvantages such as high ambient glutamate level during elongated measurements, low two-photon efficacy and higher phototoxicity. Several groups have reported that there is a clear connection between photostimulation efficacy and molecule stability [36]. Increasing efficacy decreases the stability of the caged material and causes spontaneous hydrolysis. It was reported earlier, that DNI-Glu exhibits faster and higher hydrolysis [56] than MNI-Glu. Indeed, the degree of hydrolysis depends on physiological pH and temperature [36], causes dendritic swelling, intensive precipitation of the compound, robust changes in electrophysiological parameters, or even toxicity [36]. In order to overcome these important drawbacks we introduced an enzymatic compensation method. Increased level of endogen dehydrogenase concentration can stabilize the abnormal concentrations of hydrolyzed neurotransmitters, thus, DNI-Glu can be used for long term experiments because of the low ambient glutamate level. Here, I demonstrated that even a robust hydrolysis can be eliminated with enzymatic compensation.

DOI:10.15774/PPKE.ITK.2021.008

Different cage molecules, such as the synthetic molecule, may exhibit other important disadvantages, namely the conformation of cage molecules may be similar to other endogen receptor ligands, thus open the possibilities to bind them causing serious side effects. It is known from the literature that the higher concentrations of MNI-Glu block the inhibitory synaptic transmissions [64] and modify the potassium channel activity. DNI-Glu, as a same aromatic molecule, theoretically could cause the same effect. Though my results show that the DNI-Glu has no significant negative side effect neither on GABA transmission nor on the potassium channel activity, DNI-Glu is a physiologically more intact molecule than the widely used MNI-Glu.

In summary, we have shown that DNI-Glu•TFA (**2**), in combination with a novel enzymatic hydrolysis correction method is a faster and more effective caged compound than MNI-Glu•TFA (**1**). The *ca*. 7 times higher efficacy of DNI-Glu (**2**) allows the decrease of the effective concentration significantly. Our data showed that the efficiency of photochemical release calculated from the quantum chemical model and from the uncaging measurements correlated well for all of the four uncaging materials tested. The enzymatic glutamate elimination shown here is a major addition to the uncaging toolbox available for scientists. It allows the use of new caged compounds with fast photochemical reactions and high spontaneous hydrolysis rates by eliminating the undesired side-effects of glutamate molecules escaping from caged compounds. These favorable results give the possibility to study higher states of dendritic processes, which is impossible with previously published caged materials.

DOI:10.15774/PPKE.ITK.2021.008

II. UNCAGING MODELING OF DENDRITIC REGENARATIVE EVENTS ON FS-PV$^+$ INS IN THE HIPPOCAMPUS

In this following part, I present our recent findings about FS-PV INs regenerative events.

1. BACKGROUND

Fast-spiking, parvalbumin-expressing CA1 interneurons (FS-PV INs) are considered to be one of the key elements of fast feed-forward and feedback inhibition [74, 75]. They are recruited during different population activities such as sharp wave-ripple (SPW-R), gamma & theta oscillations [74, 76-79], and their involvement in different cognitive dysfunctions such as schizophrenia has been suggested [80, 81]. According to the generally accepted view, FS-PV INs act as fast integrators, with passive dendritic membrane properties and a fast membrane time constant [82-84]. As a further support to this concept, the dendrites of FS-PV INs are rich in fast, Ca^{2+}-permeable AMPA receptors and have a high K^+ to Na^+ conductance ratio, which further suppresses electric activity in their dendrites [82, 85-89]. These features result in accelerated kinetics of excitatory postsynaptic potentials (EPSPs), a reduced, sub-millisecond temporal window for dendritic integration, and precise and fast coupling between EPSPs and action potential (AP) outputs [76, 82, 84, 86, 90]. The fast integrator role of FS-PV INs is also thought to be reflected in spatiotemporally confined Ca^{2+} dynamics in their a spiny dendrites. Namely, Ca^{2+} signaling is kinetically fast, as it is mediated by Ca^{2+}-permeable AMPARs with the assistance of intensive Na^+-Ca^{2+} exchange and increased Ca^{2+} buffering; hence, Ca^{2+} accumulation is localized to small, ~1 μm long dendritic microdomains [76, 87, 89]. Backpropagation of APs (bAP) is decremental, with little activity dependence in the passive, K^+ channel-dampened dendrites of FS-PV INs. Moreover, it was shown that dendritic spikes could not be evoked in these cells [82, 86]. This widely accepted view of passive, dampened dendrites in FS-PV INs was based on experiments performed in conventional submerged recording chambers where the spontaneous network activity is low. However, under more physiological conditions, when neurons are bombarded with precisely timed and spatially clustered dendritic inputs [22, 91], the rules of dendritic integration and EPSP-AP coupling can be different [22, 92]. The coordinated synaptic activity during *in vivo* or *in vitro* SPW-R oscillations is more than an order of magnitude greater [93, 94] than the synaptic activity observed in regular *in vitro* recording conditions. Thus, SPW-R may provide a sufficiently large number of coincident inputs to generate a dynamic switch from a ground state of passive integration to an active state. Under conditions where spontaneous synaptic activity is low, bAP-induced Ca^{2+} transients can only be detected in FS-PV IN dendrites up to 150 μm from the soma [76, 82, 86]. In contrast, bAPs invade even the farthest dendritic

DOI:10.15774/PPKE.ITK.2021.008

segments when spontaneous network activity is high enough, such as during *in vitro* SPW-Rs [92]. In good agreement with these data, somatic current steps and simultaneous Ia-type K^+ channel blockade revealed an extended pool of functional voltage-gated Ca^{2+} channels (VGCCs) in FS-PV IN distal dendrites [86, 92] which could be recruited under active network conditions.

In order to test the hypothesized network activity-related dynamic switch in FS-PV IN functions, local field potential (LFP) and whole cell patch-clamp recordings were performed simultaneously in a dual-superfusion recording chamber [22, 92, 95] and these recordings were combined with three dimensional fast acousto-optical 3D trajectory scanning [96] (**Figure 15**). This *in vitro* approach allowed access to long, thin, tortuous apical dendritic segments (up to 700 µm in length, **Figure 15**) [96] that are otherwise hardly accessible for *in vivo* recordings or dendritic patch-clamping [97]. Horizontal hippocampal slices were cut from transgenic mice which expressed enhanced green fluorescent protein under the parvalbumin promoter [92, 98]. Since both surfaces of the 450 µm-thick acute slices were perfused in a dual-superfusion chamber, oxygenation improved and the number of ongoing EPSPs, and consequently their integration, was closer to *in vivo* conditions [22, 92, 95].

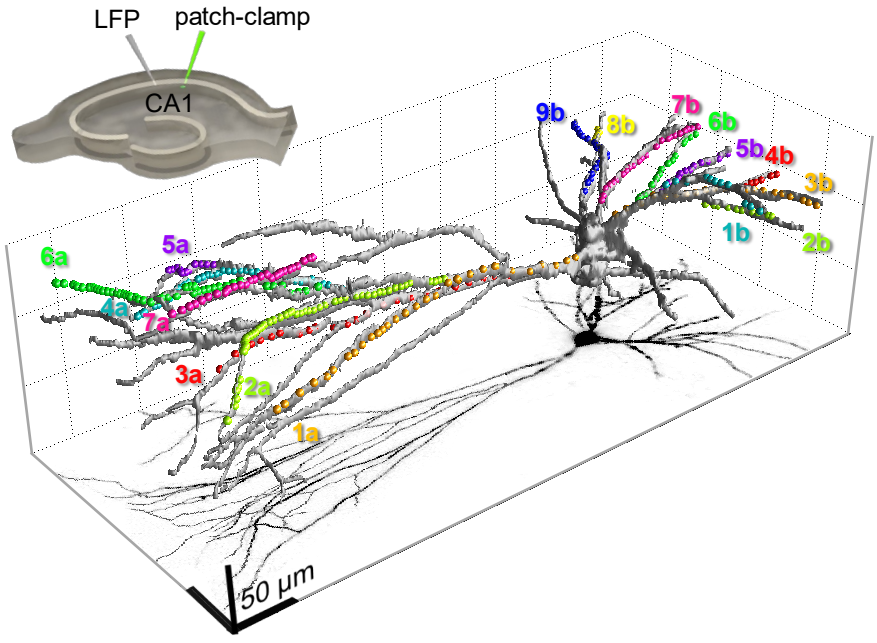

Figure 15 *Neuron anatomy and experimental setup.* Full dendritic arborization of a FS-PV IN (top) imaged by 3D acousto-optical scanning in the hippocampal CA1 region. Colored spheres represent locations for the point-by-point trajectory scanning. Inset, experimental setup.

Under these recording conditions, SPWs occurred spontaneously at a rate of 1.44±0.09 Hz (n=32) and were associated with network ripple oscillations (f_{max} 249.2±12.7 Hz; $f_{Fourier}$ 181.6±7.1 Hz;

DOI:10.15774/PPKE.ITK.2021.008

Figure 16) [92, 95]. Importantly, the observed SPW-R events had similar laminar profiles, oscillation frequencies and hippocampal propagation properties to those observed *in vivo* [92, 94, 95, 99].

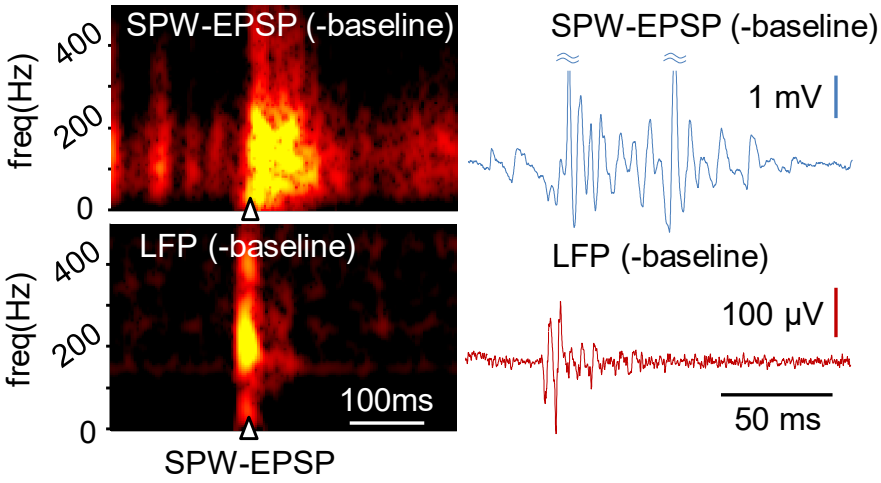

Figure 16 *Characterization of the electrophysiological recordings.* (Left) Spectrograms (average of 7 traces) of SPW-EPSPs and LFPs. Representative individual traces after baseline subtraction (right) are shown on the same timescale.

Enhanced green fluorescent protein-expressing FS-PV INs in CA1 stratum pyramidale were identified with two-photon imaging and were filled with fluorescent Ca^{2+} indicator (OGB-1 and Fluo-4) via a somatic recording pipette [22, 92, 96]. All of the recorded neurons were characterized as typical fast-spiking interneurons according to previous classifications [82, 83, 100, 101]. These physiological parameters were analyzed with cluster analysis, which further supported the homogeneity of the sampled interneuron population. For Ca^{2+} imaging, the objective was moved to the center of the region of interest and a reference z-stack was taken with 3D acousto-optical imaging in order to select multiple long dendritic segments for 3D trajectory scanning [96]. Then simultaneous fast 3D recordings along multiple recording sites were performed, which covered the majority of the dendritic arbor during SPW-R events (**Figure 15**). Responses were spatially normalized and plotted in 2D as a function of distance along the imaged dendritic segment(s) and time (**Figure 17**).

DOI:10.15774/PPKE.ITK.2021.008

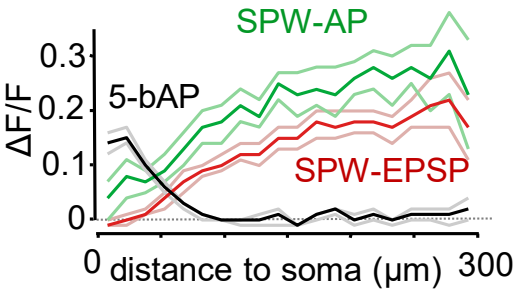

Figure 17. *Distribution of Ca^{2+} responses along dendrite.* Average SPW-EPSP (red), SPW-AP (green, with 1 AP) and bAPs (black, 5 APs) induced 3D Ca^{2+} responses as a function of distance from the soma. Mean ± s.e.m., n=5 cells. Backpropagating APs were induced by somatic current injection between SPW events.

The amplitude of the dendritic 3D Ca^{2+} responses elicited by bAPs (5 APs, 40 Hz) decreased rapidly as a function of distance, dropping below the detection threshold at 113.88±14.50 µm (n=13; **Figure 17**) from the soma, consistent with recently published data [82, 89, 92]. These data can be explained by the passive properties of FS-PV INs dendrites, which are dampened by a high K^+ to Na^+ conductance ratio [75, 82, 102]. In contrast to somatically-evoked bAPs, the amplitude of dendritic 3D Ca^{2+} responses occurring during spontaneous SPW-R associated APs (SPW-APs) progressively increased as a function of distance from the soma (**Figure 17**). Moreover, a similar, incremental response could be measured during subthreshold events when SPW-R activity did not induce somatic APs. In this case the 3D Ca^{2+} response was close to zero at the soma, suggesting a dendritic rather than somatic origin for these signals (**Figure 17**). Interestingly, the SPW-EPSP-associated dendritic Ca^{2+} signals invaded the majority of the distal apical but not the basal dendritic arbor (**Figure 18**), however it might be different under *in vivo* conditions.

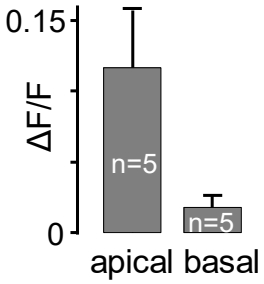

Figure 18 *Average Ca^{2+} responses from different dendritic regions.* Average apical and basal dendritic Ca^{2+} signals during SPW-EPSPs (mean±s.e.m., n=5 cells).

The distance-dependent distribution of 3D Ca^{2+} responses to bAPs and to SPW-EPSPs showed a reciprocal pattern (**Figure 17**), These data suggest that network activity during SPW-Rs can shift

DOI:10.15774/PPKE.ITK.2021.008

the status of FS-PV INs from their well-characterized ground state where dendrites are passive [75, 85-89] to an 'excited' state where regenerative dendritic activity such as dendritic Ca^{2+} spikes may occur.

The previous definitions strongly indicate that dendritic spikes exist in FS-PV INs during SPW-Rs if:

- spikes are detectable in the membrane potential signal
- spike initiation is dendritic in origin
- spikes actively propagate into neighboring dendritic segments
- spikes are initiated in an all-or-none manner above a well-defined threshold
- spikes are mediated by voltage-gated ion channels.

The first could be easily addressed by studying the somatic membrane potential in relation to the simultaneously recorded Ca^{2+} responses. However, a large event-to-event variability was noticed in the amplitude of the dendritic Ca^{2+} signal (**Figure 19**); specifically, SPW-EPSPs with long oscillating plateau-potentials were occasionally accompanied by Ca^{2+} events larger than those of SPW-APs (**Figure 19**).

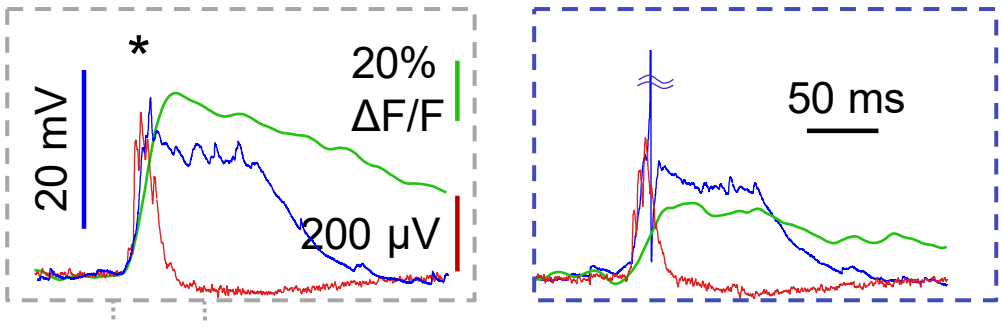

Figure 19 *Overlaid Ca^{2+}, LFP and whole cell membrane potential traces.* The green graph represents the spatially integrated dendritic Ca^{2+} response while the simultaneously recorded somatic membrane potential is in blue and the local (CA1) field potential trace (LFP, str. pyramidale) appears in red.

This oscillation-like behavior of the somatic membrane potential (interneuronal ripple oscillations) could be captured by the baseline subtraction method and with short-time Fourier transforms (spectrogram, 0-500 Hz) of the somatic membrane potential (**Figure 16**). The oscillation frequency of SPW-EPSPs increased rapidly before the peak of SPW-EPSPs (**Figure 16**), had a maximum at the peak (f_{max} 270.3 ± 18.18 Hz, n=11), then decreased at a slower rate below 239.97±19.25 Hz, while its duration extended 17.1±3.19 ms beyond the termination of the network LFP signal (LFP_{FWHM} 12.23±1.85 ms, $EPSP_{FWHM}$ 29.37±2.49 ms, p=0.0001). These data provide evidence that individual neurons can generate additional membrane oscillations after the network oscillations have already terminated. Moreover, in over 50% of the cells we

DOI:10.15774/PPKE.ITK.2021.008

simultaneously recorded SPW-EPSPs and LFP traces whose phases, frequencies and amplitudes did not correlate (**Figure 20A**), despite the fact that average of SPW-EPSPs and LFP signals correlated well **(Figure 20B**). As these data also suggested that intrinsic membrane mechanisms may contribute to the generation of the dendritic Ca^{2+} spikes and accompanying interneuronal ripple oscillations; therefore, the relationship between the oscillations and Ca^{2+} responses were further investigated.

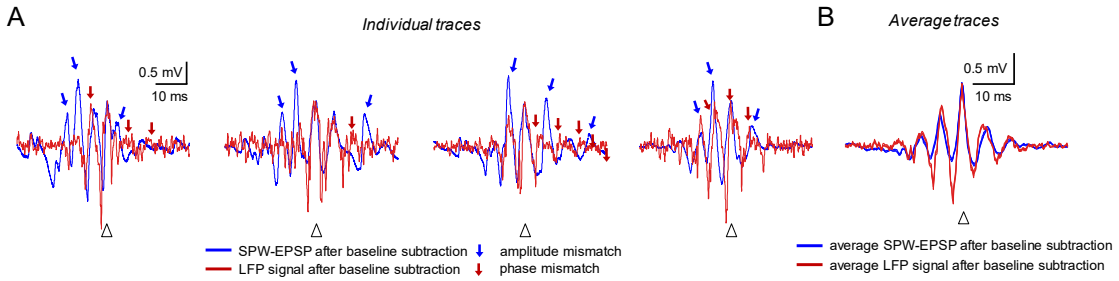

Figure 20 *Comparison of membrane potential and LFP signals for individual and average cases.* Individual SPW-EPSPs (blue) and LFP signals (red) recorded simultaneously in a FS-PV IN. The baselines were subtracted using the baseline subtraction method as before. Note the amplitude (blue arrows) and phase (red arrows) mismatches between the SPW-EPSP and LFP traces. (**F**) Average (mean ± s.e.m) of 20 traces recorded in the FS-PV IN. Traces in E are also included. Note that averaging eliminated the amplitude and phase mismatches.

The amplitude of SPW-EPSP-associated Ca^{2+} responses correlated well with the power of interneuronal ripple oscillations in individual dendritic segments and also in spatial averages across dendrites. Baseline-corrected and peak-aligned SPW-EPSPs and SPW-APs showed interneuronal ripple oscillations with similar frequency and phase values (239.97±19.25 Hz and 239.70±11.60 Hz, respectively, $p>0.3$, $n=11$). Moreover, the output of FS-PV INs was tightly phase-locked to these interneuronal ripple oscillations (**Figure 21**). This also means that putative dendritic spikes induced by synchronized network activity transiently switch the input-output transformation function of FS-PV INs from a submillisecond scale to a slower integration scale, where interneuron output is gated in phase synchrony with membrane ripple oscillations.

DOI:10.15774/PPKE.ITK.2021.008

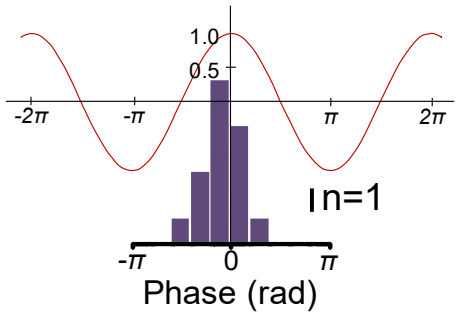

Figure 21 *Firing of FS-PV INs is phase-locked to interneuronal ripple oscillations.* Binned firing probability relative to the phase of the subthreshold interneuronal ripple oscillations (n=17 cells).

High-speed 3D trajectory scanning was used to define the dendritic origin of the putative Ca^{2+} spikes. Long apical segments were examined in the distal dendritic zone (up to 308 µm distance from the soma; **Figure 22**), where the amplitude of 3D Ca^{2+} responses induced by five bAPs is reduced below the detection threshold (**Figure 22**). As shown above, large 3D Ca^{2+} responses associated with either SPW-EPSPs or SPW-APs effectively invaded these apical dendritic segments and had simultaneous local maxima ("hot spots") in several segments (**Figure 22**). The relevance of hot spots is further supported by the fact that although the occurrence of APs boosted the dendritic 3D Ca^{2+} response in the measured distal segments evenly by 41.3±2.9 % (n=5 cells over 150 µm distance; **Figure 22**), the location of hot spots remained well preserved.

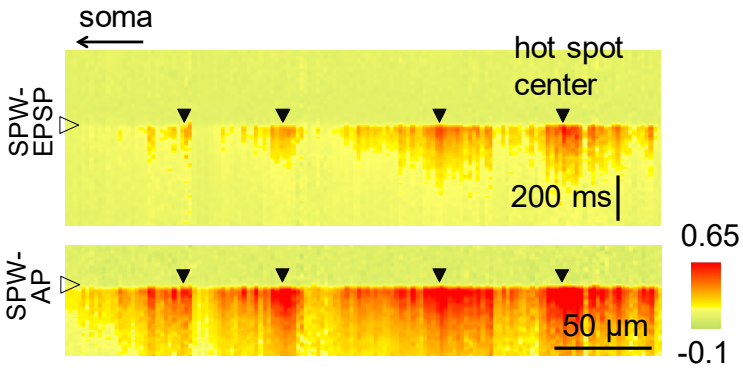

Figure 22 *Ca^{2+} activity during SPW activity*. Average SPW-EPSP and SPW-AP associated Ca^{2+} responses, recorded simultaneously in apical dendritic segments. Local maxima of activity were identified as "hot spot" regions (black triangles).

Another key element of proving dendritic spikes is the active propagation of the putative spikes from their dendritic initiation sites to the adjacent dendritic segments. To achieve this goal, the speed of 3D acousto-optical scanning was further increased by reducing the number of simultaneously measured locations and by applying our previously developed temporal super-

DOI:10.15774/PPKE.ITK.2021.008

resolution method [96]. The subthreshold SPW-EPSPs were only selected for analysis in order to avoid the effect of interactions with somatic APs. As the SPW-EPSP-associated 3D Ca^{2+} responses typically showed simultaneous hot spots in more than one dendritic segment (**Figure 22**), we selectively measured fast propagation from these multiple hot spots to neighboring dendritic segments. The 3D Ca^{2+} responses were not only larger in the hot spots (333±51 %, n=17 regions in n=9 cells), but they were also preceded by 12.8±2.4 ms the Ca^{2+} signals in the adjacent dendritic segments (41.5±12.7 µm from the center of the hot spot). Supporting the regenerative nature of the dendritic spikes, the propagation speed from the center of the hot spots toward the soma could be clearly measured in 68.8±8.2 % of long dendritic segments (222.1±63.0 µm, n=13, **Figure 23**), yielding an average propagation speed of 34.22 ± 4.32 µm/ms.

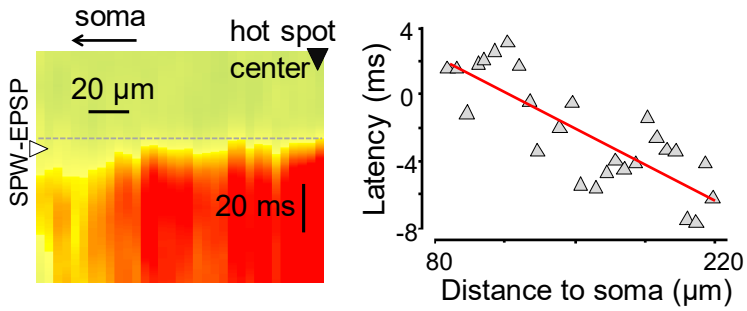

Figure 23 *Ca^{2+} propagation speed in dendrites during SPW.* Propagation of the SPW-EPSP-associated Ca^{2+} signal from the center of the hot spot (Figure 22) toward the soma. (Right) Corresponding onset latency times as a function of distance along the dendrite. Red line is a linear fit (r=0.65).

The measured high propagation speed is not compatible with Ca^{2+} diffusion, which is much slower at these large dendritic distances [22, 66, 87, 103]. These data indicate that the SPW-R-associated and broadly distributed Ca^{2+} signals demonstrated above are regenerative dendritic events with active propagation. In the following Results Part I applied DNI-Glu•TFA to evoke regenerative dendritic events to define the ion channel contribution and the characteristics of these events.

DOI:10.15774/PPKE.ITK.2021.008

2. MATERIAL AND METHODS

2.1. SLICE PREPARATION AND ELECTROPHYSIOLOGY

All experiments were carried out in accordance with the Hungarian Act of Animal Care and Experimentation (1998; XXVIII, section 243/1998.). A transgenic mouse line [98] was used to selectively identify FS-PV INs. Acute hippocampal slices were prepared from 15 to 30-day-old transgenic mice expressing enhanced green fluorescent protein controlled by the parvalbumin promoter[92, 98]. The animals were deeply anesthetized with isoflurane and then decapitated. The brain was quickly removed from the skull and put into an ice cold cutting solution[92]. Horizontal brain slices (thickness: 300 μm) were cut with a vibratome (Vibratome 3000). The slices were then stored at room temperature (23-25 °C) in standard artificial cerebrospinal fluid containing (in mM): 126 NaCl, 2.5 KCl, 2 $CaCl_2$, 2 $MgCl_2$, 1.25 NaH_2PO_2, 26 $NaHCO_3$ and 10 glucose and bubbled with carbogen gas[66, 92].

During the two-photon uncaging and pharmacological experiments we used a regular submerged chamber (Luigs & Neumann, Ratingen, Germany) to deliberately suppress network activity and SPWs. Whole-cell current-clamp recordings and LFP measurements (MultiClamp 700B, Digidata 1440: Molecular Devices, Sunnyvale, CA, USA) were made at 32-34 °C (in-line heater: Supertech; chamber heater: Luigs & Neumann). LFPs were recorded (with 1-3 kHz sampling rate) from the CA1 region of the hippocampus with glass electrodes (6-9 MΩ) filled with artificial cerebrospinal fluid and then band pass filtered (1-500 Hz). FS-PV INs in the CA1 pyramidal region were visualized for targeted patch-clamp recordings with infrared oblique illumination (at 880 nm) and two-photon imaging (830 nm). Whole cell recording was performed with 6-9 MΩ resistance borosilicate glass electrodes filled with an intracellular solution containing (in mM): 125 K-gluconate, 20 KCl, 10 HEPES, 10 Di-Tris-salt phosphocreatine, 0.3 Na-GTP, 4 Mg-ATP, 10 NaCl, 0.008 biocytin. Patch pipettes also contained 100 μM Fluo-4 (Invitrogen, Budapest, Hungary) or 60 μM Oregon Green BAPTA-1 (OGB-1, Invitrogen), all in combination with 100 μM Alexa Fluor 594 (Invitrogen). Only cells with a resting membrane potential more negative than −55 mV were accepted.

The passive intrinsic membrane properties of FS-PV INs were measured in whole-cell current-clamp configuration[83, 104]. The resting membrane potential was estimated during the absence of holding current. Input resistance and the membrane time constant were calculated from voltage responses to current injections (500 ms, 50 pA). The AP properties (e.g. half width) were measured at the first AP evoked by increased depolarizing current injection. To determine the AP accommodation, we increased the somatically injected current until the cell reached the maximal

DOI:10.15774/PPKE.ITK.2021.008

firing frequency (~800pA, 500ms). The accommodation was determined as the frequency difference between the frequency of the first and the last 100 ms time intervals. Five bAPs were induced with somatic current injections (500-700 pA for 5 ms, five current steps at 40 Hz). Data were recorded with pClamp10 (Molecular Devices, Sunnyvale, CA, USA) and MES v4.5 (Femtonics Ltd., Budapest, Hungary) software.

2.2. PHARMACOLOGICAL EXPERIMENTS

The sigmoid-like increase in the temporal width of the uncaging-evoked EPSPs as a function of the number of active inputs suggested that an NMDA receptor-mediated mechanism contributed to the dendritic spike. Moreover, the propagating nature of Ca^{2+} responses, and the extended Ca^{2+} plateaus, argued that voltage-gated Ca^{2+} channels (VGCCs) could have a role, while the fast kinetics of interneuronal ripple oscillations suggest that voltage-gated Na^{+} channels contribute. Therefore, we investigated the role of VGCC, L-type VGCC, NMDA, AMPA, and Ca^{2+}-permeable AMPA receptors.

All drugs were applied in the bath. Tetrodotoxin (TTX) (1 μM), nimodipine (20 μM), mibefradil (10 μM), ω-connotoxin MVIIC (0.5 μM), CNQX (10 μM), and DL-AP5 (60 μM) were purchased from Tocris Bioscience. The cocktail of VGCC blockers contained ω-connotoxin MVIIC, nimodipine, and mibefradil. During local TTX experiments we injected 10 μM TTX in combination with Alexa 594 using a patch pipete (6-9 MΩ).

2.3. TWO-PHOTON UNCAGING EXPERIMENTS

DNI-Glu•TFA (2.5 mM) was applied in the bath. The photolysis of DNI-Glu•TFA was performed at 740 nm using a second ultrafast pulsed laser (Mai Tai, SpectraPhysics). Laser intensity was set using an electro-optical modulator (model 350–80 LA; Conoptics) after beam expansion (1:2, Thorlabs). The laser light was directly coupled into the pathway of a two-photon microscope (Femto2D, Femtonics Ltd.) with two motorized mirrors and a polarization cube (PBS10; Thorlabs). The four degrees of freedom provided by the two motorized mirrors allowed precise positioning of the uncaging focal spot relative to the imaging focal spot (<50 nm radial and < 300 nm axial errors). Imaging was interleaved with short uncaging periods during which the uncaging focal spot was jumped to the preselected locations in jump times of 40-50 μs. Single-spot uncaging laser intensity was set to previously reproduced unitary EPSPs induced by local puffed high osmolar ACSF [22]. Fluorescent data values, collected during these uncaging periods, were used to monitor and correct uncaging positions relative to the imaged dendritic segment. Single-spot uncaging laser intensity was set to reproduce unitary EPSPs induced by local injection of high osmolar artificial cerebrospinal fluid [22], at similar distances from the soma where spontaneous activity was detected (amplitude of high osmolar artificial cerebrospinal fluid-

DOI:10.15774/PPKE.ITK.2021.008

induced EPSPs was 0.71±0.06 mV, n=4). When recording the input-output curves of neurons, uncaging at the maximum number of selected locations (43.8 ± 2.9) was allowed first, then the inputs were gradually but randomly removed. Inputs were sequentially activated because the use of more complex sequences of active inputs in the same total uncaging time window did not cause any significant difference in the response amplitudes. Finally, uncaging with the maximum input number was repeated at the end of each experiment, and only experiments with the same final and initial maximum amplitude were accepted.

With the application of DNI-Glu•TFA, it became possible to rapidly and repetitively activate the required high number of unitary inputs (up to 60) in a short time period (4.39±0.32 ms, n=35 cells) without inducing a detectable level of phototoxicity in the dendrites. The trajectory of long dendritic segments (53.5±2.9 μm) was rapidly scanned (at 170-500 Hz) and, after a 500 ms baseline period, DNI-Glu•TFA was uncaged at up to 60 locations in each sweep. We characterized each cell's input-output function by plotting the simultaneously-recorded Ca^{2+} and somatic voltage responses as a function of the progressively increasing input number, until the density of active inputs reached 1.36±0.09 synapses/μm, corresponding to the reported excitatory synapse density (1-5 synapses/μm) of FS-PV INs [105]. The clustered active input pattern covered, on average, an 18.3±1.4 μm long dendritic segment (termed hot-spot region) on the apical dendritic tree in the distal dendritic region (235.4±63.5 μm, from the soma; mean ± s.d.), where large spontaneous SPW-EPSP-associated 3D Ca^{2+} responses were usually detected. The single site uncaging time was set to reproduce the amplitude of miniature EPSPs induced with high-osmolarity artificial cerebrospinal fluid (0.71±0.06 mV, n=4) puffed at the same distance from the soma.

2.4. DETECTION OF INTERNEURONAL RIPPLE OSCILLATIONS WITHOUT FILTERING ARTIFACTS USING THE BASELINE SUBTRACTION METHOD

To avoid these errors, we used off-line Gaussian filtering (100 Hz) on the raw whole-cell traces to generate a "baseline", which was then subtracted from the raw traces to preserve ripple oscillations. In contrast to band-pass filtering, the baseline-subtraction method did not generate any extra oscillation cycles, phase shifts, or false oscillations from the relatively slow depolarizing humps which characterize SPW-associated EPSP. Therefore, the baseline-subtraction allowed us to detect individual ripple oscillation cycles in the somatic membrane voltage with the required phase and amplitude precision (**Figure 25**). The ripple frequency of individual traces and averages was determined either by Fourier transformation (f_{Fourier}) or by measuring the time between oscillation peaks after baseline subtraction in an interval centered on the peak of raw events (f_{max}).

2.5. DATA ANALYSIS AND STATISTICS

DOI:10.15774/PPKE.ITK.2021.008

Analysis was performed with a MATLAB-based program (MES, Femtonics) using custom-written software elements. The 3D raw fluorescent data (*F*) were collected along the dendrite, spatially normalized and then projected into a two-dimensional plot (defined as 3D Ca^{2+} responses) by applying the formula

$$\Delta F/F=(F(d,t) - F_0(d))/F_0(d) \quad \textbf{Eq. 12},$$

where *d* denotes the distance along the dendrite and *t* indicates time. $F_0(d)$ denotes background fluorescence as a function of distance along the dendrite. When 3D Ca^{2+} responses were simultaneously collected from multiple dendritic segments, the data were consecutively projected into the same two-dimensional frame and responses from different segments were separated by dashed lines. As it is indicated, in some measurements the color look up table (LUT) was shifted to higher ΔF/F values in order to better reveal the location of dendritic hot spots.

Sublinear dendritic integration was fitted using the following equation:

$$y_1 = A_1(1 - e^{(-A_2*(x-A_3)})} \quad \textbf{Eq. 13}$$

where *x* denotes number of glutamatergic inputs, A_i are fitting parameters and *y* is the output.

Boltzmann fit of supralinear jumps in input-output curves was either performed using Equation 14 alone:

$$y_2 = \frac{A_4}{1+e^{\left(\frac{x-A_5}{A_6}\right)}} + A_7 \quad \textbf{Eq. 14}$$

or, alternatively, when the initial part of the input-output curve showed a clear sublinear tendency, first this sublinear period was fitted and subtracted from the whole input-output curve using **Eq. 13**, and **Eq. 14** was used only thereafter. We also attempted to fit the data by not subtracting **Eq. 13** but adding it to **Eq. 14**.

DOI:10.15774/PPKE.ITK.2021.008

3. RESULTS

3.1. SPATIALLY AND TEMPORALLY CLUSTERED INPUTS GENERATE THE DENDRITIC SPIKES

In order to find the minimum number of excitatory inputs that are needed to evoke the regenerative event in an all-or-none manner, we simulated excitatory inputs by using two-photon glutamate uncaging in short, temporally and spatially clustered patterns [16]. This method allowed the selective measurement of postsynaptic mechanisms and avoided any potential variability due to presynaptic mechanisms. In addition, the contribution of network activity was deliberately decreased in these experiments by using a conventional recording chamber with a normal perfusion rate (6.5 ml/min), conditions that prevent spontaneous SPW generation in regular acute slices. To model the long-lasting and large-amplitude SPW-EPSPs (29.37±2.49 ms, 22.6±1.7 mV, **Figure 19**) from small unitary inputs (< 1 mV) [106], tens of unitary inputs must be activated in a short time window. However, the quantum efficiency of the widely used MNI-glutamate was not high enough to repetitively activate such a high number of clustered inputs in the time window of ripple oscillations (5-6 ms) without causing photodamage in consecutive measurements. Therefore, we used DNI-Glu•TFA, which has 7 times higher two-photon uncaging efficiency than MNI-glutamate. With the application of DNI-Glu•TFA, it became possible to rapidly and repetitively activate the required high number of unitary inputs (up to 60) in a short time period (4.39±0.33 ms, n=35 cells) without inducing a detectable level of phototoxicity in the dendrites. The trajectory of long dendritic segments (53.5±2.9 µm) was rapidly scanned (at 0.5 kHz) and after a 500 ms baseline period, DNI-Glu•TFA was uncaged at up to 60 locations. We characterized each cell's input-output function by plotting the simultaneously recorded Ca^{2+} and somatic voltage responses as a function of the progressively increasing input number until the density of inputs reached 1.36±0.09 synapses/µm, corresponding to the reported excitatory synapse density (1-5 synapses/µm) of FS-PV INs [96]. The clustered input pattern covered on average a 18.3±1.4 µm long dendritic segment (input region) on the apical dendritic tree in the distal dendritic region (239.4±11.0 µm from the soma) where the large spontaneous SPW-EPSP-associated Ca^{2+} responses were detected. The single site uncaging time was set to reproduce the amplitude of miniature EPSPs induced with high-osmolarity artificial cerebrospinal fluid (0.71±0.06 mV, n=4) puffed at the same distance from the soma. In contrast to the expected linear or sublinear dendritic input-output transformation demonstrated earlier in FS-PV INs [82, 102] and two types of cerebellar interneurons [107, 108], the uncaging-evoked Ca^{2+} signal in the input region showed a step-like nonlinear increase (**Figure 24 A-D**) at a given threshold input number, defined as the first threshold (9.17±1.2 inputs, n=6 cells), followed by a more modest increase at a slower rate at a progressively increasing input number.

DOI:10.15774/PPKE.ITK.2021.008

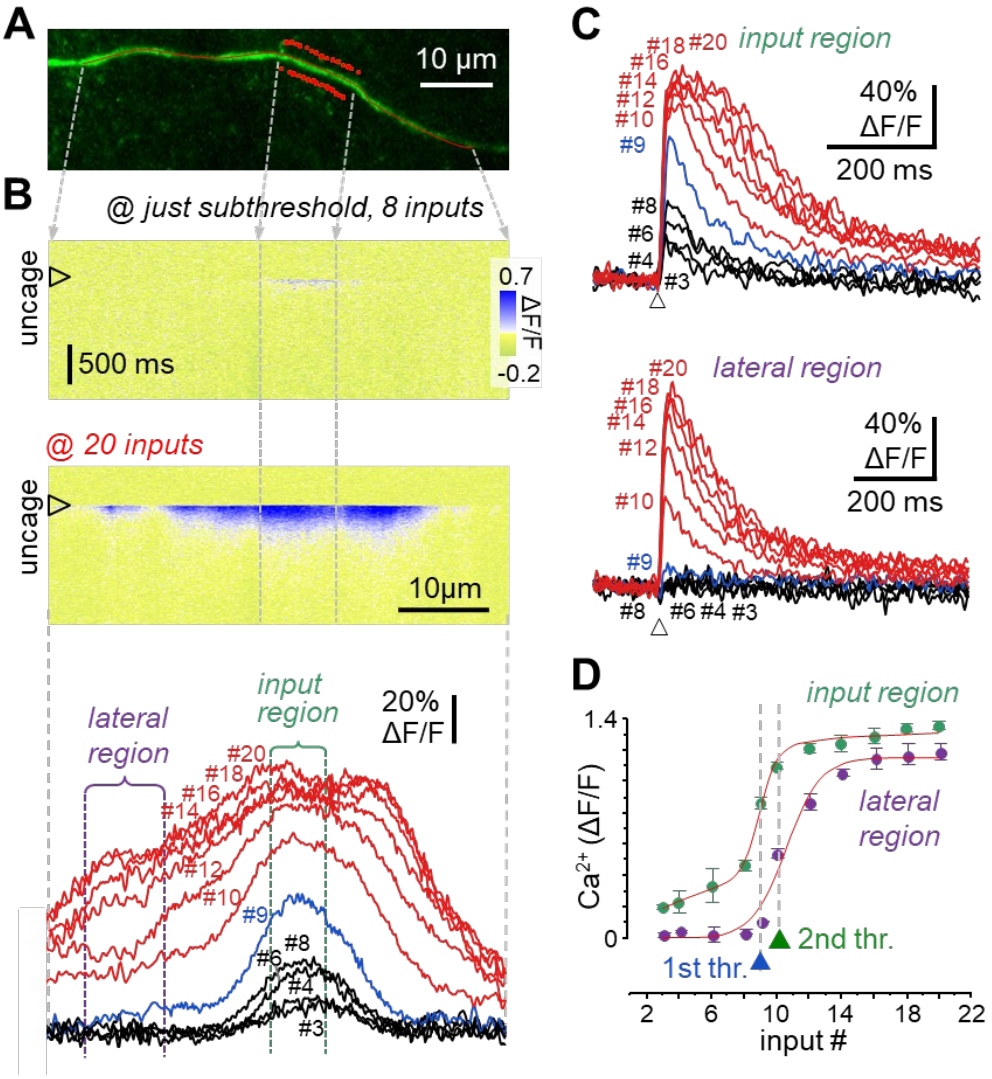

Figure 24 *Synchronous activation of clustered glutamatergic inputs reproduces SPW-R-associated dendritic Ca^{2+} spikes.* (**A**) Maximum intensity z-projection image of a dendritic segment of a FS-PV IN selected for two-photon imaging and uncaging. Red points are input locations used for patterned two-photon glutamate uncaging in the presence of 2.5 mM DNI-Glu•TFA. Red line shows the long scanning trajectory. (**B**) Average Ca^{2+} responses (n=5) induced by uncaging with a just-subthreshold input number (8 inputs, top) and at suprathreshold input number (20 inputs, middle). (Bottom) Spatial distribution of the peak Ca^{2+} responses at an increasing number of inputs (averages of 10 responses). (**C**) Ca^{2+} transients derived at the input (top) and at the lateral dendritic (bottom) regions in A at an increasing number of inputs (bottom). (**D**) Mean peak Ca^{2+} responses (n=4 measurements) as a function of input number in the input and lateral dendritic regions. Boltzmann fits (**Eq.14**) are shown in red.

Interestingly, the first threshold was followed by a separate second threshold (**Figure 24D**) which was best visible in the lateral dendritic region (outside of the input zone, **Figure 24, B to D**) where the uncaging-evoked Ca^{2+} signal showed a sigmoid-like increase, at 27.0±5.6 excitatory inputs

DOI:10.15774/PPKE.ITK.2021.008

(second threshold, range 10-47, n=6 cells). The simultaneously-recorded somatic membrane potential remained below the AP threshold (**Figure 25**).

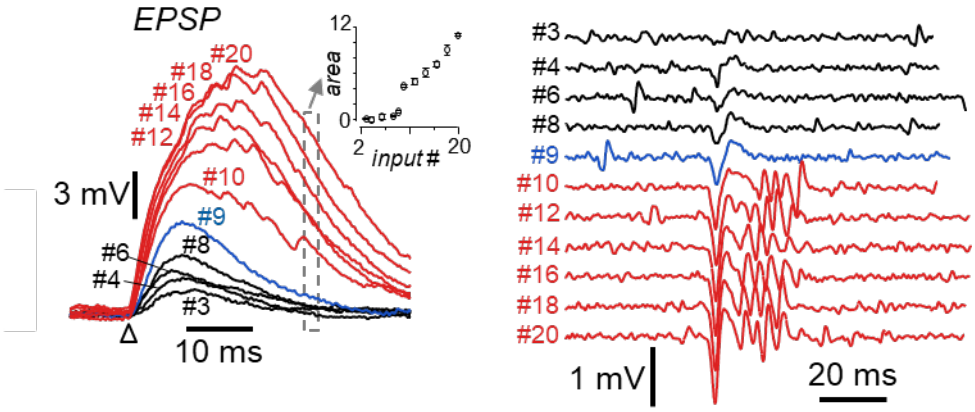

Figure 25 *EPSP amplitudes versus uncaging input numbers.* Corresponding individual EPSPs without (left) and with (right) baseline subtraction demonstrate the occurrence of ripple oscillations at 270.3±9.1 Hz. Inset shows EPSP integral calculated in the boxed region versus number of inputs.

Moreover, the spatial distribution of the Ca^{2+} increase in the lateral dendritic regions showed a 'plateau-like' characteristic above the second threshold (**Figure 24B**). Although this Ca^{2+} plateau slightly decreased as a function of distance from the input region, it reproduced the large, spontaneous SPW-EPSP-associated Ca^{2+} responses (**Figure 24B**). If this Ca^{2+} plateau in the lateral dendritic region indeed represents a regenerative spike, active propagation should also be present. Indeed, we could measure a propagation speed of 17.4±3.6 µm/ms (**Figure 26**) in 85.1±16.4 µm-long dendritic segments (n=5 cells), which is similar to the propagation speed of the large, spontaneous SPW-EPSP-associated dendritic 3D Ca^{2+} responses, and is much higher than expected from Ca^{2+} diffusion alone at these distances [22, 66].

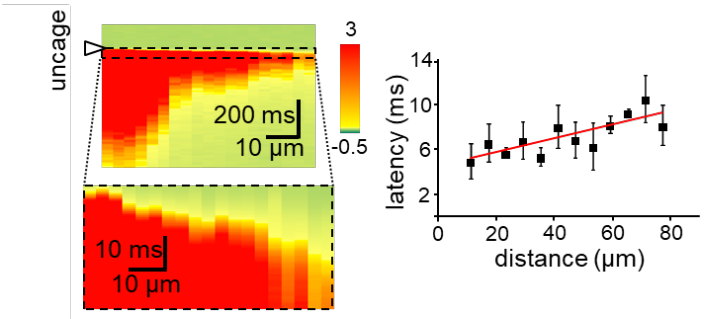

Figure 26 *Uncaging-evoked Ca^{2+} signal propagation speed measurement.* (Left) Propagation of a somatically subthreshold dendritic Ca^{2+} spike from the input region toward the lateral dendritic region. (Right) Corresponding Ca^{2+} signal onset latency times as a function of distance along the dendrite. Linear fits are shown in red.

DOI:10.15774/PPKE.ITK.2021.008

The difference in the propagation speed between SPW-EPSP-associated Ca^{2+} responses (**Figure 26**) and uncaging-evoked Ca^{2+} signals could be explained by the lack of activated synaptic inputs in the lateral dendritic regions upon uncaging, which may increase the local voltage threshold. Indeed, Ca^{2+} responses were larger when the activated inputs were more widely distributed along the dendrite (**Figure 27**).

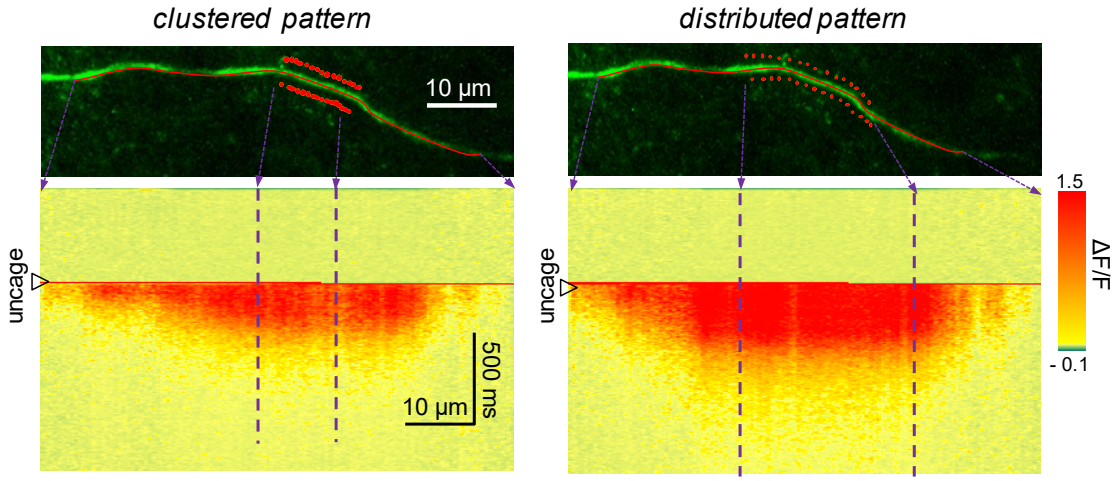

Figure 27 *Ca^{2+} response amplitude during clustered and distributed uncaging patterns.* (Top) Maximum intensity z-projection image of the imaged dendritic segment with the 32 input locations (red dots). Red line shows the scanning trajectory. (Bottom) Average Ca^{2+} response (n=9 traces) measured along the red line. Arrows show corresponding locations.

These data are in good agreement with the increased AP back-propagation during SPW-Rs (**Figure 17**) when dendrites are bombarded with high number of EPSPs.

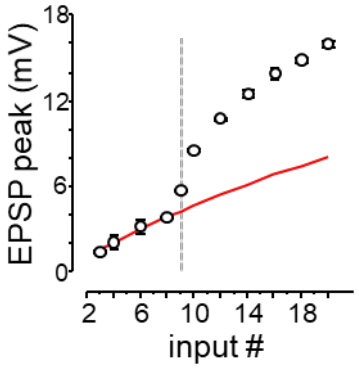

Figure 28 *Input-output characteristic of FS-PV Ins.* EPSP peak versus the number of inputs (mean ± s.e.m., n=4 measurements). The sublinear integration, below the threshold, was fitted using **Equation 13**.

To establish, how the uncaging-induced Ca^{2+} spikes were reflected in the simultaneously recorded somatic membrane potential, we first investigated the input-output characteristics of FS-PV INs. The initial linear (**Figure 25 & 28**) or sublinear increase in the amplitude of the somatic EPSPs

DOI:10.15774/PPKE.ITK.2021.008

was followed by a step-like increase at the second threshold input number (determined above by Ca^{2+} imaging), and the amplitude progressively increased thereafter as a function of increasing input number at a slower rate above the second threshold (**Figure 28**). When the second threshold input number was higher (above ~15 inputs), an initially sub-linear increase in the input-output function (instead of linear increase) was revealed, on which a sigmoid-like increase was superimposed at the second threshold input number. This sigmoid-like increase was similar to the previous, low input threshold case and was also combined with a simultaneously occurring Ca^{2+} increase in the input and lateral dendritic regions. A similar sub-linear integration rule of EPSPs, but without the step-like increase, has also been demonstrated in other interneurons in silent acute slices [107, 108]. Somatic interneuronal ripple oscillations could be detected in 17 out of 35 cells (48.57%), above the second threshold. The evoked oscillation, in eleven cells, proved to be robust and stable, and its frequency (219.3±14.9 Hz) well approximated the interneuronal ripple oscillation frequency of spontaneous SPW-EPSPs (239.9±19.3 Hz). When the input number was increasing progressively, the evoked oscillation onset latency became shorter and interneuronal ripple oscillations varied less in amplitude and phase; nevertheless, the frequency of evoked interneuronal ripple oscillations did not change ($p>0.38$) at all. The frequency of evoked interneuronal ripple oscillations was similar for both spatially clustered and distributed activation patterns ($p=0.23$). However, distributed input patterns induced ripple oscillations in more dendritic segments (73.68%, 14/19 segments in 14/19 cells) and produced more oscillation cycles upon each induction. Finally, we investigated the functional relevance of interneuronal ripple oscillations. Since the distribution of AP times relative to interneuronal ripple oscillations was much narrower than the distribution relative to the EPSP onset time (**Figure 29**), we concluded that AP output is more strongly coupled to interneuronal ripple oscillations than EPSPs, which is in good agreement with our spontaneous SPW-R-associated data (**Figure 21**).

DOI:10.15774/PPKE.ITK.2021.008

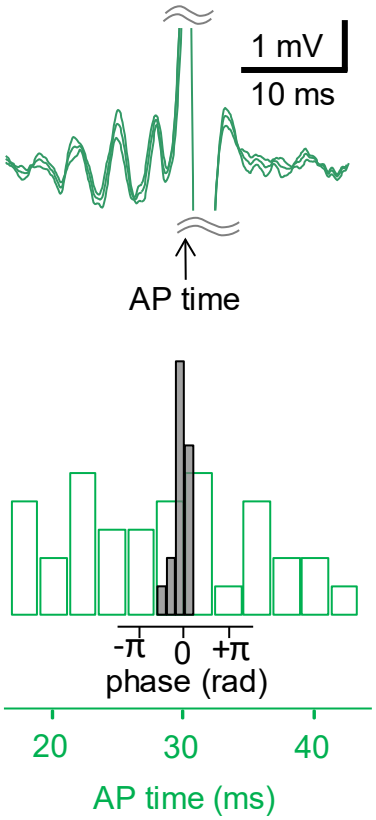

Figure 29 *AP output coupling to interneuronal ripple oscillation* (Top) Average suprathreshold voltage responses (mean ± s.e.m.) induced by 59 inputs, baseline-subtracted and aligned to the peak of the AP. (Bottom) Histogram of AP timing relative to the phase of interneuronal ripple oscillation (gray, n=18) and relative to the EPSP onset time (green, n=36). The two different x-axes were overlaid according to the average interneuronal ripple oscillation frequency.

In order to investigate the functional role of different ion channels, we activated spatially and temporally clustered patterns of 43.8±2.9 inputs (above the second threshold, but below the threshold of somatic AP generation) at distal dendritic segments in control conditions and in the presence of various voltage- and ligand-gated ion channel blockers for comparison. The sigmoid-like increase in the temporal width of the uncaging-evoked EPSPs as a function of input number (**Figure 25**) suggests the contribution of an NMDA receptor-mediated mechanism to the dendritic spike. Moreover, the propagating Ca^{2+} responses (**Figure 23 & 25**) argue for the potential role of voltage-gated Ca^{2+} channels (VGCCs), and the fast kinetics of interneuronal ripple oscillations suggest the contribution of voltage-gated Na^{+} channels. The relative contribution of different types of ion channels may differ between the input region, where inputs are located, and the lateral dendritic region, where active propagation occurs. Therefore, we imaged long dendritic segments and activated the inputs at only one of the ends of the imaged segments (**Figure 30**) in order to provide long lateral dendritic regions for the measurements. These lateral dendritic regions of

DOI:10.15774/PPKE.ITK.2021.008

active propagation appeared in the spatial distribution of the Ca^{2+} amplitude as a plateau following a sharp drop in amplitude at the border of the input and lateral dendritic regions (**Figure 30**).

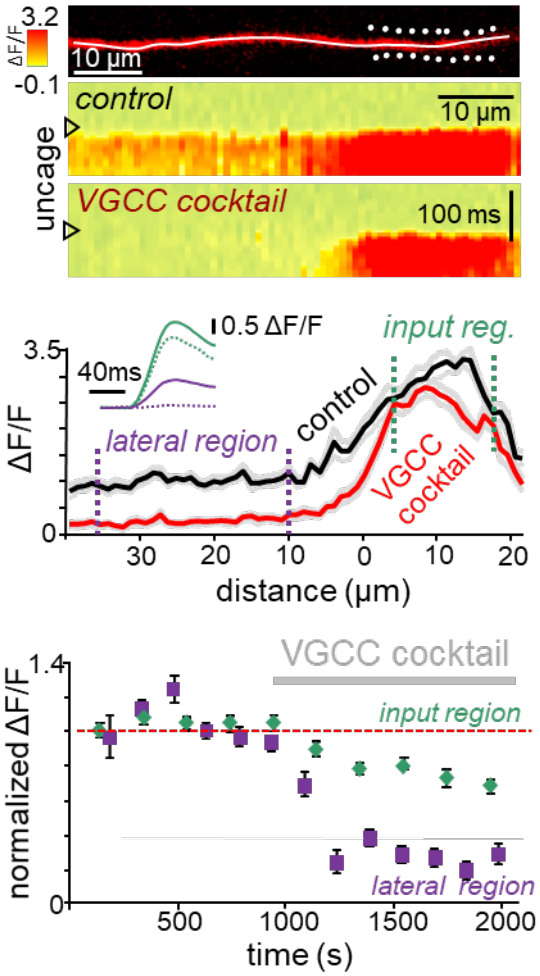

Figure 30 *Effect of VGCC blockers on uncaging-evoked Ca^{2+} responses.* (*Top*) Maximum intensity z-projection image of the distal dendritic segment of a FS-PV IN filled with Fluo-4 and Alexa-594. White points are input locations used for clustered two-photon glutamate uncaging in the presence of DNI-Glu•TFA (2.5 mM). The white line indicates the scanning path . Average uncaging-evoked Ca^{2+} responses in control condition (middle) and in the presence of a cocktail of VGCC blockers (Nimodipine, Mibefradil and ω-conotoxin MVIIC; bottom). (*Middle*) Spatial distribution of the peak dendritic Ca^{2+} response (mean±s.e.m.) measured along the white line in A in control conditions (black) and in the presence of the cocktail of VGCC blockers (red). Inset: mean Ca^{2+} transients derived at the input (green) and lateral dendritic (magenta) regions of the Ca^{2+} responses before (solid line) and after VGCC cocktail (dashed line). (*Bottom*) Time course of the effect of VGCC cocktail on Ca^{2+} responses in the input (green) and lateral dendritic (magenta) regions.

The mean effect of the VGCC, voltage-gated Na^+ channel, NMDA and AMPA receptor inhibitors was generally smaller in the input region as compared to the control values (TTX: 87.9±2.8 %, p=0.0036; AP5: 83.9±5.5 %, p=0.02; Nimodipine 71.6±3.3 %, p=0.0001; VGCC cocktail 75.2±4.8 %, p=0.0009; IEM-1460 72.7±8.3%, p=0.01; **Figure 31**), but the combined application

DOI:10.15774/PPKE.ITK.2021.008

of AMPA and NMDA receptor blockers (AP5 and CNQX) reduced the Ca^{2+} responses to almost zero (5.6±2.4 %, p=0.0004) (**Figure 31**).

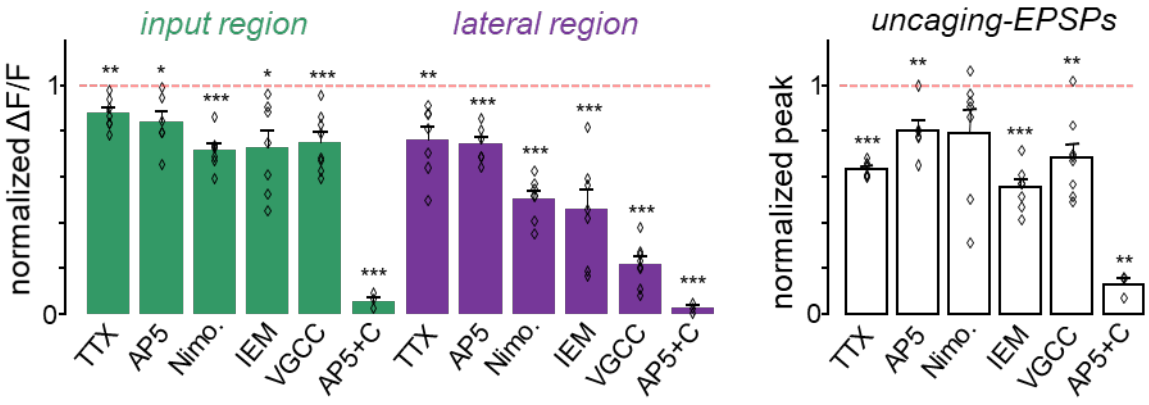

Figure 31 *Effect of different ion channel blockers* (*Left*) Effect of different ion channel blockers on the peak amplitude of Ca^{2+} transients derived from the dendritic Ca^{2+} responses in the input (green) and lateral dendritic (magenta) regions. (*Right*) The same as G, but for simultaneously recorded somatic EPSPs.

In the lateral dendritic region, the effects of ion channel inhibitors were stronger, and even the cocktail of VGCC blockers alone evoked a drastic reduction in the Ca^{2+} signal (TTX: 76.3±6.3%, p=0.006; AP5 74.4±3.7%, p=0.0006; Nimodipine 50.7±3.9%, p=0.00001; IEM-1460 46.0±9.4%, p=0.0008; VGCC 21.8±3.6%, $p=10^{-7}$; **Figure 31**). Here, the combined application of AP5 and CNQX decreased responses to a similar level to that of the input region (2.6 ± 1.6 %, p=0.0002; Figure 17). Our data indicate that VGCCs are mainly responsible for the Ca^{2+} influx in the lateral dendritic region, and thus for the dendritic Ca^{2+} spike. Hippocampal interneurons express P/Q-, R-, L-, N-, and T-type VGCCs [100], but we found that the L-type VGCC blocker Nimodipine had the greatest effect on the Ca^{2+} responses of FS-PV INs, both in the present study and in our earlier data [83]. In line with other observations, we noted that IEM-1460 (a blocker of Ca^{2+}-permeable AMPA receptors) also had a large effect on the postsynaptic Ca^{2+}-influx [67, 76, 78, 80, 91]. The amplitude and the area of the simultaneously recorded uncaging-evoked EPSPs were significantly decreased by all the ion channel blockers used (**Figure 31**). This change in the somatic EPSP likely reflects a similar change in the local dendritic voltage response, which may by itself affect the generation of membrane ripple oscillations. Therefore, when oscillations disappeared as a result of drug application, we compensated by increasing the uncaging laser intensity until the amplitude of the uncaging-evoked EPSPs reached the control value or interneuronal ripple oscillations reappeared.

DOI:10.15774/PPKE.ITK.2021.008

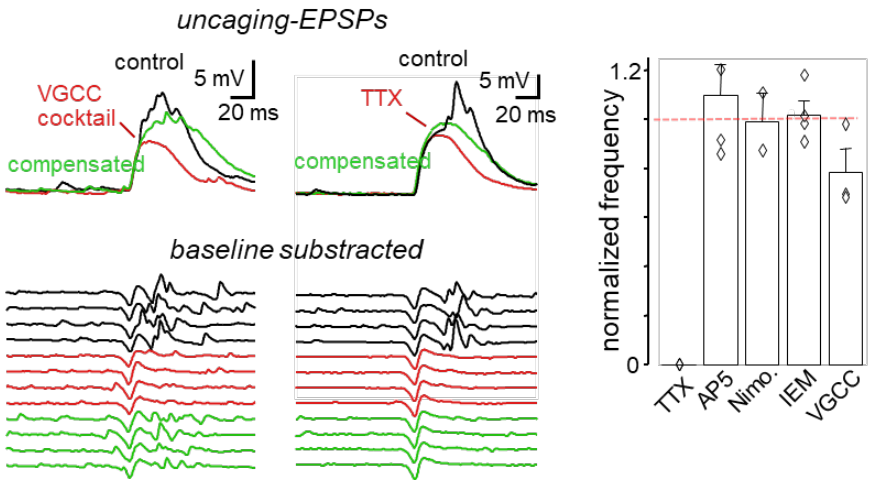

Figure 32 *Effect of ion channel blockers on interneuronal ripple oscillation* (*Left*) Subthreshold EPSPs showing interneuronal ripple oscillations with (bottom) and without (top) baseline subtraction in control conditions (black), but in absence of TTX and the VGCC blocker cocktail (red traces left and right respectively). When uncaging laser power was increased, interneuronal ripple oscillations were restored after application of VGCC blockers, but not for TTX (green traces left and right respectively). (*Right*) Normalized and pooled data for the effect of NMDA, Ca^{2+} permeable AMPA, VGCC and voltage-gated Na^{+} channel blockers on interneuronal ripple oscillations. Ripple oscillations were abolished only in the presence of TTX.

Almost in all the cases, the oscillations recovered (or remained stable), except for TTX, which completely eliminated interneuronal ripple oscillations, indicating their dependence on Na^{+} channel activation (**Figure 32**). In support of this, oscillation frequency did not change significantly in the presence of AP5, Nimodipine, IEM-1460, or the cocktail of VGCC blockers (control: 219.3±15.0 Hz, n=17; AP5: 275.9±48.3, n=4, p=0.13; Nimodipine: 256.7±75.4, n=3, p>0.4; IEM-1460 166.8±25.7, n=4; p=0.12; VGCC blocker cocktail: 186.7±4.4 Hz, n=3, p=0.37; Figure 32). Our results show that the propagating dendritic Ca^{2+} spikes are predominantly mediated by L-type Ca^{2+} channels, while the related interneuronal ripple oscillations are determined by voltage-gated Na^{+} channels. In summary, we conclude that dendritic regenerative events exist in FS-PV INs and DNI-Glu•TFA is a suitable compound to model it.

DOI:10.15774/PPKE.ITK.2021.008

4. DISCUSSION PART II

The above presented results are based firstly on our novel caged glutamate compound (DNI-Glu•TFA) and secondly on challenging the prevailing classical view of the functional role of FS-PV INs by showing a network-activity-dependent dynamic switch in dendritic integration mode. This changes the function of FS-PV INs during SPW-R events from a passive, fast, sublinear integrator role to an active mode where

i) supralinear dendritic integration of coincident inputs can generate robust, propagating Ca^{2+} spikes in apical dendritic segments of FS-PV INs

ii) dendritic spikes are associated with interneuronal ripple oscillations;

iii) dendritic spikes originate and propagate from multiple dendritic hot spots;

iv) the dual integration threshold reveals a three-stage input-output function;

v) AP outputs are phase-coupled to the interneuronal ripple oscillation.

The presence of Ca^{2+}-permeable AMPA, NMDA, voltage-gated Na^{+}, voltage-gated Ca^{2+}, and K^{+} channels in FS-PV INs dendrites was also demonstrated in earlier studies. These studies suggested that the main functional role of these channels is to provide fast electrical and Ca^{2+} signals that are spatially and temporally attenuated and well-compartmentalized [76, 82, 85]. This functional dampening and compartmentalization is thought to be required for the effective preservation of signal separation during sublinear integration at the very high speed characteristics of FS-PV INs. Similar passive cable properties and a sublinear signal integration rule were also demonstrated in other interneurons such as in cerebellar Golgi [107] and stellate cells [108] under conditions where spontaneous synaptic activity was similarly low. However, in the present study we recognized that these passive, well-dampened dendrites of FS-PV INs could be transiently activated by a high number of spatially and temporally coincident excitatory inputs during active network conditions. In this activated state several generally accepted and well-documented physiological properties of FS-PV INs change:

i) instead of the passive back-propagation, bAPs propagate actively and invade distal dendritic segments.

ii) There are dendritic spikes which cannot be elicited in the ground state [82].

iii) Supralinear dendritic integration replaces linear or sublinear summation.

iv) Dendritic voltage-gated Na^{+} channels, which are functionally inactive in ground state conditions [82], start to generate interneuronal ripple oscillations, which are associated with dendritic Ca^{2+} spikes.

DOI:10.15774/PPKE.ITK.2021.008

v) The well-compartmentalized synaptic Ca^{2+} signals are replaced by multiple propagating Ca^{2+} spikes originating from several hot spots in multiple dendritic segments.

vi) The AP output of FS-PV INs is tightly coupled to the phase of interneuronal ripple oscillations and the integration window becomes broader when compared to the submillisecond precision in EPSP-AP coupling that characterizes the ground state.

We demonstrated that Ca^{2+} spikes could be associated with membrane potential oscillations in a much higher, ripple frequency band and this resonance is actively mediated by TTX-sensitive Na^{+} channels. The appearance of the ripple oscillation seems to contradict the classical submillisecond integrator image of FS-PV INs because the output of FS-PV INs closely follows the ripple oscillation, instead of the tight EPSP-AP coupling which characterizes the ground state. The distance-dependent decrease in bAP amplitude and the simultaneous increase in dendritic spiking activity characteristic of pyramidal neurons [110, 111] was also reflected in FS-PV INs. Namely, bAP-induced Ca^{2+} signals disappeared beyond 100-150 μm in ground state, in good agreement with dendritic patch-clamp recording data [82], and gave way to Ca^{2+} spikes with a continuously-increasing amplitude as a function of distance. This functional separation of the distal spike zones and the axosomatic initiation zone increases neuronal computation capacity, as demonstrated in pyramidal neurons [112]. Although the origins of hippocampal SPW activity and associated ripple oscillations are contradictory, there is a consensus about several mechanisms. SPWs are considered as a population event based on an interplay between inhibitory and excitatory neuronal populations [78]. According to this model, a transient increase of pyramidal cell activity, generated autonomously in CA3, drives a widespread depolarization of both pyramidal cells and interneurons in CA1. This is directly responsible for the SPW and leads to the generation of network ripple oscillations through local interactions via chemical and/or electrical synapses [78, 99, 113-119]. More recently, smaller networks such as individual CA3 subfields [118] and CA1 (or CA3) minislices were shown to be capable of generating SPWs and associated network ripple oscillations [94, 114, 119]. In all cases, SPW-Rs have been considered as a network phenomenon [78]. A single FS-PV IN, and even a short (~20 μm long) segment of its dendritic arbor, when activated by approximately 30 coincident inputs, can generate fast oscillations in the ripple frequency range.

DOI:10.15774/PPKE.ITK.2021.008

CONCLUSIONS AND FUTURE PERSPECTIVES

In this dissertation I showed a novel caged compound (DNI-Glu•TFA), which was examined in different aspects and used in a series of neurobiological experiments. According to quantum chemical modeling, the molecule showed favorable and unfavorable properties as well. One of its most advantageous property is the high quantum efficiency (5-10 times more effective than commercially available MNI-Glu). This property is highly coupled with the possibility of spontaneous hydrolysis. If the quantum efficiency rises, the rate of spontaneous hydrolysis also increases. I introduced a method which can eliminate the product of hydrolysis. It allows us to use the compound in long-term experiments without any undesired effects. I also examined the antagonistic effect of DNI-Glu•TFA toward the GABA-A receptor and K+ channels. These side effects could also corrupt the experiment and change the delicate balance between excitatory and inhibitory components. I showed that the DNI-Glu•TFA has also no antagonist side effects. Besides quantum chemical modeling, quantum efficacy was also measured with neurobiological experiments. These experiments showed 5-7 times more two-photon efficacy compared to MNI-Glu. It means that the theoretical and the practical results are in good correlation. This compound was used in a complex neurobiological dendritic integration modeling as well. During hippocampal network 3D two-photon imaging and electrophysiological recordings, complex calcium patterns were observed on distal dendrites of FS-PV Ins. These dendritic spikes occurred when the spontaneous network activity was high in the acute brain slice. Moreover, these spikes could not be examined in active conditions. We also tested to use MNI-Glu, but the sensibility was not high enough to visualize the higher order calcium pattern activity. We also demonstrated that these dendritic spikes are mainly mediated by L-type VGCCs and the ripple component was mediated by Na+ channels. These delicate and complex measurements clearly represented the adequacy of DNI-Glu•TFA.

In the past few years, we have successfully synthetized more than 25 different glutamate and GABA analogues. These compounds show different properties like red-shifted absorption spectrum, increased two-photon efficacy or even exotic new perspectives [120]. We have moved to two different directions. Our first aim was to silence single neurons or smaller neuronal ensembles during epileptic-like activity in acute slices and in vivo as well. Therefore, we have developed a novel two-photon GABA compound called iDMPO-DNI-GABA. As a result of GABA uncaging we are able to modulate seizures to study the dynamics of epileptic-like activity. Another challenging task is to implement 3D whole cell imaging and uncaging. There is almost no data available in the literature about real-time whole cell information processing on dendritic level. The second project was to prove the existence of calcium dendritic spikes on FS-PV Ins in

DOI:10.15774/PPKE.ITK.2021.008

vivo conditions. This study is already submitted in Nature. Other recent studies have demonstrated that these cutting-edge methods help understand how the brain works. [120,121].

DOI:10.15774/PPKE.ITK.2021.008

III. THESIS STATEMENTS

1.1 The DNI-Glu•TFA has an increased 2PQE compared with MNI-Glu. Quantum chemical modeling is an excellent tool to select the proper caged glutamate candidate. I concluded that the 2PQE of DNI-Glu•TFA is 7 times higher (according to the calcium responses) and it allows to measure more precisely active regenerative dendritic processes.

Related publications: Pálfi et al., 2018.; Chiovini et al., 2014.

1.2 With enzymatic correction, spontaneous hydrolysis level was decreased for DNI-Glu•TFA. It is known that the most undesired process is the spontaneous hydrolysis for high QE compounds, which may result in dendritic swelling, intensive precipitation of the compound, robust changes in electrophysiological properties, or even toxicity. This process could prevent long-term measurements. Spontaneous activity was significantly decreased during enzymatic correction, which allowed us long-term dendritic calcium measurements. I showed in different experiments that enzymatic correction can stabilize the ambient glutamate level.

Related publications: Pálfi et al., 2018.; Vasanits-Zsigrai et al., 2015.

1.3 GABA-A receptor blocking effect is significantly less in case of DNI-Glu•TFA compared to MNI-Glu. The caged compounds must be ineffective during experiments without any light irradiation, however caged compounds have an ion channel antagonist effect. MNI-Glu has a significant antagonist effect on endogenous GABAergic currents (~80% at 300 μM). I isolated the GABA current from other current components with pharmacology to quantify the GABA antagonist effect of DNI-Glu•TFA. I showed that there is no significant change (~5% at 350 μM) in inhibition current amplitude in the presence of DNI-Glu•TFA.

Related publication: Pálfi et al., 2018.

1.4 No significant effect on the amplitude of potassium currents in the presence of DNI-Glu•TFA. Potassium channels are responsible for maintaining the resting membrane potential of a neuron as well as its repolarization following an action potential. Therefore, in physiological experiment it is crucial caged material must not affect K^+ channels. I showed experimentally that the DNI-Glu•TFA that did not change the potassium currents during long time-scale measurements.

Related publications: Bywalez et al., 2015.; Pálfi et al., 2018.

DOI:10.15774/PPKE.ITK.2021.008

2.1 Localized physiological dendritic Ca^{2+} transients could be simulated only with DNI-Glu•TFA uncaging. In order to validate precise physiological dendritic activity patterns on PV INs, we had to introduce a more efficient caged compound. The commercially available MNI-Glu is not enough sensitive to induce well localized 'hot-spot' regions with the accompanying regenerative Ca transients. It is crucial for long timescale measurements to keep laser intensity on a moderate level during frequent glutamate uncaging. Tuft regions of the dendrites are very sensitive to phototoxicity, therefore the key step is to define the 2P efficacy dependent threshold of spike initiation. I showed that dendritic Ca^{2+} spikes could be simulated only with DNI-Glu•TFA uncaging.

Related publications: Chiovini et al. 2014., Pálfi et al., 2018.

2.2 DNI-Glu•TFA uncaging could be used for pharmacological experiments to quantify the ion channel contributions in the generation of dendritic Ca^{2+} transients. Ongoing network activities cause multiple and heterogeneous calcium patterns along the dendrites. On one hand, pharmacological experiments are a widely accepted method to validate the contributions of ion channels in dendritic calcium transients. On the other hand, dynamic of the network could be blocked after the application of different pharmacons and result a distorted input pattern. To avoid this issue, I had to use glutamate uncaging techniques to simulate physiological dendritic activities. To precisely quantify the distribution of ion channels along dendrites it is necessary to repeat the photoactivation in well-defined uncaging localizations. In physiological experiments DNI-Glu•TFA is capable of the generation and long-term repetition of this precise and stable dendritic pattern. The result of our biological experiment showed that the uncaging evoked Ca^{2+} spikes are mainly mediated by L-type voltage gated calcium channels on apical and basal dendritic parts.

Related publications: Pálfi et al., 2018.; Chiovini et al. 2014.

DOI:10.15774/PPKE.ITK.2021.008

RELATED PUBLICATIONS

High efficiency two-photon uncaging coupled by the correction of spontaneous hydrolysis.
Pálfi D, Chiovini B, Szalay G, Kaszás A, Turi GF, Katona G, Ábrányi-Balogh P, Szőri M, Potor A, Frigyesi O, Lukácsné Haveland C, Szadai Z, Madarász M, Vasanits-Zsigrai A, Molnár-Perl I, Viskolcz B, Csizmadia IG, Mucsi Z & Rózsa B.
Org Biomol Chem. 2018 Mar 2. doi: 10.1039/c8ob00025e.
Impact factor: *3.564*

Local postsynaptic voltage-gated sodium channel activation in dendritic spines of olfactory bulb granule cells.
Bywalez WG, Patirniche D, Rupprecht V, Stemmler M, Herz AV, **Pálfi D**, Rózsa B & Egger V.
Neuron. 2015 Feb 4;85(3):590-601. doi: 10.1016/j.neuron.2014.12.051. Epub 2015 Jan 22.
Impact Factor: *15.054*

Quantitation of various indolinyl caged glutamates as their o-phthalaldehyde derivatives by high performance liquid chromatography coupled with tandem spectroscopic detections: derivatization, stoichiometry and stability studies.
Vasanits-Zsigrai A, Majercsik O, Tóth G, Csámpai A, Haveland-Lukács C, **Pálfi D**, Szadai Z, Rózsa B & Molnár-Perl I.
J Chromatogr A. 2015 May 15;1394:81-8. doi: 10.1016/j.chroma.2015.03.039. Epub 2015 Mar 25.
Impact Factor: *4.169*

Dendritic spikes induce ripples in parvalbumin interneurons during hippocampal sharp waves.
Chiovini B, Turi GF, Katona G, Kaszás A, **Pálfi D**, Maák P, Szalay G, Szabó MF, Szabó G, Szadai Z, Káli S & Rózsa B.
Neuron. 2014 May 21;82(4):908-24. doi: 10.1016/j.neuron.2014.04.004.
Impact Factor: *15.054*

Other Publications

Fast three-dimensional two-photon scanning methods for studying neuronal physiology on cellular and network level
Szalay G, Judák L, Szadai Z, Chiovini B, Mezey D, **Pálfi D**, Madarász M, Ócsai K, Csikor F, Veress M, Maák P & Katona G.
Orv Hetil. 2015 Dec 27;156(52):2120-6. doi: 10.1556/650.2015.30329. Hungarian.

Combined two-photon imaging, electrophysiological, and anatomical investigation of the human neocortex in vitro
Kerekes RB, Tóth K, Kaszás A, Chiovini B, Szadai Z, Szalay G, **Pálfi D**, Bagó A, Spitzer K, Rózsa B, Ulbert I, & Wittner L
Neurophotonics 2014; 1(1):011013. doi: 10.1117/1.NPh.1.1.011013

Silicon carbide quantum dots for bioimaging
Beke D, Szekrenyes Z, **Pálfi D**, Rona G, Balogh I, Maak P, Katona G, Czigany Zs, Kamaras K, Rozsa B, Buday L, Vertessy B, & Gali A
Journal of Materials Research Vol. 28, Issue 02, 2012, pp 205-209

Cumulative impact factor: *39.779*

DOI:10.15774/PPKE.ITK.2021.008

CONFERENCE POSTERS AND ORAL PRESENTATIONS

Oral presentations

Pálfi D, Chiovini B, Szalay G, Katona G, Rózsa B
New caged compounds, KOKI Days 2013, Poroszló, Hungary

Pálfi D, Katona G., Szalay G., Maák P., Kaszás A., Veress M., Hillier D., Chiovini B., Vizi ES., Roska B., Rózsa B.
Three-dimensional two-photon functional imaging with millimeter z-scanning range and sub-millisecond temporal resolution *in vivo* and *in vitro*. MMT 2012, Siófok, Hungary

Pálfi D, Chiovini B, Turi GF, Katona G, Tamás G, Kaszás A, Szalay G, Rózsa B
Local calcium events investigating in hippocampal CA1 interneurons and pyramidal cells with real-time multi-photon scanning technique, MMT 2011, Siófok, Hungary

Poster presentations

***Dénes Pálfi**, Balázs Chiovini, Linda Judak, Gergely Szalay, Gábor Juhász, Gergely Katona, Balázs Rozsa*

Three-dimensional calcium imaging of mouse hippocampal neuronal ensembles during sharp wave-ripple complexes. SFN 2016, San Diego, USA

***Dénes Pálfi**, Gergely F. Turi, Balázs Chiovini, Attila Kaszás, Pál Maák, Gergely Katona, Gábor Szabó, Gergely Szalay, Zoltán Szadai, Miklós Madarász, Szabolcs Káli, Balázs Rózsa*

Dentritic integration in fast-spiking, parvalbumin-expressing interneurons during sharp wave-ripple activity. FENS 2014, Milano, Italy

***Dénes Pálfi**, Balázs Chiovini, Gergely Katona, Zoltán Szadai, Attila Kaszás, Gergely Turi, Balázs Rózsa*

Hippocampal sharp waves associated dendritic calcium transients revealed by three dimension acousto-optic imaging in parvalbumin positive interneurons. SFN 2013, San Diego, USA

***Dénes Pálfi**, Gergely Szalay, Klaudia Spitzer, Gergely Katona, Attila Kaszás, Balázs Chiovini, Miklós Madarász, Imre Csizmadia, Balázs Rózsa*

More effective caged compounds for two photon uncaging, MITT 2013, Budapest, Hungary

***Dénes Pálfi**, Gergely Katona, Balázs Chiovini, Gergely Szalay, Klaudia Spitzer, Attila Kaszás, Balázs Rózsa*

Roller Coaster Scanning Method for high-resolution 3D two photon laser scanning, FENS 2012, Barcelona, Spain

***Dénes Pálfi**, Balázs Chiovini, Klaudia Spitzer, Gergely Katona, Attila Kaszás, Gergely Szalay, Zoltán Szadai, Csilla Haveland Lukácsné, Orsolya Majercsik, Zoltán Mucsi, Imre Csizmadia, Balázs Rózsa*

Development of new GABA and more effective glutamate uncaging materials for two-photon microscopy. IBRO Workshop 2012, Szeged, Hungary.

DOI:10.15774/PPKE.ITK.2021.008

***Dénes Pálfi**, Balázs Chiovini, Klaudia Spitzer, Gergely Katona, Attila Kaszás, Gergely Szalay, Zoltán Szadai, Csilla Haveland Lukácsné, Orsolya Majercsik, Zoltán Mucsi, Imre Csizmadia, Balázs Rózsa*

Development of new GABA and more effective glutamate uncaging materials for two-photon microscopy. 3rd European Synapse Meeting, 13th – 15th October 2011, Balatonfüred, Hungary

Patent

I. G. Csizmadia, Z. Mucsi, G. Szalay, A. Kaszas, C. H. Lukacsne, O. Majercsik, A. Potor, G. Katona, B. J. Rozsa, D. Gundisch, Dorina; B. Chiovini, **D. Palfi**, Use of photocleavable compounds U.S. Pat. Appl. Publ. (2014), US 20140234883 A1 20140821.

DOI:10.15774/PPKE.ITK.2021.008

REFERENCES

[1] M. Göppert-Mayer, "Über Elementarakte mit zwei Quantensprüngen," *Annalen der Physik,* vol. 401, no. 3, pp. 273-294, 1931.

[2] H. W. Liu, Y. C. Liu, P. Wang, and X. B. Zhang, "Molecular engineering of two-photon fluorescent probes for bioimaging applications," (in English), *Methods and Applications in Fluorescence,* vol. 5, no. 1, Mar 2017.

[3] W. Denk, J. H. Strickler, and W. W. Webb, "Two-photon laser scanning fluorescence microscopy," *Science,* vol. 248, no. 4951, pp. 73-6, Apr 6 1990.

[4] W. R. Zipfel, R. M. Williams, and W. W. Webb, "Nonlinear magic: multiphoton microscopy in the biosciences," *Nat Biotechnol,* vol. 21, no. 11, pp. 1369-77, Nov 2003.

[5] C. H. Tischbirek, A. Birkner, and A. Konnerth, "In vivo deep two-photon imaging of neural circuits with the fluorescent Ca(2+) indicator Cal-590," *J Physiol,* vol. 595, no. 10, pp. 3097-3105, May 15 2017.

[6] J. N. Kerr and W. Denk, "Imaging in vivo: watching the brain in action," *Nat Rev Neurosci,* vol. 9, no. 3, pp. 195-205, Mar 2008.

[7] A. Heckel, M. C. Buff, M. S. Raddatz, J. Muller, B. Potzsch, and G. Mayer, "An anticoagulant with light-triggered antidote activity," *Angew Chem Int Ed Engl,* vol. 45, no. 40, pp. 6748-50, Oct 13 2006.

[8] G. C. Ellis-Davies, "Caged compounds: photorelease technology for control of cellular chemistry and physiology," *Nat Methods,* vol. 4, no. 8, pp. 619-28, Aug 2007.

[9] M. Eder, W. Zieglgansberger, and H. U. Dodt, "Neocortical long-term potentiation and long-term depression: site of expression investigated by infrared-guided laser stimulation," *J Neurosci,* vol. 22, no. 17, pp. 7558-68, Sep 1 2002.

[10] D. L. Pettit and G. J. Augustine, "Distribution of functional glutamate and GABA receptors on hippocampal pyramidal cells and interneurons," *J Neurophysiol,* vol. 84, no. 1, pp. 28-38, Jul 2000.

[11] M. Matsuzaki, G. C. Ellis-Davies, T. Nemoto, Y. Miyashita, M. Iino, and H. Kasai, "Dendritic spine geometry is critical for AMPA receptor expression in hippocampal CA1 pyramidal neurons," *Nat Neurosci,* vol. 4, no. 11, pp. 1086-92, Nov 2001.

[12] L. Ramakrishnan and G. P. Hess, "Picrotoxin inhibition mechanism of a gamma-aminobutyric acid A receptor investigated by a laser-pulse photolysis technique," *Biochemistry,* vol. 44, no. 23, pp. 8523-32, Jun 14 2005.

[13] C. Grewer, "Investigation of the alpha(1)-glycine receptor channel-opening kinetics in the submillisecond time domain," *Biophys J,* vol. 77, no. 2, pp. 727-38, Aug 1999.

[14] I. H. Brivanlou, J. L. Dantzker, C. F. Stevens, and E. M. Callaway, "Topographic specificity of functional connections from hippocampal CA3 to CA1," *Proc Natl Acad Sci U S A,* vol. 101, no. 8, pp. 2560-5, Feb 24 2004.

[15] H. U. Dodt, A. Schierloh, M. Eder, and W. Zieglgansberger, "Circuitry of rat barrel cortex investigated by infrared-guided laser stimulation," *Neuroreport,* vol. 14, no. 4, pp. 623-7, Mar 24 2003.

[16] A. Losonczy and J. C. Magee, "Integrative properties of radial oblique dendrites in hippocampal CA1 pyramidal neurons," *Neuron,* vol. 50, no. 2, pp. 291-307, Apr 20 2006.
[17] R. Araya, J. Jiang, K. B. Eisenthal, and R. Yuste, "The spine neck filters membrane potentials," *Proc Natl Acad Sci U S A,* vol. 103, no. 47, pp. 17961-6, Nov 21 2006.
[18] S. Passlick, P. F. Kramer, M. T. Richers, J. T. Williams, and G. C. R. Ellis-Davies, "Two-color, one-photon uncaging of glutamate and GABA," *PLoS One,* vol. 12, no. 11, p. e0187732, 2017.
[19] A. I. Ciuciu, K. A. Korzycka, W. J. Lewis, P. M. Bennett, H. L. Anderson, and L. Flamigni, "Model dyads for 2PA uncaging of a protecting group via photoinduced electron transfer," *Phys Chem Chem Phys,* vol. 17, no. 9, pp. 6554-64, Mar 7 2015.
[20] M. Zhao *et al.*, "Optical triggered seizures using a caged 4-Aminopyridine," *Front Neurosci,* vol. 9, p. 25, 2015.
[21] A. Losonczy, J. K. Makara, and J. C. Magee, "Compartmentalized dendritic plasticity and input feature storage in neurons," *Nature,* vol. 452, no. 7186, pp. 436-41, Mar 27 2008.
[22] G. Katona *et al.*, "Roller Coaster Scanning reveals spontaneous triggering of dendritic spikes in CA1 interneurons," (in eng), *Proc Natl Acad Sci U S A,* Research Support, N.I.H., Extramural

Research Support, Non-U.S. Gov't vol. 108, no. 5, pp. 2148-53, Feb 1 2011.
[23] A. J. Granger and R. A. Nicoll, "Expression mechanisms underlying long-term potentiation: a postsynaptic view, 10 years on," *Philos Trans R Soc Lond B Biol Sci,* vol. 369, no. 1633, p. 20130136, Jan 5 2014.
[24] R. Araya, "Input transformation by dendritic spines of pyramidal neurons," *Front Neuroanat,* vol. 8, p. 141, 2014.
[25] G. Papageorgiou and J. E. T. Corrie, "Synthesis of an anionically substituted nitroindoline-caged GABA reagent that has reduced affinity for GABA receptors," (in English), *Tetrahedron,* vol. 63, no. 39, pp. 9668-9676, Sep 24 2007.
[26] M. Canepari, L. Nelson, G. Papageorgiou, J. E. Corrie, and D. Ogden, "Photochemical and pharmacological evaluation of 7-nitroindolinyl-and 4-methoxy-7-nitroindolinyl-amino acids as novel, fast caged neurotransmitters," *J Neurosci Methods,* vol. 112, no. 1, pp. 29-42, Nov 15 2001.
[27] G. Papageorgiou, D. Ogden, G. Kelly, and J. E. Corrie, "Synthetic and photochemical studies of substituted 1-acyl-7-nitroindolines," *Photochem Photobiol Sci,* vol. 4, no. 11, pp. 887-96, Nov 2005.
[28] G. Papageorgiou, M. Beato, and D. Ogden, "Synthesis and photolytic evaluation of a nitroindoline-caged glycine with a side chain of high negative charge for use in neuroscience," (in English), *Tetrahedron,* vol. 67, no. 29, pp. 5228-5234, Jul 22 2011.
[29] D. Warther *et al.*, "Two-photon uncaging: New prospects in neuroscience and cellular biology," *Bioorg Med Chem,* vol. 18, no. 22, pp. 7753-8, Nov 15 2010.
[30] D. Schlingloff, S. Kali, T. F. Freund, N. Hajos, and A. I. Gulyas, "Mechanisms of sharp wave initiation and ripple generation," *J Neurosci,* vol. 34, no. 34, pp. 11385-98, Aug 20 2014.
[31] D. L. Pritchett, J. H. Siegle, C. A. Deister, and C. I. Moore, "For things needing your attention: the role of neocortical gamma in sensory perception," *Curr Opin Neurobiol,* vol. 31, pp. 254-63, Apr 2015.

[32] T. Fernandez-Alfonso *et al.*, "Monitoring synaptic and neuronal activity in 3D with synthetic and genetic indicators using a compact acousto-optic lens two-photon microscope," *J Neurosci Methods,* vol. 222, pp. 69-81, Jan 30 2014.
[33] S. Quirin, J. Jackson, D. S. Peterka, and R. Yuste, "Simultaneous imaging of neural activity in three dimensions," *Front Neural Circuits,* vol. 8, p. 29, 2014.
[34] R. J. Cotton, E. Froudarakis, P. Storer, P. Saggau, and A. S. Tolias, "Three-dimensional mapping of microcircuit correlation structure," *Front Neural Circuits,* vol. 7, p. 151, 2013.
[35] M. A. Go *et al.*, "Four-dimensional multi-site photolysis of caged neurotransmitters," *Front Cell Neurosci,* vol. 7, p. 231, 2013.
[36] D. L. Pettit, S. S. Wang, K. R. Gee, and G. J. Augustine, "Chemical two-photon uncaging: a novel approach to mapping glutamate receptors," *Neuron,* vol. 19, no. 3, pp. 465-71, Sep 1997.
[37] M. A. Herman and C. E. Jahr, "Extracellular glutamate concentration in hippocampal slice," *J Neurosci,* vol. 27, no. 36, pp. 9736-41, Sep 5 2007.
[38] K. Moussawi, A. Riegel, S. Nair, and P. W. Kalivas, "Extracellular glutamate: functional compartments operate in different concentration ranges," *Front Syst Neurosci,* vol. 5, p. 94, 2011.
[39] D. K. Patneau and M. L. Mayer, "Structure-activity relationships for amino acid transmitter candidates acting at N-methyl-D-aspartate and quisqualate receptors," *J Neurosci,* vol. 10, no. 7, pp. 2385-99, Jul 1990.
[40] L. O. Trussell and G. D. Fischbach, "Glutamate receptor desensitization and its role in synaptic transmission," *Neuron,* vol. 3, no. 2, pp. 209-18, Aug 1989.
[41] P. J. Conn and J. P. Pin, "Pharmacology and functions of metabotropic glutamate receptors," *Annu Rev Pharmacol Toxicol,* vol. 37, pp. 205-37, 1997.
[42] M. A. Priestman, L. Sun, and D. S. Lawrence, "Dual wavelength photoactivation of cAMP- and cGMP-dependent protein kinase signaling pathways," *ACS Chem Biol,* vol. 6, no. 4, pp. 377-84, Apr 15 2011.
[43] S. Kantevari, M. Matsuzaki, Y. Kanemoto, H. Kasai, and G. C. Ellis-Davies, "Two-color, two-photon uncaging of glutamate and GABA," *Nat Methods,* vol. 7, no. 2, pp. 123-5, Feb 2010.
[44] J. M. Amatrudo, J. P. Olson, H. K. Agarwal, and G. C. Ellis-Davies, "Caged compounds for multichromic optical interrogation of neural systems," *Eur J Neurosci,* vol. 41, no. 1, pp. 5-16, Jan 2015.
[45] C. J. Cramer, „Essential of Computational Chemistry", *Wiley*, Ch. 4., pp. 95–120, 2002.
[46] C. J. Cramer, „Essential of Computational Chemistry", *Wiley*, Ch. 8., pp. 275–316, 2002.
[47] W. Kohn, A. D. Becke, R. G. Parr, *J. Phys. Chem.*, 100, 12974, 1996.
[48] P. Hohenberg, W. Kohn, *Phys. Rev.*, 136, 864, 1964.
[49] C. J. Cramer, „Essential of Computational Chemistry", *Wiley*, Ch. 10., pp. 319–345, 2002.
[50] C. J. Cramer, „Essential of Computational Chemistry", *Wiley*, Ch. 11., pp. 347–378, 2002.
[51] M. Cossi, N. Rega, G. Scalmani, and V. Barone, *J. Comp. Chem.*, 24, 669, 2003.
[52] Gaussian 03, Revision C.02, M. J. Frisch, G. W. Trucks, H. B. Schlegel, G. E. Scuseria, M. A. Robb, J. RCheeseman, J. A. Montgomery, Jr., T. Vreven, K. N. Kudin, J. C. Burant, J. M. Millam, S. S. Iyengar, J. Tomasi, V. Barone, B. Mennucci, M. Cossi, G. Scalmani, N. Rega, G. A. Petersson, H. Nakatsuji, M.

Hada, M. Ehara, K. Toyota, R. Fukuda, J. Hasegawa, M. Ishida, T. Nakajima, Y. Honda, O. Kitao, H. Nakai, M. Klene, X. Li, J. E. Knox, H. P. Hratchian, J. B. Cross, C. Adamo, J. Jaramillo, R. Gomperts, R. E. Stratmann, O. Yazyev, A. J. Austin, R. Cammi, C. Pomelli, J. W. Ochterski, P. Y. Ayala, K. Morokuma, G. A. Voth, P. Salvador, J. J. Dannenberg, V. G. Zakrzewski, S. Dapprich, A. D. Daniels, M. C. Strain, O. Farkas, D. K. Malick, A. D. Rabuck, K. Raghavachari, J. B. Foresman, J. V. Ortiz, Q. Cui, A. G. Baboul, S. Clifford, J. Cioslowski, B. B. Stefanov, G. Liu, A. Liashenko, P. Piskorz, I. Komaromi, R. L. Martin, D. J. Fox, T. Keith, M. A. Al-Laham, C. Y. Peng, A. Nanayakkara, M. Challacombe, P. M. W. Gill, B. Johnson, W. Chen, M. W. Wong, C. Gonzalez, and J. A. Pople, Gaussian, Inc., Wallingford CT, 2004.

[53] Gaussian 09, Revision B.01, M. J. Frisch, G. W. Trucks, H. B. Schlegel, G. E. Scuseria, M. A. Robb, J. R. Cheeseman, G. Scalmani, V. Barone, B. Mennucci, G. A. Petersson, H. Nakatsuji, M. Caricato, X. Li, H. P. Hratchian, A. F. Izmaylov, J. Bloino, G. Zheng, J. L. Sonnenberg, M. Hada, M. Ehara, K. Toyota, R. Fukuda, J. Hasegawa, M. Ishida, T. Nakajima, Y. Honda, O. Kitao, H. Nakai, T. Vreven, J. A. Montgomery, Jr., J. E. Peralta, F. Ogliaro, M. Bearpark, J. J. Heyd, E. Brothers, K. N. Kudin, V. N. Staroverov, T. Keith, R. Kobayashi, J. Normand, K. Raghavachari, A. Rendell, J. C. Burant, S. S. Iyengar, J. Tomasi, M. Cossi, N. Rega, J. M. Millam, M. Klene, J. E. Knox, J. B. Cross, V. Bakken, C. Adamo, J. Jaramillo, R. Gomperts, R. E. Stratmann, O. Yazyev, A. J. Austin, R. Cammi, C. Pomelli, J. W. Ochterski, R. L. Martin, K. Morokuma, V. G. Zakrzewski, G. A. Voth, P. Salvador, J. J. Dannenberg, S. Dapprich, A. D. Daniels, O. Farkas, J. B. Foresman, J. V. Ortiz, J. Cioslowski, and D. J. Fox, Gaussian, Inc., Wallingford CT, 2010.

[54] G. W. T. M. J. Frisch, H. B. Schlegel, G. E. Scuseria, M. A. Robb, J. R. Cheeseman, G. Scalmani, V. Barone, B. Mennucci, G. A. Petersson, H. Nakatsuji, M. Caricato, X. Li, H. P. Hratchian, A. F. Izmaylov, J. Bloino, G. Zheng, J. L. Sonnenberg, M. Hada, M. Ehara, K. Toyota, R. Fukuda, J. Hasegawa, M. Ishida, T. Nakajima, Y. Honda, O. Kitao, H. Nakai, T. Vreven, J. A. Montgomery, Jr., J. E. Peralta, F. Ogliaro, M. Bearpark, J. J. Heyd, E. Brothers, K. N. Kudin, V. N. Staroverov, R. Kobayashi, J. Normand, K. Raghavachari, A. Rendell, J. C. Burant, S. S. Iyengar, J. Tomasi, M. Cossi, N. Rega, J. M. Millam, M. Klene, J. E. Knox, J. B. Cross, V. Bakken, C. Adamo, J. Jaramillo, R. Gomperts, R. E. Stratmann, O. Yazyev, A. J. Austin, R. Cammi, C. Pomelli, J. W. Ochterski, R. L. Martin, K. Morokuma, V. G. Zakrzewski, G. A. Voth, P. Salvador, J. J. Dannenberg, S. Dapprich, A. D. Daniels, O. Farkas, J. B. Foresman, J. V. Ortiz, J. Cioslowski, and D. J. Fox, "Gaussian, Inc., Wallingford CT, Gaussian 09, Revision A.1, ," ed, 2009.

[55] C. A. K. Aidas, K. L. Bak, V. Bakken, R. Bast, L. Boman, O. Christiansen, R. Cimiraglia, S. Coriani, P. Dahle, E. K. Dalskov, U. Ekström, T. Enevoldsen, J. J. Eriksen, P. Ettenhuber, B. Fernández, L. Ferrighi, H. Fliegl, L. Frediani, K. Hald, A. Halkier, C. Hättig, H. Heiberg, T. Helgaker, A. C. Hennum, H. Hettema, E. Hjertenæs, S. Høst, I.-M. Høyvik, M. F. Iozzi, B. Jansik, H. J. Aa. Jensen, D. Jonsson, P. Jørgensen, J. Kauczor, S. Kirpekar, T. Kjærgaard, W. Klopper, S. Knecht, R. Kobayashi, H. Koch, J. Kongsted, A. Krapp, K. Kristensen, A. Ligabue, O. B. Lutnæs, J. I. Melo, K. V. Mikkelsen, R. H. Myhre, C. Neiss, C. B. Nielsen, P. Norman, J. Olsen, J. M. H. Olsen, A. Osted, M. J. Packer, F. Pawlowski, T. B. Pedersen, P. F. Provasi, S. Reine, Z. Rinkevicius, T.

A. Ruden, K. Ruud, V. Rybkin, P. Salek, C. C. M. Samson, A. Sánchez de Merás, T. Saue, S. P. A. Sauer, B. Schimmelpfennig, K. Sneskov, A. H. Steindal, K. O. Sylvester-Hvid, P. R. Taylor, A. M. Teale, E. I. Tellgren, D. P. Tew, A. J. Thorvaldsen, L. Thøgersen, O. Vahtras, M. A. Watson, D. J. D. Wilson, M. Ziolkowski, and H. Ågren, "The Dalton quantum chemistry program system," *WIREs Comput. Mol. Sci. ,* vol. 4, pp. 269–284., 2014.

[56] W.M. McClain, *The Journal of Chemical Physics,* no. 55, pp. 2789-2796., 1971.

[57] Z. Mucsi, A. Tsai, M. Szori, G. A. Chass, B. Viskolcz, and I. G. Csizmadia, "A quantitative scale for the extent of conjugation of the amide bond. Amidity percentage as a chemical driving force," (in English), *Journal of Physical Chemistry A,* vol. 111, no. 50, pp. 13245-13254, Dec 20 2007.

[58] M. K. Zs. Huszti, *Glia 2nd ed.* Akadémia Kiadó Zrt, 2008.

[59] C. Frieden, "Glutamic dehydrogenase. III. The order of substrate addition in the enzymatic reaction," *J Biol Chem,* vol. 234, pp. 2891-6, Nov 1959.

[60] J. A. Dzubay and C. E. Jahr, "The concentration of synaptically released glutamate outside of the climbing fiber-Purkinje cell synaptic cleft," *J Neurosci,* vol. 19, no. 13, pp. 5265-74, Jul 1 1999.

[61] A. Vasanits and I. Molnar-Perl, "Temperature, eluent flow-rate and column effects on the retention and quantitation properties of phenylthiocarbamyl derivatives of amino acids in reversed-phase high-performance liquid chromatography," *J Chromatogr A,* vol. 832, no. 1-2, pp. 109-22, Feb 5 1999.

[62] P. Sah, S. Hestrin, and R. A. Nicoll, "Tonic activation of NMDA receptors by ambient glutamate enhances excitability of neurons," *Science,* vol. 246, no. 4931, pp. 815-8, Nov 10 1989.

[63] O. D. Fedoryak, J. Y. Sul, P. G. Haydon, and G. C. Ellis-Davies, "Synthesis of a caged glutamate for efficient one- and two-photon photorelease on living cells," *Chem Commun (Camb),* no. 29, pp. 3664-6, Aug 7 2005.

[64] E. Fino, R. Araya, D. S. Peterka, M. Salierno, R. Etchenique, and R. Yuste, "RuBi-Glutamate: Two-Photon and Visible-Light Photoactivation of Neurons and Dendritic spines," *Front Neural Circuits,* vol. 3, p. 2, 2009.

[65] P. Molnar and J. V. Nadler, "gamma-Aminobutyrate, alpha-carboxy-2-nitrobenzyl ester selectively blocks inhibitory synaptic transmission in rat dentate gyrus," *Eur J Pharmacol,* vol. 391, no. 3, pp. 255-62, Mar 17 2000.

[66] B. Rozsa, T. Zelles, E. S. Vizi, and B. Lendvai, "Distance-dependent scaling of calcium transients evoked by backpropagating spikes and synaptic activity in dendrites of hippocampal interneurons," *J Neurosci,* vol. 24, no. 3, pp. 661-70, Jan 21 2004.

[67] J. Mitterdorfer and B. P. Bean, "Potassium currents during the action potential of hippocampal CA3 neurons," *J Neurosci,* vol. 22, no. 23, pp. 10106-15, Dec 1 2002.

[68] M. Matsuzaki, N. Honkura, G. C. Ellis-Davies, and H. Kasai, "Structural basis of long-term potentiation in single dendritic spines," *Nature,* vol. 429, no. 6993, pp. 761-6, Jun 17 2004.

[69] T. Nevian, M. E. Larkum, A. Polsky, and J. Schiller, "Properties of basal dendrites of layer 5 pyramidal neurons: a direct patch-clamp recording study," *Nat Neurosci,* vol. 10, no. 2, pp. 206-14, Feb 2007.

[70] N. Akaike, N. Murakami, S. Katsurabayashi, Y. H. Jin, and T. Imazawa, "Focal stimulation of single GABAergic presynaptic boutons on the rat hippocampal neuron," *Neurosci Res,* vol. 42, no. 3, pp. 187-95, Mar 2002.

[71] A. Doi, H. Ishibashi, S. Jinno, T. Kosaka, and N. Akaike, "Presynaptic inhibition of GABAergic miniature currents by metabotropic glutamate receptor in the rat CNS," *Neuroscience,* vol. 109, no. 2, pp. 299-311, 2002.
[72] G. Bort, T. Gallavardin, D. Ogden, and P. I. Dalko, "From one-photon to two-photon probes: "caged" compounds, actuators, and photoswitches," *Angew Chem Int Ed Engl,* vol. 52, no. 17, pp. 4526-37, Apr 22 2013.
[73] Y. Yang *et al.*, "In vitro and in vivo uncaging and bioluminescence imaging by using photocaged upconversion nanoparticles," *Angew Chem Int Ed Engl,* vol. 51, no. 13, pp. 3125-9, Mar 26 2012.
[74] F. Pouille and M. Scanziani, "Enforcement of temporal fidelity in pyramidal cells by somatic feed-forward inhibition," *Science,* vol. 293, no. 5532, pp. 1159-63, Aug 10 2001.
[75] T. F. Freund and I. Katona, "Perisomatic inhibition," *Neuron,* vol. 56, no. 1, pp. 33-42, Oct 4 2007.
[76] J. H. Goldberg and R. Yuste, "Space matters: local and global dendritic Ca2+ compartmentalization in cortical interneurons," *Trends Neurosci,* vol. 28, no. 3, pp. 158-67, Mar 2005.
[77] T. Klausberger *et al.*, "Brain-state- and cell-type-specific firing of hippocampal interneurons in vivo," *Nature,* vol. 421, no. 6925, pp. 844-8, Feb 20 2003.
[78] G. Buzsaki and F. L. Silva, "High frequency oscillations in the intact brain," *Prog Neurobiol,* vol. 98, no. 3, pp. 241-9, Sep 2012.
[79] G. Buzsaki, C. A. Anastassiou, and C. Koch, "The origin of extracellular fields and currents--EEG, ECoG, LFP and spikes," *Nat Rev Neurosci,* vol. 13, no. 6, pp. 407-20, May 18 2012.
[80] D. J. Lodge, M. M. Behrens, and A. A. Grace, "A loss of parvalbumin-containing interneurons is associated with diminished oscillatory activity in an animal model of schizophrenia," *J Neurosci,* vol. 29, no. 8, pp. 2344-54, Feb 25 2009.
[81] V. Volman, M. M. Behrens, and T. J. Sejnowski, "Downregulation of parvalbumin at cortical GABA synapses reduces network gamma oscillatory activity," *J Neurosci,* vol. 31, no. 49, pp. 18137-48, Dec 7 2011.
[82] H. Hu, M. Martina, and P. Jonas, "Dendritic mechanisms underlying rapid synaptic activation of fast-spiking hippocampal interneurons," *Science,* vol. 327, no. 5961, pp. 52-8, Jan 1 2010.
[83] E. H. Buhl, T. Szilagyi, K. Halasy, and P. Somogyi, "Physiological properties of anatomically identified basket and bistratified cells in the CA1 area of the rat hippocampus in vitro," *Hippocampus,* vol. 6, no. 3, pp. 294-305, 1996.
[84] F. Pouille and M. Scanziani, "Routing of spike series by dynamic circuits in the hippocampus," *Nature,* vol. 429, no. 6993, pp. 717-23, Jun 17 2004.
[85] J. H. Goldberg, R. Yuste, and G. Tamas, "Ca2+ imaging of mouse neocortical interneurone dendrites: contribution of Ca2+-permeable AMPA and NMDA receptors to subthreshold Ca2+dynamics," *J Physiol,* vol. 551, no. Pt 1, pp. 67-78, Aug 15 2003.
[86] J. H. Goldberg, G. Tamas, and R. Yuste, "Ca2+ imaging of mouse neocortical interneurone dendrites: Ia-type K+ channels control action potential backpropagation," *J Physiol,* vol. 551, no. Pt 1, pp. 49-65, Aug 15 2003.
[87] J. H. Goldberg, G. Tamas, D. Aronov, and R. Yuste, "Calcium microdomains in aspiny dendrites," *Neuron,* vol. 40, no. 4, pp. 807-21, Nov 13 2003.
[88] W. Nissen, A. Szabo, J. Somogyi, P. Somogyi, and K. P. Lamsa, "Cell type-specific long-term plasticity at glutamatergic synapses onto hippocampal

interneurons expressing either parvalbumin or CB1 cannabinoid receptor," *J Neurosci,* vol. 30, no. 4, pp. 1337-47, Jan 27 2010.
[89] L. Topolnik, "Dendritic calcium mechanisms and long-term potentiation in cortical inhibitory interneurons," *Eur J Neurosci,* vol. 35, no. 4, pp. 496-506, Feb 2012.
[90] D. Fricker and R. Miles, "EPSP amplification and the precision of spike timing in hippocampal neurons," *Neuron,* vol. 28, no. 2, pp. 559-69, Nov 2000.
[91] N. Takahashi *et al.*, "Locally synchronized synaptic inputs," *Science,* vol. 335, no. 6066, pp. 353-6, Jan 20 2012.
[92] B. Chiovini *et al.*, "Enhanced dendritic action potential backpropagation in parvalbumin-positive basket cells during sharp wave activity," *Neurochem Res,* vol. 35, no. 12, pp. 2086-95, Dec 2010.
[93] F. Bahner *et al.*, "Cellular correlate of assembly formation in oscillating hippocampal networks in vitro," *Proc Natl Acad Sci U S A,* vol. 108, no. 35, pp. E607-16, Aug 30 2011.
[94] N. Maier *et al.*, "Coherent phasic excitation during hippocampal ripples," *Neuron,* vol. 72, no. 1, pp. 137-52, Oct 6 2011.
[95] N. Hajos *et al.*, "Maintaining network activity in submerged hippocampal slices: importance of oxygen supply," *Eur J Neurosci,* vol. 29, no. 2, pp. 319-27, Jan 2009.
[96] G. Katona *et al.*, "Fast two-photon in vivo imaging with three-dimensional random-access scanning in large tissue volumes," *Nat Methods,* vol. 9, no. 2, pp. 201-8, Jan 8 2012.
[97] N. Matsumoto, K. Okamoto, Y. Takagi, and Y. Ikegaya, "3-Hz subthreshold oscillations of CA2 neurons In vivo," (in English), *Hippocampus,* vol. 26, no. 12, pp. 1570-1578, Dec 2016.
[98] A. H. Meyer, I. Katona, M. Blatow, A. Rozov, and H. Monyer, "In vivo labeling of parvalbumin-positive interneurons and analysis of electrical coupling in identified neurons," *J Neurosci,* vol. 22, no. 16, pp. 7055-64, Aug 15 2002.
[99] G. Buzsaki, "Hippocampal sharp waves: their origin and significance," *Brain Res,* vol. 398, no. 2, pp. 242-52, Nov 29 1986.
[100] K. P. Lamsa, J. H. Heeroma, P. Somogyi, D. A. Rusakov, and D. M. Kullmann, "Anti-Hebbian long-term potentiation in the hippocampal feedback inhibitory circuit," *Science,* vol. 315, no. 5816, pp. 1262-6, Mar 2 2007.
[101] M. Avermann, C. Tomm, C. Mateo, W. Gerstner, and C. C. Petersen, "Microcircuits of excitatory and inhibitory neurons in layer 2/3 of mouse barrel cortex," *J Neurophysiol,* vol. 107, no. 11, pp. 3116-34, Jun 2012.
[102] A. Norenberg, H. Hu, I. Vida, M. Bartos, and P. Jonas, "Distinct nonuniform cable properties optimize rapid and efficient activation of fast-spiking GABAergic interneurons," *Proc Natl Acad Sci U S A,* vol. 107, no. 2, pp. 894-9, Jan 12 2010.
[103] F. Helmchen, G. S. Stuart, N; Hausser, M, Ed. *Dendrites: Biochemical compartmentalization in dendries*, second edition ed. Oxford University Press, 1999.
[104] T. Gloveli *et al.*, "Differential involvement of oriens/pyramidale interneurones in hippocampal network oscillations in vitro," *J Physiol,* vol. 562, no. Pt 1, pp. 131-47, Jan 1 2005.
[105] A. I. Gulyas, M. Megias, Z. Emri, and T. F. Freund, "Total number and ratio of excitatory and inhibitory synapses converging onto single interneurons of

different types in the CA1 area of the rat hippocampus," *J Neurosci,* vol. 19, no. 22, pp. 10082-97, Nov 15 1999.
[106] A. B. Ali, J. Deuchars, H. Pawelzik, and A. M. Thomson, "CA1 pyramidal to basket and bistratified cell EPSPs: dual intracellular recordings in rat hippocampal slices," *J Physiol,* vol. 507 (Pt 1), pp. 201-17, Feb 15 1998.
[107] K. Vervaeke, A. Lorincz, Z. Nusser, and R. A. Silver, "Gap junctions compensate for sublinear dendritic integration in an inhibitory network," *Science,* vol. 335, no. 6076, pp. 1624-8, Mar 30 2012.
[108] T. Abrahamsson, L. Cathala, K. Matsui, R. Shigemoto, and D. A. Digregorio, "Thin dendrites of cerebellar interneurons confer sublinear synaptic integration and a gradient of short-term plasticity," *Neuron,* vol. 73, no. 6, pp. 1159-72, Mar 22 2012.
[109] J. Vinet and A. Sik, "Expression pattern of voltage-dependent calcium channel subunits in hippocampal inhibitory neurons in mice," *Neuroscience,* vol. 143, no. 1, pp. 189-212, Nov 17 2006.
[110] J. Schiller, Y. Schiller, G. Stuart, and B. Sakmann, "Calcium action potentials restricted to distal apical dendrites of rat neocortical pyramidal neurons," *J Physiol,* vol. 505 (Pt 3), pp. 605-16, Dec 15 1997.
[111] M. E. Larkum, K. M. Kaiser, and B. Sakmann, "Calcium electrogenesis in distal apical dendrites of layer 5 pyramidal cells at a critical frequency of back-propagating action potentials," *Proc Natl Acad Sci U S A,* vol. 96, no. 25, pp. 14600-4, Dec 7 1999.
[112] P. Poirazi, T. Brannon, and B. W. Mel, "Pyramidal neuron as two-layer neural network," *Neuron,* vol. 37, no. 6, pp. 989-99, Mar 27 2003.
[113] N. Brunel and X. J. Wang, "What determines the frequency of fast network oscillations with irregular neural discharges? I. Synaptic dynamics and excitation-inhibition balance," *J Neurophysiol,* vol. 90, no. 1, pp. 415-30, Jul 2003.
[114] N. Maier, V. Nimmrich, and A. Draguhn, "Cellular and network mechanisms underlying spontaneous sharp wave-ripple complexes in mouse hippocampal slices," *J Physiol,* vol. 550, no. Pt 3, pp. 873-87, Aug 1 2003.
[115] R. D. Traub and A. Bibbig, "A model of high-frequency ripples in the hippocampus based on synaptic coupling plus axon-axon gap junctions between pyramidal neurons," *J Neurosci,* vol. 20, no. 6, pp. 2086-93, Mar 15 2000.
[116] A. Ylinen *et al.*, "Sharp wave-associated high-frequency oscillation (200 Hz) in the intact hippocampus: network and intracellular mechanisms," *J Neurosci,* vol. 15, no. 1 Pt 1, pp. 30-46, Jan 1995.
[117] J. Taxidis, S. Coombes, R. Mason, and M. R. Owen, "Modeling sharp wave-ripple complexes through a CA3-CA1 network model with chemical synapses," *Hippocampus,* vol. 22, no. 5, pp. 995-1017, May 2012.
[118] T. J. Ellender, W. Nissen, L. L. Colgin, E. O. Mann, and O. Paulsen, "Priming of hippocampal population bursts by individual perisomatic-targeting interneurons," *J Neurosci,* vol. 30, no. 17, pp. 5979-91, Apr 28 2010.
[119] V. Nimmrich, N. Maier, D. Schmitz, and A. Draguhn, "Induced sharp wave-ripple complexes in the absence of synaptic inhibition in mouse hippocampal slices," *J Physiol,* vol. 563, no. Pt 3, pp. 663-70, Mar 15 2005.
[120] Márton Bojtár, Krisztina Németh, Farkas Domahidy, Gergely Knorr, András Verkman, Mihály Kállay, and Péter Kele "Conditionally Activatable Visible-Light Photocages" *Journal of the American Chemical Society* X 142 (35), 15164-15171, 2020.

DOI:10.15774/PPKE.ITK.2021.008

[121] Geiller T, Vancura B, Terada S, Troullinou E, Chavlis S, Tsagkatakis G, Tsakalides P, Ócsai K, Poirazi P, Rózsa BJ, Losonczy A. "Large-Scale 3D Two-Photon Imaging of Molecularly Identified CA1 Interneuron Dynamics in Behaving Mice. " *Neuron*. 2020 Sep 25:S0896-6273(20)30713-3.